Scaling of Multiphase Flow, Droplet Trajectories, and Ice Accretion on a Rotating Wind Turbine Blade

by

© Galal Mohamed Galal Ibrahim

A Dissertation Submitted to the School of Graduate Studies

In Partial Fulfilment of the Requirements for the Degree Of

Doctor of Philosophy

Faculty of Engineering and Applied Science

Memorial University of Newfoundland

St. John's, NL, Canada

March 2023

Abstract

This thesis presents an extended formulation of non-dimensionalized governing equations for scaling of the flow field, droplet trajectories, and ice accretion on a rotating wind turbine blade. The analytical formulation leads to similitude relationships for ice accretion to evaluate new scaling parameters corresponding to the rotation of the blade. The scaling methodology can be used to determine alternative test conditions and predict icing conditions on a full-scale wind turbine blade. The main objective of the research is to develop and apply scaling methods and similitude analyses for ice accretion prediction on a rotating turbine blade. The investigation reviews the derivation of the similitude relationships for ice accretion scaling to evaluate their importance and develops new scaling parameters corresponding to the rotation of the turbine blade.

Numerical CFD icing simulations are also performed using ANSYS FENSAP ICE software to test the proposed scaling methods and verify the results. A turbine blade model is developed using blade element momentum theory (BEM). Turbine blade models are scaled up in geometry, and each case is tested at specific flow conditions as calculated using the scaling equations. Scaled conditions for velocity (streamwise and rotational), droplet size, and icing time are examined. CFD solutions for the flow field (air and droplet) are obtained in terms of velocity, droplet trajectories, pressure coefficient distributions, ice thickness, and ice shapes by quantifying the significant parameters involved in the icing process. Recommendations for parameters to be used for glaze and rime ice scaling on a rotating blade are presented and new numerical predictions are provided to support those recommendations. Numerical results and test conditions are obtained at sea level in wind tunnel facilities for experimental investigation. The research results provide valuable insight to predict ice accretion on large wind turbine blades in the field, based on smaller scaled blade models tested in a laboratory setting.

Acknowledgements

This thesis is submitted in partial fulfilment of the requirements for the degree of Doctor of Philosphy (Ph.D.) at Memorial University of Newfoundland. The research work is a result of my doctoral studies under the supervision of Prof. Kevin Pope and Prof. Greg F. Naterer. During my Ph.D. program, I received professional and personal support from my supervision team, family members, and colleagues. I would like to take this opportunity to thank all of them; without them, I could never reach my goal of completing this Ph.D. program with such fruitful outcomes.

First and foremost, I would like to praise "Allah'' the almighty, the most gracious, and the most merciful for his blessing given to me during my study and in completing this thesis. I would like to express my special appreciation and sincere thanks to my supervisors, Prof. Kevin Pope and Prof. Greg F. Naterer, for their outstanding supervision on both academic and professional levels and financial support throughout this Ph.D. program. I am also very grateful to them for their continuous encouragement and prompt guidance. I greatly appreciate their time in contributing to these research outcomes and enhancing my professional development skills.

Last but not least, endless thanks are reserved to all my dear family members, who gave me their strong spiritual support throughout my life. I do not say it enough, but I am so thankful to have you all in my life. Without your unconditional love, encouragement, support and guidance, I would not have been who I am today.

Co-Authorship Statements

I, Galal Ibrahim, hold a principal author status for all of this dissertation's manuscript chapters (Chapters 2-5). However, each manuscript is co-authored by my co-supervisors, whose contributions have facilitated the development of this work, as described below.

- Paper 1 in Chapter 2: Ibrahim, G., Naterer, G., & Pope, K. (2021). Scaling effects on flow field and ice accretion for a rotating wind turbine blade. Progress in Canadian Mechanical Engineering. Volume 4. https://doi.org/10.32393/csme.2021.198

  I was the primary author, with authors 2 and 3 contributing to this work's conceptualization, methodology, formulation, development and refinement of the presentation.

- Paper 2 in Chapter 3: Ibrahim, G. M., Naterer, G. F., & Pope, K. (2022). Ice accretion on a rotating horizontal axis wind turbine blade. Progress in Canadian Mechanical Engineering. Volume 5. https://doi.org/10.7939/r3-rk5b-w453

  I was the primary author, with authors 2 and 3 contributing to this work's conceptualization, methodology, formulation, development and refinement of the presentation.

- Paper 3 in Chapter 4: Ibrahim, G. M., Pope, K., & Naterer, G. F. (2023). Scaling formulation of multiphase flow and droplet trajectories with rime ice accretion on a rotating wind turbine blade. Journal of Wind Engineering and Industrial Aerodynamics, 232, 105247. https://doi.org/10.1016/j.jweia.2022.105247

  I was the primary author, with authors 2 and 3 contributing to this work's conceptualization, methodology, formulation, development and refinement of the presentation.

- Paper 4 in Chapter 5: Ibrahim, G. M., Pope, K., & Naterer, G. F. (2023). Extended scaling approach for droplet flow and glaze ice accretion on a rotating wind turbine blade. Journal of Wind Engineering and Industrial Aerodynamics, 233, 105296. https://doi.org/10.1016/j.jweia.2022.105296

  I was the primary author, with authors 2 and 3 contributing to this work's conceptualization, methodology, formulation, development and refinement of the presentation.

---------- ----------

Galal Ibrahim Date

Table of Contents

List of Figures

List of Tables

Chapter 1

1. Introduction

1.1. Background

Wind energy in cold climate regions has gained greater attention from the scientific and financial community lately in efforts to achieve more ambitious targets for renewable energy. Good wind resources combined with typically low population density make it an attractive destination for the future development of the wind power market. However, the icing of wind turbines has been identified as a barrier, limiting the performance of wind turbines and energy production at elevated cold climate sites. In some cases this has led to a decrease in annual energy production of up to 17% and a reduction in the aerodynamic performance of wind turbines by up to 50% [1].

Atmospheric ice accumulation and low ambient temperatures pose particular challenges for the wind energy industry, such as reduced energy production, reduced mechanical lifespan of wind turbines, increased overall costs, and increased safety risks due to the potential for ice fall [2]. Several problems have been reported due to ice, including loss of power generation, disruption of blade aerodynamics, overloading due to delayed stall, increased fatigue of components due to an imbalance in the ice load, and damage caused by the melting of ice chunks. One of the major risks to wind turbine design and safety is atmospheric ice accumulation. To improve safety and reduce the capital cost and operational expenditure related to the operation of wind turbines in ice-prone areas, past studies have addressed the need to better understand the ice accretion process on wind turbine blades [3].

Atmospheric ice is mainly formed on the leading edge of a wind turbine blade due to an interaction with supercooled water droplets, which can freeze directly on its surface or immediately

after being momentarily delayed [3, 4]. By reducing the lift and increasing the drag force, accumulated ice changes blade shape in a way that increases its surface roughness which reduces aerodynamic performance. Three categories of parameters that cause adverse effects on wind aerodynamics include microscale surface roughness, large-scale surface roughness and ice geometry [5].

Atmospheric ice on wind turbines is commonly classified as rime and glaze ice. In comparison with rime ice, glaze ice has a more significant impact on aerodynamic performance, resulting in a higher loss of power generation. The rime ice is softer and less dense and occurs at lower temperatures when 100% of the impinging droplets freeze, whereas the glaze ice is harder and denser. If the freezing fraction of the impinging droplet is less than 100%, and some droplets are running along the blade surface as a very thin water film, glaze icing occurs close to the freezing temperature. Accreted ice, depending on the operational conditions, has a variety of possible shapes which lead to different aerodynamic performance losses. The shape of the accreted ice on the leading edge of the wind turbines is also determined by the geometry of the blade and operating conditions, which are mainly influenced by their respective wind velocity, air temperature, droplet size, distribution spectrum and liquid water content [3, 6].

Prediction of icing on wind turbine blades is a research field that aims to better understand the atmospheric ice accretion process, thereby minimizing the effects of atmospheric ice accretion on wind turbine performance and overall energy harvesting. The operation of wind farms is affected by a wide range of ice accumulation scales. In particular, three area of research are focused on this topic: field measurements, laboratory experiments and computer simulations.

Scaling methods using wind tunnel tests and numerical computational tools are useful approaches for assessing wind turbine performance during icing conditions. In a controlled environment, the effects of different operating and geometrical parameters on ice accretion physics

may be examined. An icing wind tunnel is an appropriate laboratory approach to study icing on wind turbine blades. However, some components may not be tested fully in an icing wind tunnel due to their size limitations since every wind tunnel has certain limits on the range of test conditions available for testing. Therefore, it is necessary to develop reliable methods of scaling both model size and test conditions. For the simulation and determination of wind turbine airfoil performance under different scaled icing conditions, advanced multiphase computational fluid dynamic models have become useful tools. This research primarily uses four modules to predict atmospheric ice accretion and test new flow scaling methods over a rotating blade: grid generation, airflow behaviour simulations, water droplet trajectory calculation, and surface thermodynamics analysis. This research focuses on developing new scaling parameters that can be used to scale ice accretions on a rotating blade. The proposed research conducts a detailed review of the currently available scaling methods for aircraft icing over the past 40 years and the development of new scaling parameters related to a turbine blade's rotation.

1.2. Research Motivation and Objectives

The motivation of this Ph.D. program is to investigate and analyze ice accretion on rotating wind turbine blade profiles and formulate new key parameters to scale icing conditions and ice accretions on larger turbine blade geometries. The scope of the investigation includes an evaluation of the icing scaling requirements. This research aims to non-dimensionalize the equations governing the icing process to identify scaling parameters, predict similar ice accretions on a wind turbine blade and to develop new correlations. The research identifies new scaling methods that can produce scaled ice accretions over various operating conditions that can be applied to predict wind turbine icing conditions.

The main research objectives of scaling methods are usually to ensure that the flow field, droplet field, and amount of accumulated ice are equivalent to the blade model size. Additionally, the predicted ice characteristics include the type, shape, and distributed thickness. The aerodynamic processes due to the icing are the same as that which would have occurred for the desired test conditions or reference blade model size. Thus, geometry, flow field, droplet trajectory and impingement / collection, and heat transfer rates, must be identical for accurate scaling predictions. Four areas of investigation should be considered for an ice scaling problem: flow field about the body, droplet trajectory and impingement characteristics, surface mass collection, and surface thermodynamics. Defining a specific set of scaling parameters is the key element and keeping them constant between different test conditions ensures the similarity of the icing conditions.

1.3. Thesis Contribution

The main contributions of this thesis are the extended analytical formulation of multiphase flow during glaze and rime icing effects over a rotating wind turbine blade and using numerical modelling, particularly computational fluid dynamics CFD multiphase analyses for ice accretion predictions on wind turbine blade profiles at various operating and geometric conditions. While a considerable amount of research exists on ice scaling over aircraft (i.e. stationary wing) using past scaling parameters, this thesis develops novel scaling methods using newly developed scaling parameters for predicting scaled icing conditions on a full-scale wind blade (i.e. rotating blade). The thesis results contribute to fluid mechanics with applications to wind turbine aerodynamics and icing. It allows a better knowledge of multiphase flow scaling on turbomachinery and rotating equipment. Additionally, it provides the wind power sector with engineering tools that can assist in predicting icing conditions during wind turbine operation in cold climate regions. One further

contribution of the thesis includes a design of an experimental setup to test scaled wind turbine prototype models available for future icing tests at Memorial University of Newfoundland.

1.4. Thesis Outline

This section outlines the organization of this thesis and gives a brief overview of each chapter.

- Chapter 1 presents an overview of the research aspects of this Ph.D. dissertation.
- Chapter 2 presents a numerical study to investigate ice accretion scaling on wind turbine blade sections with a scaling analysis under icing/operating conditions. The chapter analyzes the scaling effects in the flow field, droplet impingement and ice accretion process.
- Chapter 3 presents an additional numerical study investigating ice accumulation on a rotating horizontal axis wind turbine blade model. The chapter analyzes ice characteristics with a focus on spanwise variability along a rotating blade.
- Chapter 4 presents multiphase flow scaling and similitude analysis for ice accretion on a rotating wind turbine blade. The chapter presents the formulation of non-dimensionalized governing equations for scaling the flow field, droplet trajectories, and rime ice accretion on a rotating blade model. The chapter presents the scaling methodology for determining alternative test conditions to predict rime ice conditions on a rotating blade.
- Chapter 5 presents an extended approach for glaze ice accretion scaling on a rotating wind turbine blade. The chapter presents the multiphase flow formulation that leads to similitude relationships for glaze ice accretion to evaluate new scaling parameters corresponding to the rotation of the blade. The chapter presents and analyzes a non-

dimensional model of the flow field and droplet trajectories with glaze ice accretion on a rotating blade.

- Finally, Chapter 6 summarizes the contributions of this dissertation, discusses several potential extensions to research work, and provides suggestions for future research work.

References

[1] Yirtici, O., Tuncer, I. H., & Ozgen, S. (2016). Ice accretion prediction on wind turbines and consequent power losses. Journal of Physics, 753, https://doi.org/10.1088/1742-6596/753/2/022022

[2] Virk, M. S. (2011). Atmospheric ice accretion on non-rotating circular cylinder. The Journal of Computational Multiphase Flows, 3(4), 197–205. https://doi.org/10.1260/1757-482x.3.4.197

[3] Battisti, L. (2015). Effects of cold climates on wind turbine design and Operation. Wind Turbines in Cold Climates, 1–42. https://doi.org/10.1007/978-3-319-05191-8_1

[4] Pouryoussefi, S. G., Mirzaei, M., Nazemi, M.-M., Fouladi, M., & Doostmahmoudi, A. (2016). Experimental study of ice accretion effects on aerodynamic performance of an NACA 23012 airfoil. Chinese Journal of Aeronautics, 29(3), 585–595. https://doi.org/10.1016/j.cja.2016.03.002

[5] Lamraoui, F., Fortin, G., Perron, J., & Benoit, R. (2015). Canadian icing envelopes near the surface and its impact on Wind Energy Assessment. Cold Regions Science and Technology, 120, 76–88. https://doi.org/10.1016/j.coldregions.2015.09.007

[6] Ibrahim, G. M., Pope, K., & Muzychka, Y. S. (2018). Transient atmospheric ice accretion on wind turbine blades. Wind Engineering, 42(6), https://doi.org/10.1177/0309524x18780380

Chapter 2

2. Scaling Effects on Flow Field and Ice Accretion for a Rotating Wind Turbine Blade

In this chapter, a numerical study is presented to investigate blade sections (NACA 4415) with a scaling analysis. For variable rotational speeds (up to 60 RPMs) and operating/icing conditions for both similar models, the effects on the flow field, droplet impingement and ice accretion process are obtained. The numerical simulations are conducted using ANSYS FENSAP ICE software. Effects of the relative flow Reynolds number and speed ratio over two similar blade sections are investigated. Flow velocity contours, pressure distributions, droplet impingement/collection efficiencies and ice shapes/quantities are presented. The results of this study provide useful insight to predict icing on wind turbine blades including scaling effects among different blade configurations.

Nomenclature

A	Area (m^2)	H	Total enthalpy (kJ)
ρ	Density (kg/m^3)	μ	Dynamic viscosity (Pa·s)
d	Diameter (m)	τ_{ij}	Shear stress tensor (N/m^2)
V	Velocity (m/s)	α	Local water volume fraction (kg/m^3)
p	Pressure (Pa)	C_D	Droplet drag coefficient
E	Total internal energy (kJ)	K_d	Droplet inertia parameter
T	Temperature (°C)	c	Chord length (m)
t	Time (s)	β	Total collection efficiency
M	Mass (kg)	$\vec{n}$	Normal surface vector
Re	Reynolds number	f	Freezing fraction
Fr	Froude number	k	Thermal conductivity (W/m.K)
g	Gravitational acceleration (m/s^2)		

Subscripts and Superscripts

a Air

d Droplet

imp Impingement

ice Ice

∞ Stream conditions

Abbreviations

CFD Computational Fluid Dynamics

LWC Liquid Water Content

RPM Revolutions Per Minute

2.1. Introduction

Ice accretion on wind turbine blade rotors in cold and moist conditions is a critical challenge which can significantly affect the performance of wind turbine operation [1]. Ice formation on a rotating turbine blade can occur when supercooled water droplets in the atmosphere impinge on the blade surface [2]. Due to the large size of wind turbine blade rotors, it is difficult to investigate icing on full-size wind turbines in a laboratory facility. Thus, scaling methods can be an effective way to examine the icing characteristics on a turbine blade surface. Similar scaling methods are used in the aerospace industry for aerodynamic scaling of aircraft [3].

CFD numerical simulations can be used to predict the impacts of icing on wind turbines operating in cold environments [4-6]. Atmospheric conditions of high liquid water content and low temperatures near the freezing point, or environments with high convective cooling rates, can significantly impact wind turbine performance [7]. The formed ice mechanisms are influenced by the atmospheric conditions and usually divided into two main types [8]. Rime ice develops when impinging water freezes upon impact with the object surface, usually when the temperature is significantly below the freezing temperature. Glaze ice occurs in warmer conditions in which impinged droplets partially freeze on contact with the object surface while the remaining water gradually freezes when running back further downstream along the object surface [8].

The icing process is strongly influenced by the cooling effect of the surrounding air, and by the energy released through evaporation. When the local temperature is near the freezing point, only a

fraction of the water droplets freezes upon impact with an exposed surface. The remaining water is free to run back and freeze downstream, driven by shear stresses, gravity and in the case of wind turbines, rotational forces [9]. Ice accretion can degrade the aerodynamic characteristics of a rotating wind turbine rotor [10, 11]. Previous research indicated that the wind turbine rotor angular speed has a significant impact on the ice quantity [12, 13]. Combined changes in blade section chord length and relative flow velocity can significantly affect the ice accretion process. In this study, variable rotational speeds and operating/icing conditions are investigated on two similar blade section models.

2.2. Methodology

2.2.1. Formulation of Flow, Droplet and Icing Process Equations

The Navier-Stokes equations are complex equations to use and solve. These coupled time-dependent non-linear equations require many approximations to obtain analytical solutions. Numerical methods need to be applied to solve these equations so that they can provide insight into the behaviour of flows in generalized systems or complicated geometries. Some computational approximations can be applied to reduce the complexity of these equations and allow simulations to run more rapidly without losing significant accuracy. The steady-state solution of the Reynolds-averaged Navier-Stokes (RANS) equations is separated from the time-varying fluctuations within the system, which will subsequently include turbulence under a variety of flow regimes. Many more CFD models have emerged from RANS simulations and the use of empirical turbulence models, some of them making their way into commercially available applications for computational fluid dynamics.

Numerical modeling of an icing event around an object is achieved in ANSYS FENSAP ICE by solving firstly the air flow field around the blade using the FENSAP solver. This solves the partial differential equations for the conservation of mass, momentum and energy. The continuity equation for the carrier air phase is given by:

$$\frac{D\rho_a}{Dt} + \vec{\nabla} \cdot \left(\rho_a \vec{V_a}\right) = 0 \tag{1}$$

The continuity equation for the dispersed droplet phase is:

$$\frac{D\alpha}{Dt} + \vec{\nabla} \cdot \left(\alpha \vec{V_d}\right) = 0 \tag{2}$$

where α and V_d are the water volume fraction and droplet velocity, respectively. The Navier-Stokes equation is:

$$\frac{\partial \rho_a \vec{V_a}}{\partial t} + \vec{\nabla} \cdot \left(\rho_a \vec{V_a} \vec{V_a}\right) = \rho_a \vec{g} - \nabla p_a + \mu_a \nabla^2 \vec{V_a} \tag{3}$$

where ρ_a is the air density, V_a is the air velocity. The air conservation of energy equation can be written as:

$$\frac{\partial \rho_a E_a}{\partial t} + \vec{\nabla} \cdot \left(\rho_a \vec{V_a} H_a\right) = \rho_a \vec{g} \cdot \vec{V_a} + \vec{\nabla} \cdot \left(k_a \left(\vec{\nabla} T_a\right) + V_i \tau^{ij}\right) \tag{4}$$

where E_a, H_a, and k_a are the internal energy, enthalpy and the thermal conductivity, respectively. Then by solving the droplet momentum equation, the droplet collection efficiencies are obtained by using a DROP 3D solver. The Navier-Stokes equation in the droplet phase becomes:

$$\frac{\partial \left(\alpha \vec{V_d}\right)}{\partial t} + \vec{\nabla} \cdot \left(\alpha \vec{V_d} \vec{V_d}\right) = \left(\frac{C_D \cdot Re_d}{24 K_d}\right) \alpha V_{a,\infty} + \alpha \left(1 - \frac{\rho_a}{\rho_d}\right) \frac{1}{Fr^2} \tag{5}$$

where K_d is the droplet inertia parameter, and Re_d is the droplet-based Reynolds number; which are defined as:

$$K_d = \frac{\rho_d {d_d}^2 V_{a,\infty}}{18\mu_a c} \tag{6}$$

$$Re_d = \frac{\rho_d d_d V_{a,\infty}}{\mu_a} \tag{7}$$

The collection efficiency can be defined as:

$$\beta = -\frac{\alpha \vec{V}_d \cdot \vec{n}}{LWC\ V_{a,\infty}} \tag{8}$$

where α is the local water volume fraction and $\vec{n}$ is the surface normal vector. The thermodynamics of the icing/freezing process uses ICE 3D to compute the ice mass quantities, predict ice shapes, and determine the freezing fraction and the energy transfer rates due to total water impinged, convection heat transfer, evaporation/sublimation, radiation, sensible heat and energy of ice formation. The Reynolds number for the air flow can be calculated by:

$$Re_a = \frac{\rho_a V_{a,\infty} c}{\mu_a} \tag{9}$$

where $V_{a,\infty}$ is the relative flow stream velocity (includes both rotational and linear speeds). The total mass of water impingement can be calculated by:

$$M_{imp} = V_{a,\infty} LWC A_{imp} \beta t \tag{10}$$

The freezing fraction *f,* can be defined as the proportion of the total mass of liquid entering the control volume that freezes in that control volume, expressed as:

$$f = \frac{M_{ice}}{M_{imp}} \tag{11}$$

2.2.2. Computational Domain and Mesh Discretization

CFD numerical analysis of the air flow, droplet impingement and ice accretion are obtained with an ANSYS FENSAP-ICE solver. For each model, a hybrid computational grid is constructed of

approximately 0.6 million elements after mesh refinement attempts. Boundary conditions for the domain (see Fig. 2.1) include the inlet, exit, slip outer wall and inner non-slip wall for the blade section. The mesh near the blade wall is properly sized to ensure accurate flow field simulations using a desired Y+ value of 1. Fine grid elements with a first boundary layer thickness of 1×10^{-5} m over the blade section surface with a growth rate of 1.1 are constructed.

Each NACA 4415 blade section is located at a one-third position from the inlet boundary to avoid reversed flow in the wake region and successfully achieve a converged solution. Steady-state simulations are achieved using a rotating frame of reference method. When solving the equations in the relative frame of reference, the inlet flow is defined as absolute (i.e. not rotating with the grid), since it s circular and its center lies on the axis of rotation. The inflow velocity is co-linear with the axis of course; this leads to a steady-state solution. The Spalart-Allmaras turbulence model uses a RANS approach and achieves a stable solution with a streamlined upwind artificial viscosity. It involves a single governing kinematic equation to describe turbulent flow. Compared with many existing turbulence models, the model offers a good trade-off between computational cost and solution accuracy. This model has proved reliable for attachment and moderate separation flows and is well-suited for the cases discussed in this section. The model was developed specifically for aerodynamic applications of wall-bound systems and turbomachines. A one-equation Spalart Allmaras turbulence model is used for modeling of the turbulent flow around the blade section. Convergence for air flow and droplet residuals are achievied.

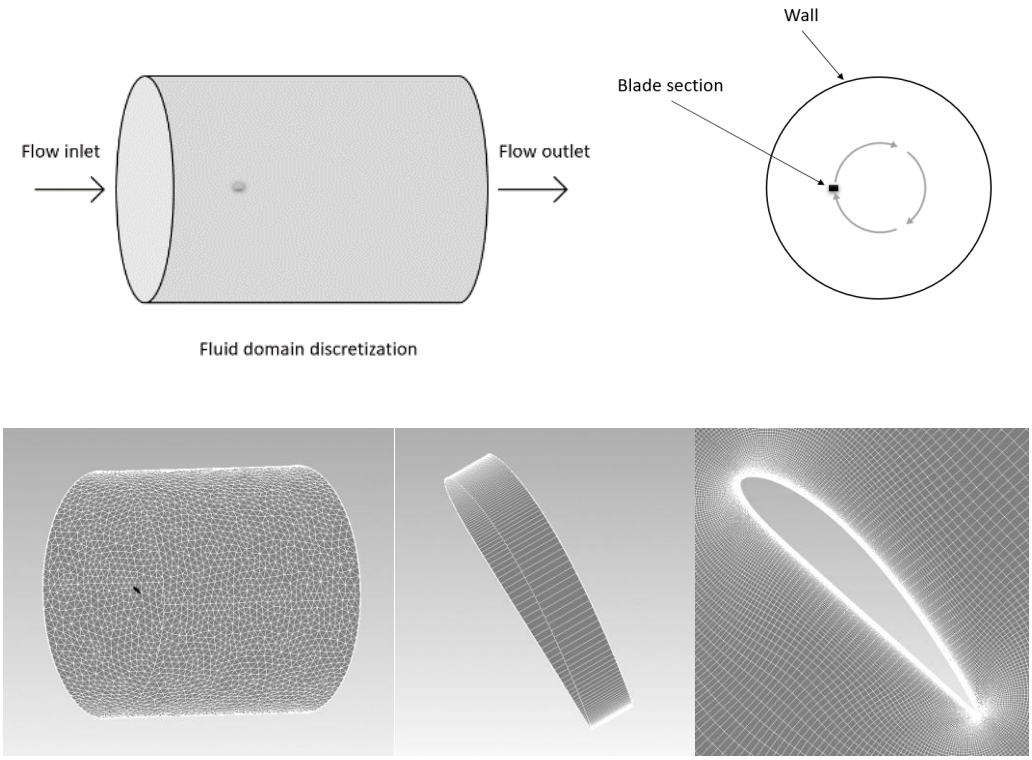

Figure 2.1. Discretization of cylindrical domain with the flow inlet, flow outlet and slip wall condition.

2.2.3. Test Conditions

Two similar blade geometries are considered in this study – Model A: (Chord 0.5 m, Spanwise 0.1 m) and Model B: (Chord 1 m, Spanwise 0.2 m). The two similar models, NACA 4415 blade sections, have a scale factor of 2. Each blade model is located at a distance from the axis of rotation and rotates in the clockwise direction. The same icing condition is applied on both models. Each section is tilted at an angle of 45 degrees. The simulated test case conditions (case 1) for a variable rotational speed investigation are shown in Table 2.1.

Table 2.1. Case 1 test conditions

Parameter	Value
Wind speed [m/s]	10
Rotational speed [RPM]	0, 10, 20, 30, 40, 50, 60
Rotational distance [m]	1
Icing temperature [°C]	-6
Liquid water content [g/m^3]	5
Icing time [mins]	30
Droplet size [µm]	50

The simulated test conditions for case 2, which maintain a relative Reynolds number and speed ratio over each blade model, are shown in Table 2.2.

Table 2.2. Case 2 test conditions

Parameter	Model A	Model B
Wind speed [m/s]	18.1	9.1
Rotational speed [RPM]	35	18
Relative speed [m/s]	25.6	12.8
Rotational distance [m]	5	
Icing temperature [°C]	-6	
Liquid water content [g/m^3]	1	
Icing time [mins]	60	
Droplet size [µm]	30	
Reynolds number	10^6	
Speed ratio	1	

2.3. Results and Discussion

This section discusses and analyses the changes in the flow field (air and droplets) during an icing event on two NACA 4415 similar blade sections. Significant changes are compared at different operating/icing conditions.

2.3.1. Air and Droplet Flow Fields

For case 1, air and droplet velocity contours are obtained for the two similar blade sections using FENSAP ICE and DROP 3D solvers, at different rotational speeds, as shown in Fig. 2.2. Droplet contours are like air velocity contours but with slightly different ranges. Only air velocity contours with legends are shown and both air and droplet velocity ranges are indicated under each contour. Results show minimal changes in the velocity upper magnitude. The results indicate that with a faster blade rotation, there is more flow attachment to the blade suction side, and thus more lift can be developed. At the same operating conditions in terms of rotational speed, distance from the rotation and linear wind speed, the velocity contours over similar blade sections remain almost the same.

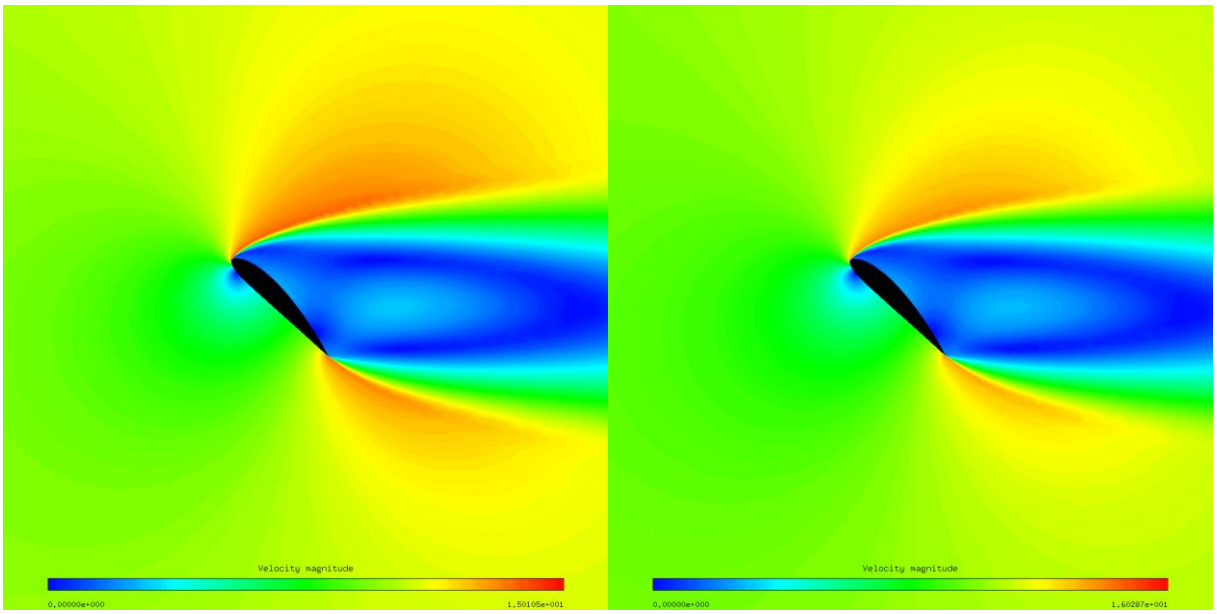

V_a (0 m/s - 15.01 m/s)

V_d (0 m/s - 14.54 m/s)

V_a (0 m/s - 16.02 m/s)

V_d (0m/s - 14.56 m/s)

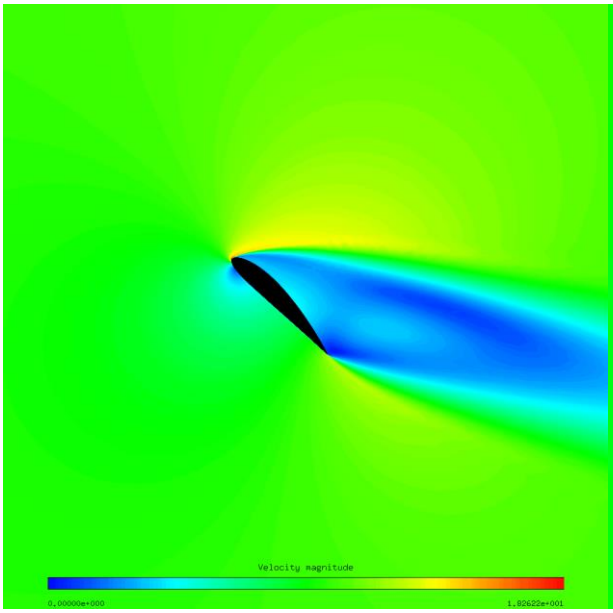

V_a (0 m/s - 18.26 m/s)

V_d (0 m/s - 15.01 m/s)

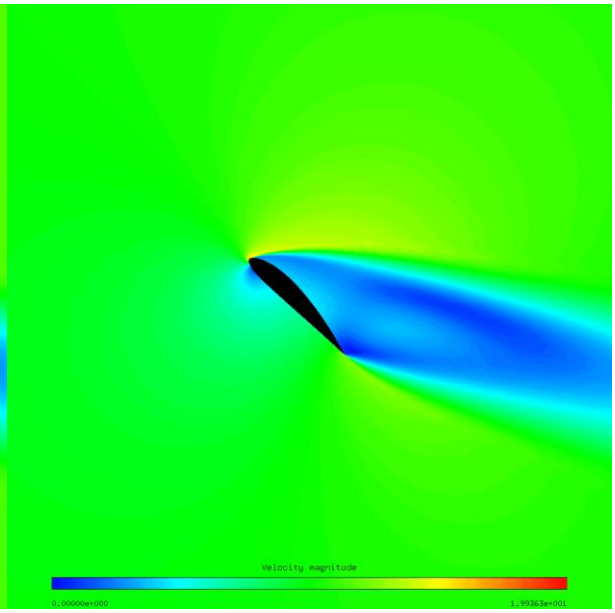

V_a (0 m/s - 19.93 m/s)

V_d (0 m/s - 16.60 m/s)

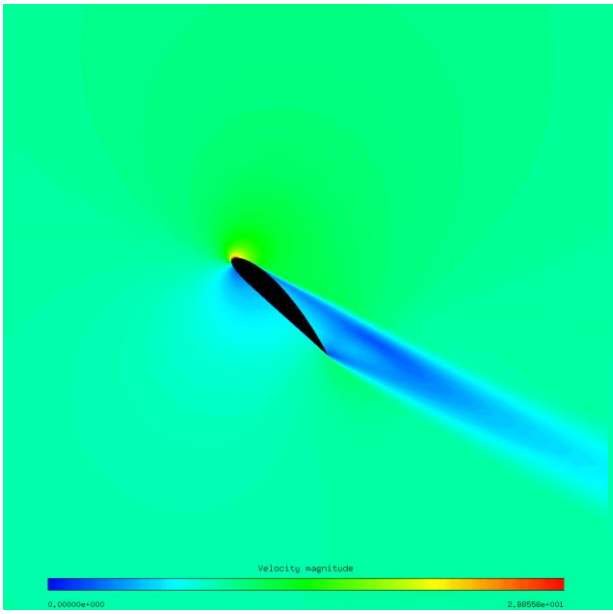

V_a (0 m/s - 28.85 m/s)

V_d (0 m/s - 21.82 m/s)

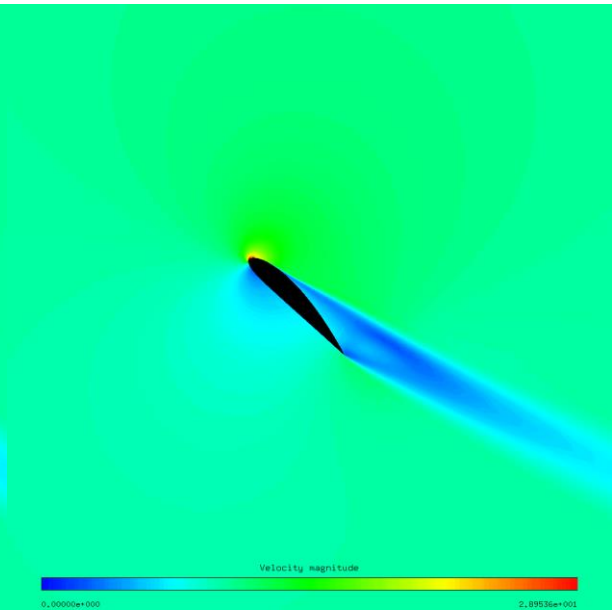

V_a (0 m/s - 28.95 m/s)

V_d (0 m/s - 24.76 m/s)

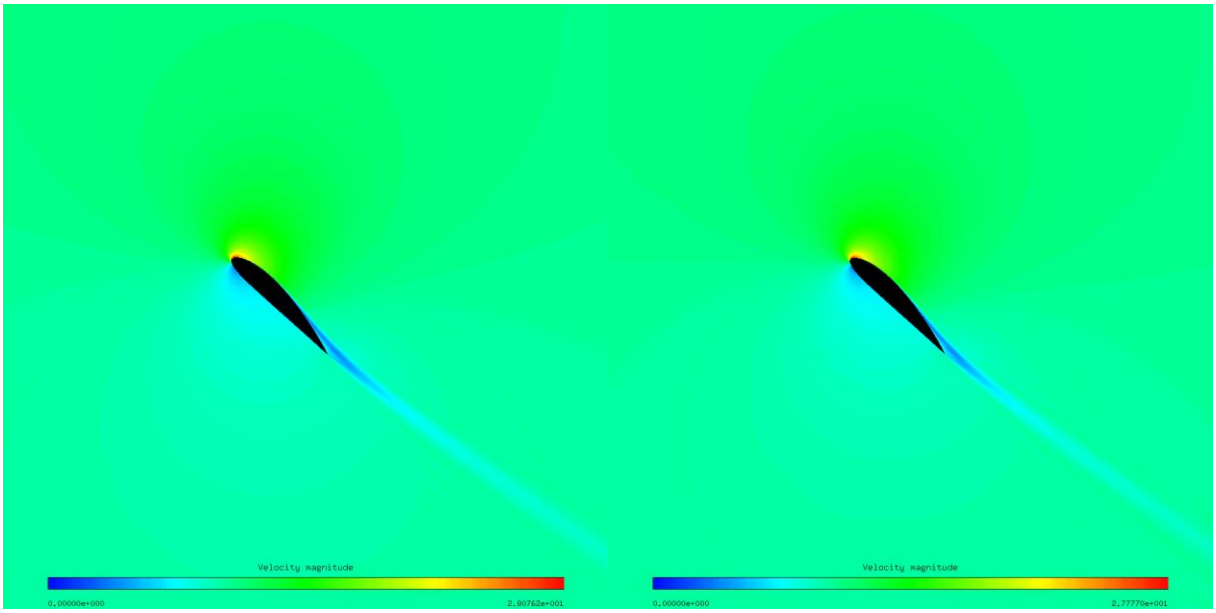

Va (0 m/s - 28.07 m/s)

Vd (0 m/s - 22.55 m/s)

Va (0 m/s - 27.77 m/s)

Vd (0 m/s - 25.10 m/s)

Figure 2.2. Flow field around Model A and Model B at variable RPM (air and droplet velocity ranges).

2.3.2. Pressure Distribution

For case 1, pressure coefficients over two similar blade sections are obtained at different rotational speeds. As shown in Fig. 2.3, plots are presented for a comparison between the models. For both model sections, slight changes are present in the pressure coefficient along the pressure and suction sides of the blade section surfaces. The blade's top surface represents the suction side (i.e. negative values) and the blade's bottom surface represents the pressure side (i.e. positive values). Results show that at lower rotational speeds, lower values for the pressure are expected on the suction side of a blade section.

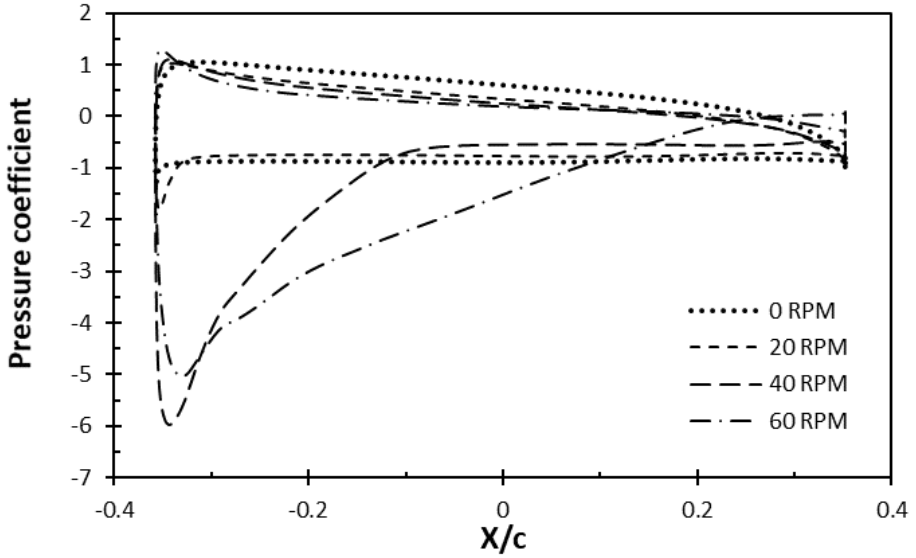

Model A

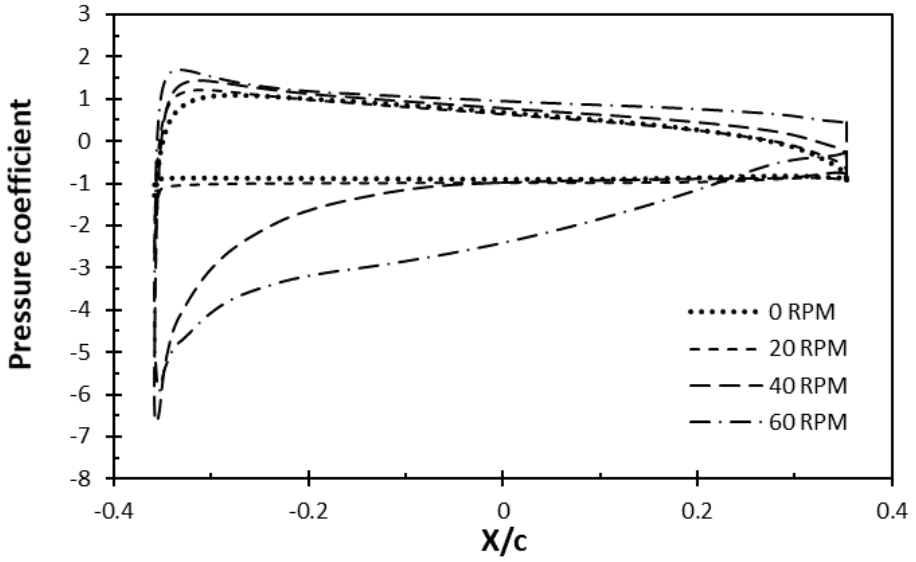

Model B

Figure 2.3. Pressure coefficient plots at variable RPMs.

2.3.3. Droplet Impingement / Collection

The total collection efficiency is a measure of the total water collected by the object (i.e. airfoil). This is a ratio of the actual mass of impinging water to the maximum value that would occur if the

droplets followed straight-line trajectories. For case 1, collection efficiency plots are obtained for both similar blade sections (Fig. 2.4). Results indicate that for Blade Model A (i.e. smaller blade section), higher collection efficiency values are predicted when compared to Model B (i.e. larger blade section). Also, results show that at lower rotational speeds, lower collection efficiency values are predicted.

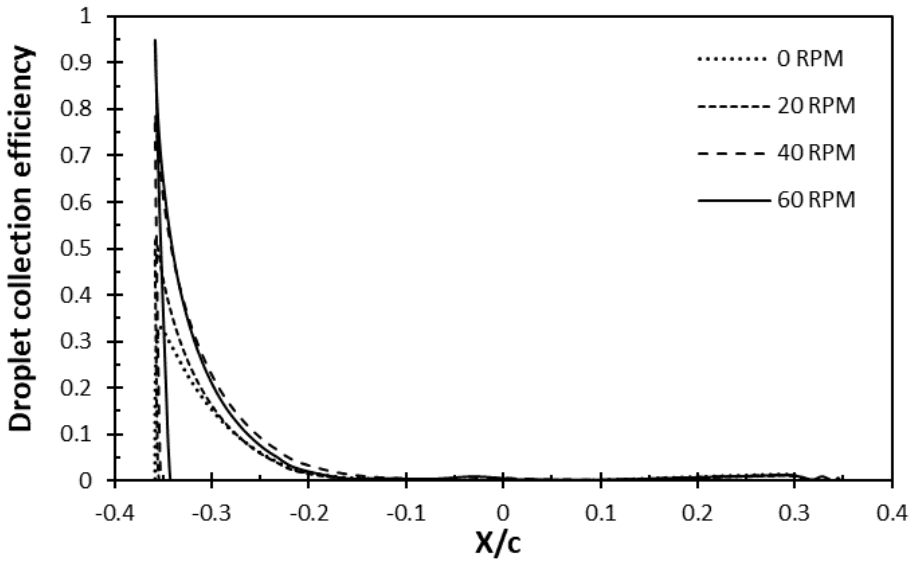

Model A

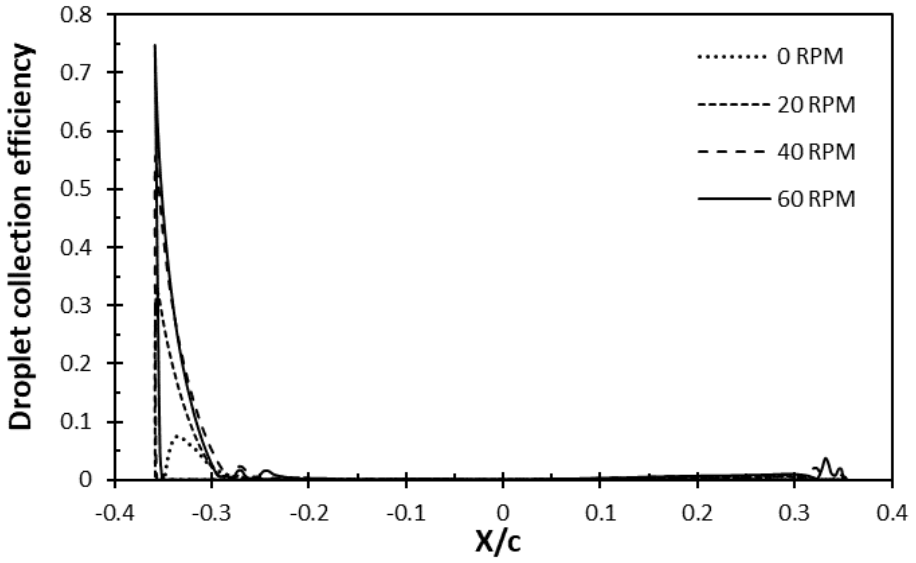

Model B

Figure 2.4. Droplet collection efficiency plots at variable RPM.

2.3.4. Ice Mass Accumulation

For case 1, the relative flow Reynolds number is calculated based on the characteristic chord length, rotational and linear speed over the blade section and flow properties. As illustrated in Fig. 2.5, higher Reynolds numbers (due to the increase in the characteristic length of the geometry, i.e. blade chord length and rotational speeds) significantly impact the quantity of ice accumulation.

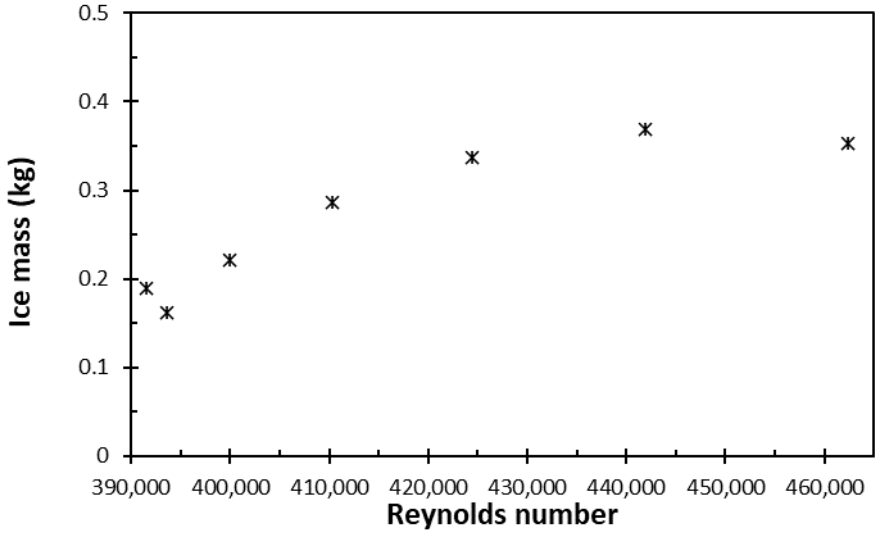

Model A

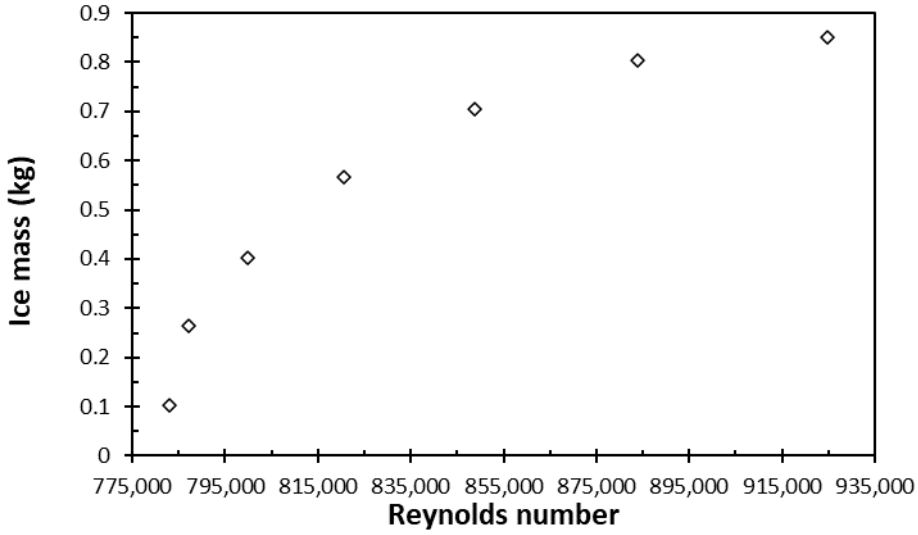

Model B

Figure 2.5. Ice quantities at variable relative flow Reynolds numbers.

2.3.5. Ice Distribution

For Case 1, ice shapes for both blade sections at varied rotational speeds are presented in Fig. 2.6. Ice shapes are formed at the leading edge of the blade where the majority of the droplet collection occurs. Results indicate that ice shapes on the smaller blade section, Model A, cover more surface area when compared to the larger blade. However, more ice mass accumulates on the larger blade, Model B. This suggests that ice horns are more likely to form on smaller blade sections, characterized by small chord lengths.

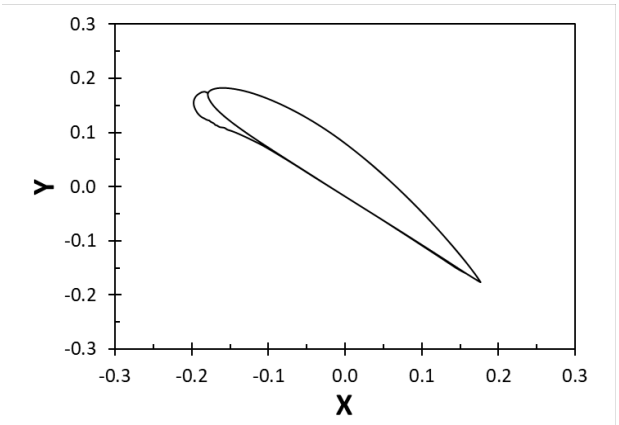

(Model A 0 RPM)

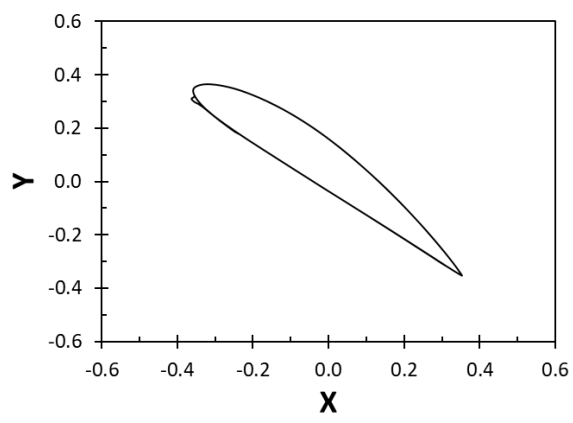

(Model B 0 RPM)

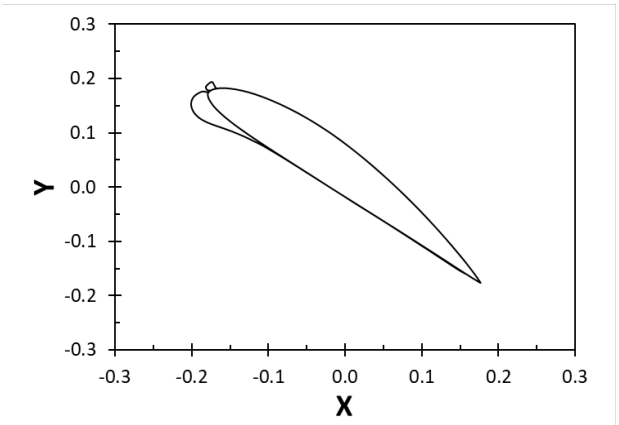

(Model A 20 RPM)

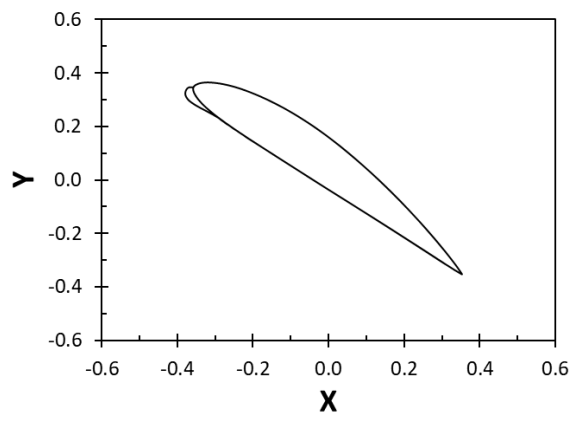

(Model B 20 RPM)

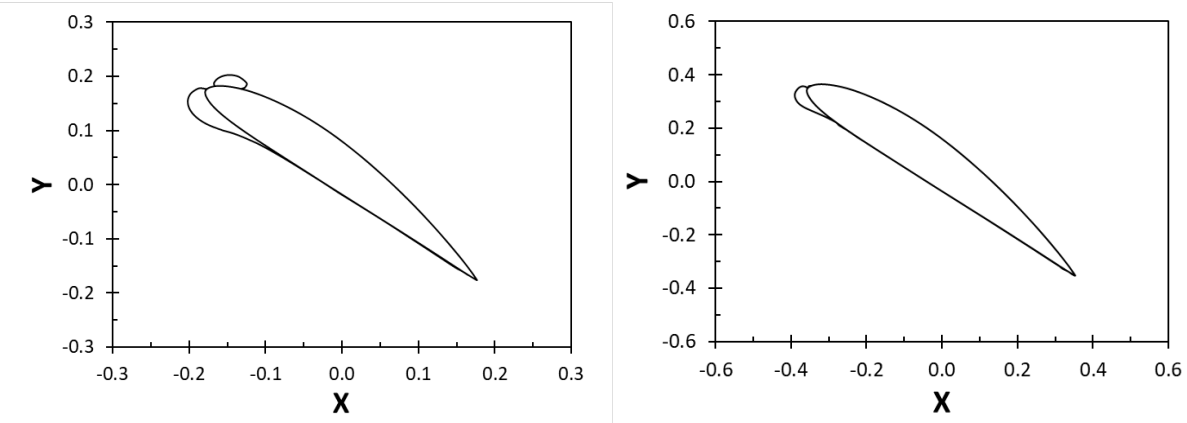

(Model A 40 RPM) (Model B 40 RPM)

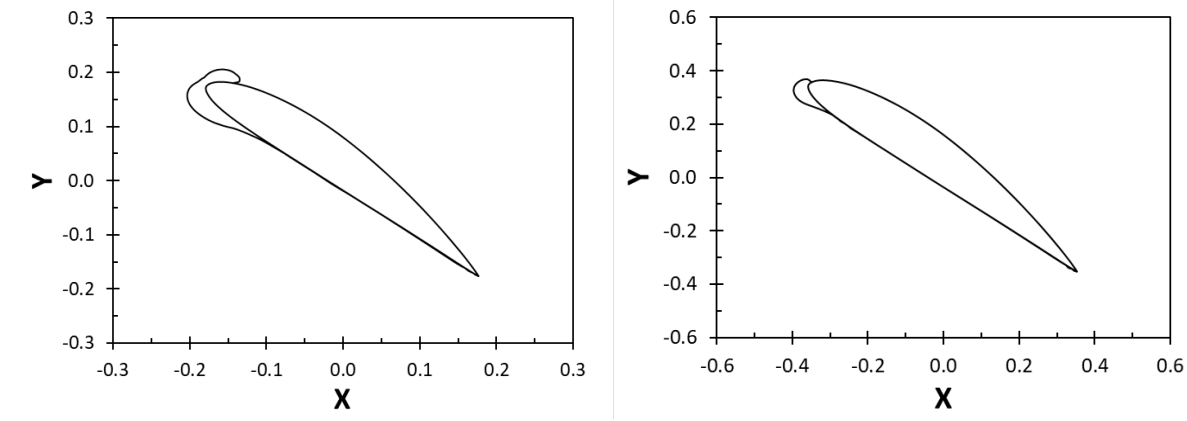

(Model A 60 RPM) (Model B 60 RPM)

Figure 2.6. Ice shapes around Model A (left) and Model B (right) at variable RPM.

2.3.6. Speed Ratio and Relative Reynolds Number

For Case 2, the relative flow Reynolds number and speed ratio over each blade section are maintained to investigate the significant changes in the (air and droplet) flow fields and ice accretion characteristics. The velocity field (Fig. 2.7) predicts an almost identical distribution of flow around both blade models, however, different velocity ranges for air and droplets are predicted. Predictions for the pressure coefficient show no significant changes over both blades on suction and pressure surfaces (Fig.2.8). Plots for droplet collection over both blade surfaces are

presented in Fig. 2.9, which predict higher collection efficiency values for the smaller blade section, Model A. By comparison, the predicted ice shapes for both models are shown in Fig. 2.10. The predicted ice mass for the smaller blade section, Model A, is higher than the larger blade section, Model B, due to the higher velocity ranges over the smaller characteristic chord length of model A. This highlights the impact of maintaining both the relative flow number and speed ratio on the icing process.

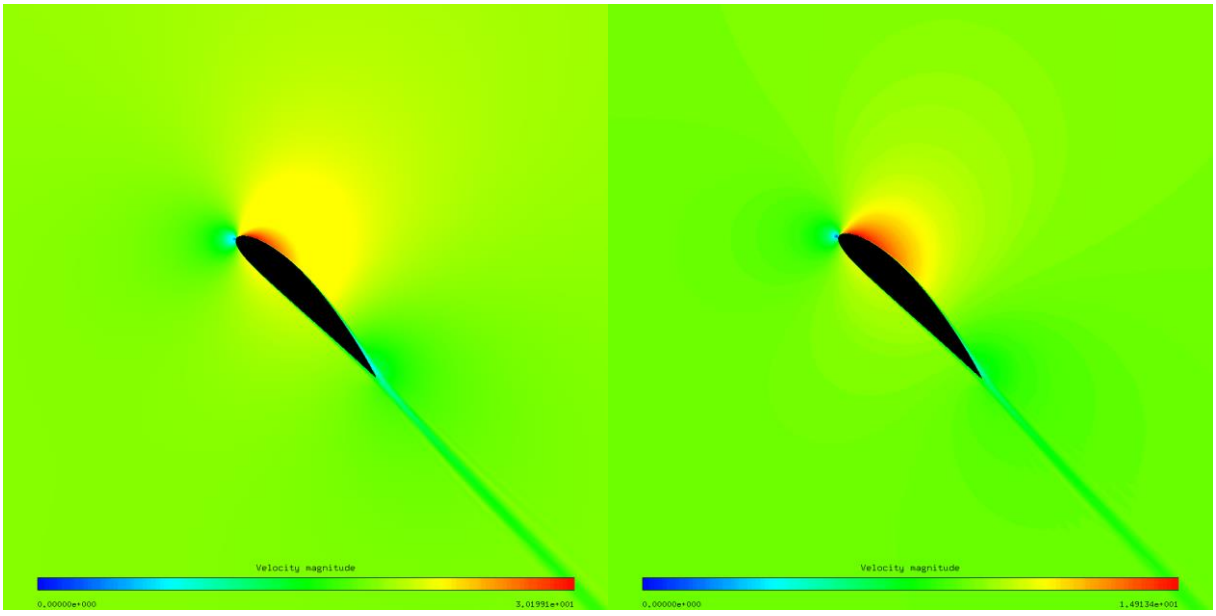

V_a (0 m/s - 30.19 m/s) V_a (0 m/s - 14.91 m/s)

V_d (0 m/s - 31.24 m/s) V_d (0 m/s - 16.34 m/s)

Figure 2.7. Flow field around Model A (left) and Model B (right) at same relative Reynolds number and speed ratio (air and droplet velocity ranges).

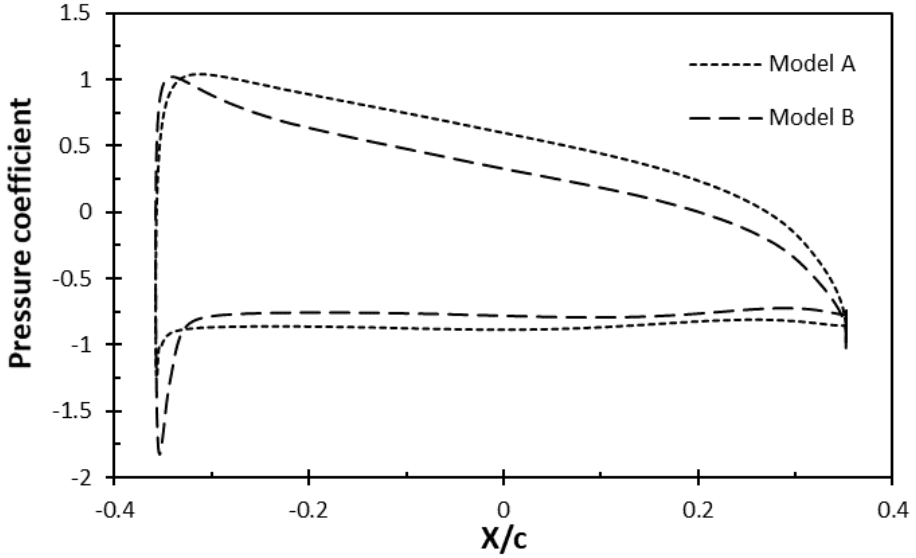

Figure 2.8. Pressure coefficients at same relative Reynolds number and speed ratio.

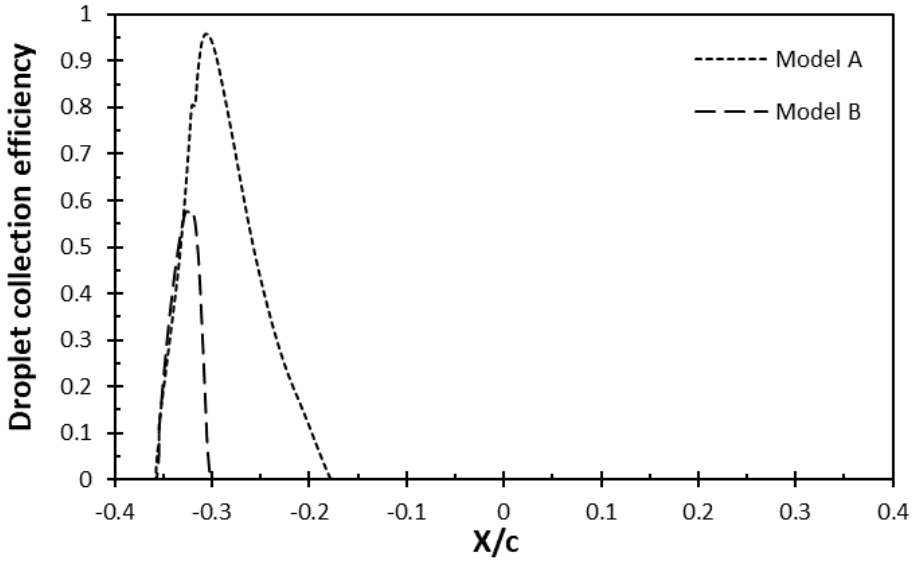

Figure 2.9. Droplet collection efficiency at same relative Reynolds number and speed ratio.

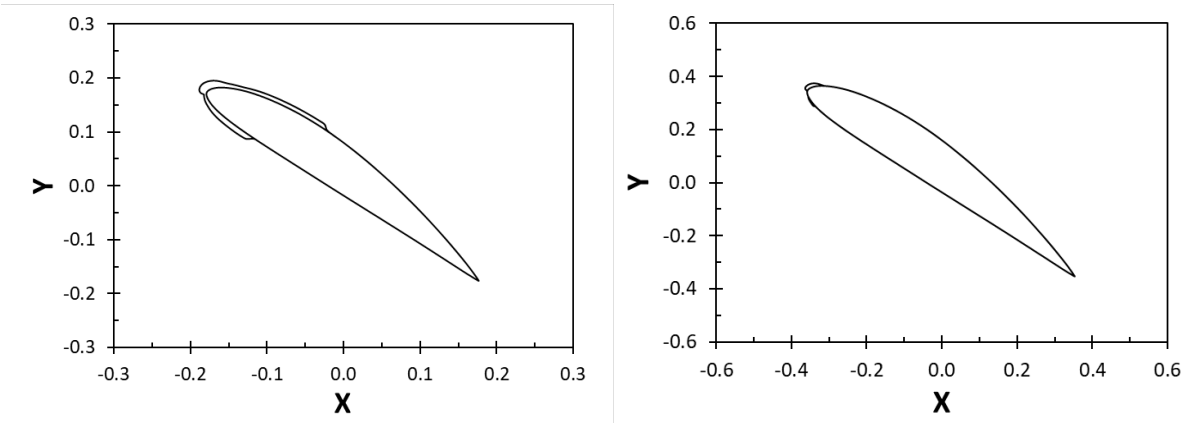

Figure 2.10. Formed ice shapes around both blade models at same relative Reynolds number and speed ratio.

2.3.7. Mass Conservation and Energy Conservation

Considering Cases 1 and 2, for both blade models, impinging water mass, ice mass and energy exchange due to water impingement, the convective heat transfer and ice formation are predicted and presented in Table 2.3. For Case 1, predictions suggest the large blade section develops higher energy rates when compared to Model A. For Case 1, predictions suggest the smaller blade section tends to have a slightly lower freezing fraction when compared to the larger blade. Higher energy rates during the freezing process occur at higher speeds. For Case 2, predictions suggest large differences in water collection magnitudes and ice masses between both models, when the relative Reynolds number and speed ratio are maintained on both models.

Table 2.3. Tabulated values

CASE 1						
Model A						
Run No.	M_{imp} (kg)	M_{ice} (kg)	E_{imp} (kJ)	E_{ice} (kJ)	E_{conv} (kJ)	n
0 RPM	0.19	0.18	-4.82	65.44	57.34	0.94
10 RPM	0.21	0.16	-5.51	56.17	39.38	0.76
20 RPM	0.24	0.22	-6.25	76.72	58.90	0.91
30 RPM	0.30	0.28	-7.79	99.02	66.97	0.93
40 RPM	0.36	0.33	-9.35	116.67	74.96	0.91
50 RPM	0.41	0.36	-10.49	127.75	81.85	0.87
60 RPM	0.40	0.35	-10.19	122.30	76.63	0.87
CASE 2						
Model A						
Run No.	M_{imp} (kg)	M_{ice} (kg)	E_{imp} (kJ)	E_{ice} (kJ)	E_{conv} (kJ)	n
1	0.22	0.21	-4.69	74.37	42.01	0.95
CASE 1						
Model B						
Run No.	M_{imp} (kg)	M_{ice} (kg)	E_{imp} (kJ)	E_{ice} (kJ)	E_{conv} (kJ)	n
0 RPM	0.11	0.10	-2.77	36.01	23.62	0.90
10 RPM	0.26	0.26	-6.68	91.32	84.63	1
20 RPM	0.40	0.40	-10.21	139.57	129.35	1
30 RPM	0.56	0.56	-14.34	195.97	181.45	1
40 RPM	0.71	0.70	-17.84	243.71	224.97	0.98
50 RPM	0.81	0.80	-20.39	277.86	250.76	0.98
60 RPM	0.85	0.84	-21.62	294.19	260.65	0.98
CASE 2						
Model B						
Run No.	M_{imp} (kg)	M_{ice} (kg)	E_{imp} (kJ)	E_{ice} (kJ)	E_{conv} (kJ)	n
1	0.12	0.11	-3.12	40.6	25.4	0.91

2.4. Conclusions

In this study, scaling effects on the flow field and ice accretion on rotating turbine blades were investigated at different flow conditions. Two similar NACA 4415 blade sections share a scale factor of 2. They were investigated numerically using ANSYS FENSAP ICE. Two cases were examined, one by rotating both similar sections at variable rotating speeds (i.e. ranges from 0 to 60

RPM) and same flow conditions, and the other case by maintaining the value of the relative flow Reynolds number and speed ratio over each similar blade section.

For Case 1, velocities over the two similar blades are almost similar in terms of the distribution of the flow around the blade at different RPM. Slight changes are found in the magnitudes of the velocity ranges. More flow attachment on the suction side of the blade is found at higher RPM. The droplet collection is found at the leading edge for both blade models. A smaller blade section has more droplet collection efficiency magnitude when compared to the larger section, which demonstrates the resulting large icing area coverage over its surface. The relative flow Reynolds number greatly impacts ice mass. This suggests that large blade sections are characterized by large characteristic lengths compared to the smaller sections (i.e. chord length), operating at the same flow conditions and rotational speeds, which can form more ice mass.

Results showed that heat transfer rates and freezing fraction values during the icing process over the small blade section are slightly lower when compared to the large blade section. For Case 2, results indicated higher velocity magnitudes over the small blade. Minimal changes are found in the pressure distributions between both blade sections. More droplet collection is found on the small blade section. Larger icing area coverage and ice mass are found over the small blade section. The results provide useful predictions for the changes in the flow field and ice accretion on wind turbine blade sections.

References

[1] Feng, F., Li, S., Li, Y., & Tian, W. (2012). Numerical simulation on the aerodynamic effects of blade icing on small scale Straight-bladed VAWT. Physics Procedia, 24, 774-780.

[2] Battisti, L. (2015). Wind turbines in cold climates: Icing impacts and mitigation systems. Springer.

[3] Li, Y., Sun, C., Jiang, Y., & Feng, F. (2019). Scaling method of the rotating blade of a wind turbine for a rime ice wind tunnel test. Energies, 12(4), 627.

[4] Switchenko, D., Habashi, W., Reid, T., Ozcer, I., & Baruzzi, G. (2014). FENSAP-ICE Simulation of Complex Wind Turbine Icing Events, and Comparison to Observed Performance Data. In 32nd ASME Wind Energy Symposium (p. 1399).

[5] Sultana, K.R., Dehghani, S.R., Pope, K., & Muzychka, Y.S. (2017). Numerical techniques for solving solidification and melting phase change problems. Numerical Heat Transfer, Part B: Fundamentals: 129-145.

[6] Ibrahim, G.M., Pope, K., and Muzychka, Y.S. (2018). Transient ice accretion on wind turbine blades. Wind Engineering 42(6): 596-606.

[7] Kraj, A. G., & Bibeau, E. L. (2010). Measurement method and results of ice adhesion force on the curved surface of a wind turbine blade. Renewable Energy, 35(4), 741-746.

[8] Reid, T., Baruzzi, G., Ozcer, I., Switchenko, D., & Habashi, W. FENSAP-ICE simulation of icing on wind turbine blades, part 1: performance degradation. In 51st AIAA aerospace sciences meeting including the new horizons forum and aerospace exposition (p. 750), Grapevine, Texas, (2013, January).

[9] Reid, T., Baruzzi, G., Ozcer, I., Switchenko, D., & Habashi, W. FENSAP-ICE simulation of icing on wind turbine blades, part 2: ice protection system design. In 51st AIAA Aerospace Sciences Meeting including the New Horizons Forum and Aerospace Exposition (p. 751), Grapevine, Texas, (2013).

[10] Ibrahim, G. M., Pope, K., & Muzychka, Y. S. (2018). Effects of blade design on ice accretion for horizontal axis wind turbines. Journal of Wind Engineering and Industrial Aerodynamics, 173, 39-52.

[11] Barber, S., Wang, Y., Jafari, S., Chokani, N., & Abhari, R. S. (2011). The impact of ice formation on wind turbine performance and aerodynamics. Journal of Solar Energy Engineering, 133(1).

[12] Homola, M. C., Wallenius, T., Makkonen, L., Nicklasson, P. J., & Sundsbø, P. A. (2010). Turbine size and temperature dependence of icing on wind turbine blades. Wind Engineering, 34(6), 615-627.

[13] Fu, P., & Farzaneh, M. (2010). A CFD approach for modeling the rime-ice accretion process on a horizontal-axis wind turbine. Journal of Wind Engineering and Industrial Aerodynamics, 98(4-5), 181-188.

Chapter 3

3. Ice Accretion on a Rotating Horizontal Axis Wind Turbine Blade

This study presents a numerical study of ice accretion on a 2 MW wind turbine with an 80 m rotor diameter using ANSYS FENSAP ICE software. The study investigates ice accumulaton with a focus on spanwise variability by analyzing four sections along a rotating blade. Air and droplet velocity contours, pressure distribution, droplet behavior, and ice characteristics are presented. The numerical results predict that radial distance towards the blade tip significantly impacts droplet collection and ice accretion. The results provide helpful insights for ice accretion modeling and mitigation along a blade span.

Nomenclature

A	Area (m^2)
d	Diameter (m)
V	Velocity (m/s)
p	Pressure (Pa)
T	Temperature (°C)
t	Time (s)
M	Mass (kg)
Re	Reynolds number
R	Radius (m)
Fr	Froude number
g	Gravitational acceleration (m/s^2)
μ	Dynamic viscosity (Pa·s)
ρ_d	Droplet fraction (kg/m^3)
C_d	Droplet drag coefficient
K_d	Droplet inertia parameter
c	Chord length (m)
β	Total collection efficiency
$\vec{n}$	Normal surface vector
f	Freezing fraction
k	Thermal conductivity (W/m.K)

Abbreviations

$NREL$	National Renewable Energy Laboratory
CFD	Computational Fluid Dynamics
LWC	Liquid Water Content
MVD	Median Volume Diameter
TSR	Tip Speed Ratio
RPM	Revolutions Per Minute

Subscripts and Superscripts

a	Air

d	Droplet	ice	Ice
imp	Impingement	∞	Stream conditions

3.1. Introduction

Wind turbines operating in high wind speeds and low temperatures are prone to severe ice loads [1]. For optimal wind turbine operation in cold regions, it is necessary to analyze changes in the air and droplet flow fields around the rotating blade during an icing event. Icing occurs due to the impingement of supercooled water droplets in the atmosphere, which freeze on the blade surface upon collision [2, 3]. Ice accretion on wind turbines depends on many variables including atmospheric conditions (e.g., pressure, temperature, droplet median diameter (MVD), and liquid water content (LWC)), operating conditions (e.g., wind speed, rotational speed, and tip speed ratio (TSR)), and blade design characteristics (e.g., roughness, material, airfoil, radius, and aerodynamic characteristics) [3].

Ice accretion on a wind turbine blade affects the flow behavior and degrades overall aerodynamic performance [4]. Its effects on wind turbine performance can be investigated using experimental and numerical approaches. Due to the large physical sizes, it is challenging to study icing on full-size wind turbines in a laboratory facility. Along with field measurements, computational fluid dynamics (CFD) simulations can be used to simulate, analyze and determine the performance of a wind turbine blade under icing conditions.

Past studies have shown significant power loss due to ice occurring at sections near the blade tip [5-8]. Results indicated that the ice formation in terms of its local ice mass and accreted shapes are less severe near blade root sections, as characterized by larger and thicker blade profiles. Results showed that ice growth changes significantly with the atmospheric temperature along the blade sections from the center to the tip [9]. In this study, numerical simulations are performed to

examine the airflow and droplet behavior and predicted ice accretion on a large horizontal axis wind turbine using ANSYS FENSAP-ICE software.

3.2. Methodology

3.2.1. Two-Phase Flow and Ice Accretion Modeling

Modeling of an icing event on a wind turbine blade is a complex process that involves airflow field simulations, water droplet trajectories, surface thermodynamics, and phase change computations. FENSAP [10] obtains flow field solutions by solving partial differential equations for mass conservation, momentum, and energy. The Navier-Stokes equation in a relative frame of reference for a rotating blade is given by:

$$\frac{\partial \rho_a \vec{V}_a}{\partial t} + \vec{\nabla} \cdot \left[\rho_a \vec{V}_a \vec{V}_a\right] = \rho_a \vec{g} - \nabla p_a + \mu_a \nabla^2 \vec{V}_a - \rho_a \vec{\Omega} \times \left[\vec{\Omega} \times \vec{r}\right] - 2\rho_a \left[\vec{\Omega} \times \vec{V}_a\right] \quad (1)$$

where ρ_a, μ_a, V_a, r, are air density, dynamic viscosity, air velocity, rotational speed, and distance from the axis of rotation, respectively. DROP3D [10] predicts the two-phase flow using an Eulerian approach, consisting of the Navier-Stokes equations augmented with the droplet continuity and momentum equations [11]:

$$\frac{\partial \rho_d \vec{V}_d}{\partial t} + \vec{\nabla} \cdot \left[\rho_d \vec{V}_d \vec{V}_d\right] = \frac{C_d Re_d}{24K} \rho_d \left[\vec{V}_a - \vec{V}_d\right] + \rho_d \left[1 - \frac{\rho_a}{\rho_d}\right] \frac{1}{Fr^2} \quad (2)$$

where ρ_d, V_d, Re_d, K, Fr, are the droplet's fraction, velocity, droplet Reynolds number, inertia parameter, and Froude number, respectively. This determines droplet trajectories and collection efficiencies over the entire domain and blade surface. Local, β_o, and total, β, droplet collection efficiencies are defined as:

$$\beta_o = -\frac{\rho_d \vec{V}_d \cdot \vec{n}}{LWC_\infty V_\infty} \qquad \beta = \frac{\int \beta_o dA}{A_{imp}} \quad (3)$$

where LWC_∞, A_{imp}, and $\vec{n}$ are the stream liquid water content, impingement area, and normal surface vector, respectively.

Finally, ICE3D [10] computes the surface thermodynamics and predicts ice characteristics by modeling the mass transfer and heat fluxes generated due to supercooled water droplet impingement (i.e., source of the water film), evaporation, and ice accretion (i.e., sink of the water film). This leads to ice accretion over the blade surface.

3.2.2. Computational Domain and Grid Discretization

CFD grids are constructed at specific locations of interest along the blade sections to decrease the computational demands of testing at full-size. Each separate computational grid is constructed of high-resolution hexahedral elements, ranging approximately from 256 to 438 thousand elements. Four locations along the blade span are analyzed during an icing event. Boundary conditions (Fig. 3.1) for each grid include the flow inlet, exit, a non-slip blade wall, and symmetry. A corresponding y-value of 1 is computed based on the flow conditions to ensure that the CFD domain around each blade surface is appropriately sized for an accurate simulation. Each structured grid has a boundary layer thickness of 1×10^{-5} m up to 50 m with a growth rate of 1.15 over a NACA 4418 blade surface to avoid the wake region reverse flow and achieve a converged solution.

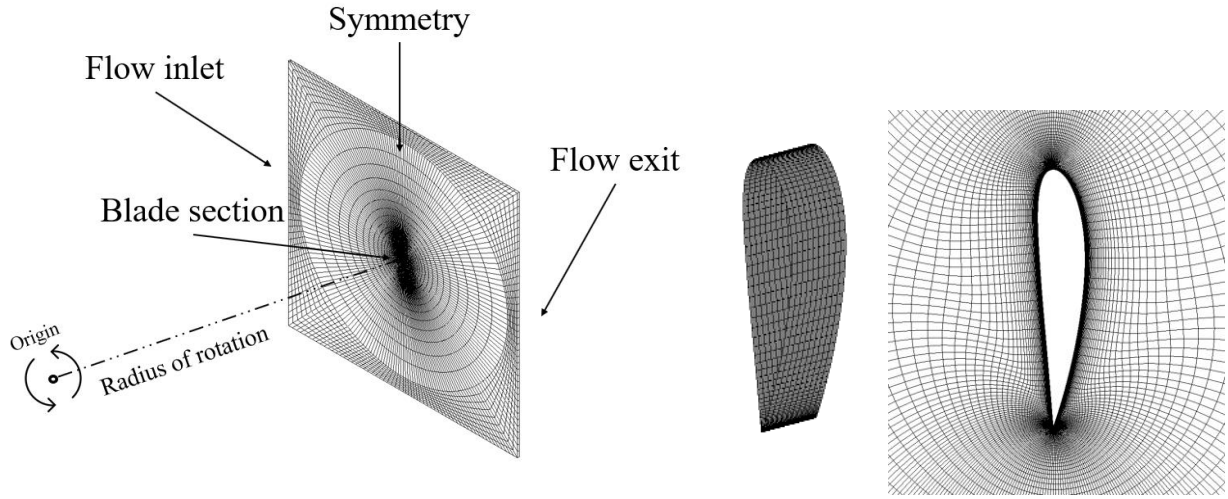

Figure 3.1. Discretization of the CFD domain and grid around blade airfoil.

3.2.3. Numerical Model and Operating Conditions

This study investigates ice accretion on a 2 MW power wind turbine model with an 80 m rotor diameter. An icing event is predicted using steady-state simulations for the flow field. A rotating frame of reference method is applied to each grid. Each blade section is set to rotate in the clockwise direction. A one-equation Spalart-Allmaras turbulence model is used to predict the turbulent flow around each rotating blade section. Compared with many existing turbulence models, the model offers a good trade-off between computational cost and solution accuracy. This model has proved reliable for attachment and moderate separation flows and is well-suited for the cases discussed in this work. The model was developed specifically for aerodynamic applications of wall-bound systems and turbomachines. The Langmuir B [10] droplet model is used with seven droplet diameters ranging from 22 μm to 55 μm by computing the droplet concentration and speed for each droplet diameter of the discrete distribution and automatically determining an averaged solution at the end of the simulation. Four sections with a blade span of 0.5 m along the blade are tested for a specific icing condition. The blade design and configuration are based on the Blade Element

Momentum (BEM) theory [12]. The theory is used to evaluate a specific blade design due to combined aerodynamic loads for different operational factors, including rotational velocity, pitch angle, and wind speed. The method requires the lift and drag coefficients as inputs in its algorithm to predict rotor aerodynamic performance. These performance coefficients are assumed using the available airfoil database for specified Reynolds numbers. After designing and applying the flow conditions, the expected aerodynamic performance from blade section rotation in the relative frame of reference can be achieved. Fig. 3.2 shows velocity triangle discretization over a rotating blade and each tested section's pitch angle and chord to radius radio.

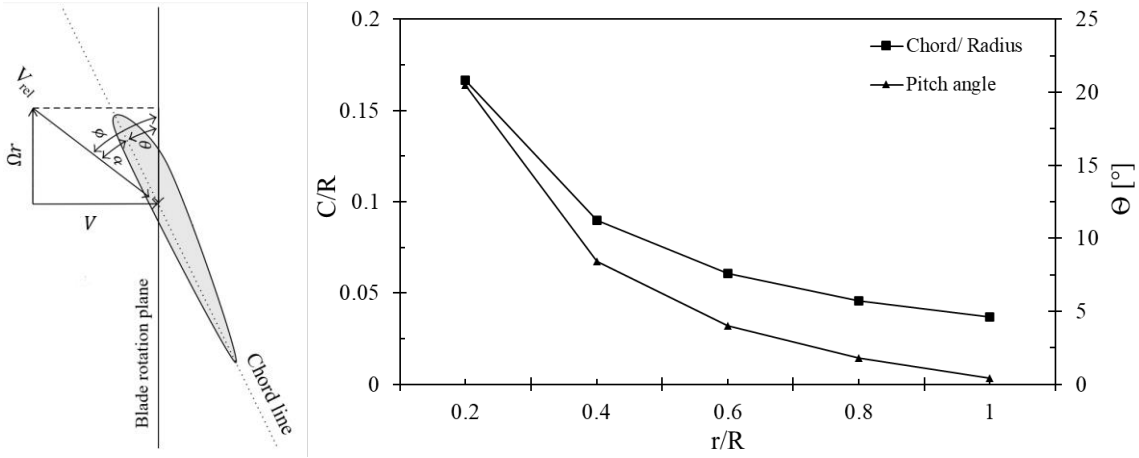

Figure 3.2. (a) Velocity triangle with aerodynamic angle discretization and (b) 40 m radius blade - tested section design specifications.

The design process includes calculations for each blade section pitch angle, chord, angle of attack based on the optimal aerodynamic characteristics of a NACA 4418 airfoil at a specific Reynolds number of 10^6, and an optimal tip speed operation of 7. The blade origin point in the XY plane is located at 30% of the chord line. The test section specifications are presented in Table 3.1. The operating conditions and icing event conditions are shown in Table 3.2.

Table 3.1. Blade characteristics

Parameter	Value			
Angle of attack, α [°]	5			
Location, r/R	0.4	0.6	0.8	1
Chord, C [m]	3.59	2.43	1.84	1.47
Rotational radius, R [m]	16	24	32	40
Local speed ratio	2.8	4.2	5.6	7

Table 3.2. Test conditions

Parameter	Value
Wind speed, V [m/s]	8.78
Rotational speed, Ω [RPM]	15
Icing temperature, T [°C]	-5
Droplet distribution - (size) [μm]	Langmuir B - (22 ~ 55)
Liquid water content, LWC [g/m^3]	0.5
Icing time, t [hrs]	3

3.3. Results and Discussion

This section presents the results of the numerical predictions, including significant changes in the flow field (air and droplets) during an icing event on a wind turbine blade with NACA 4418 airfoil sections.

3.3.1. Air and Droplet Flow Fields

Air velocity contours around the entire blade sections are obtained using the FENSAP solver. Air velocity contours with legends are presented in Fig. 3.3. Results show similar flow field behavior among different blade sections, from positions near the base (r/R = 0.4) to others near the tip (r/R = 1). However, higher velocity magnitudes exist over blade sections rotating at larger rotational distances of r/R (due to high relative speeds towards the tip).

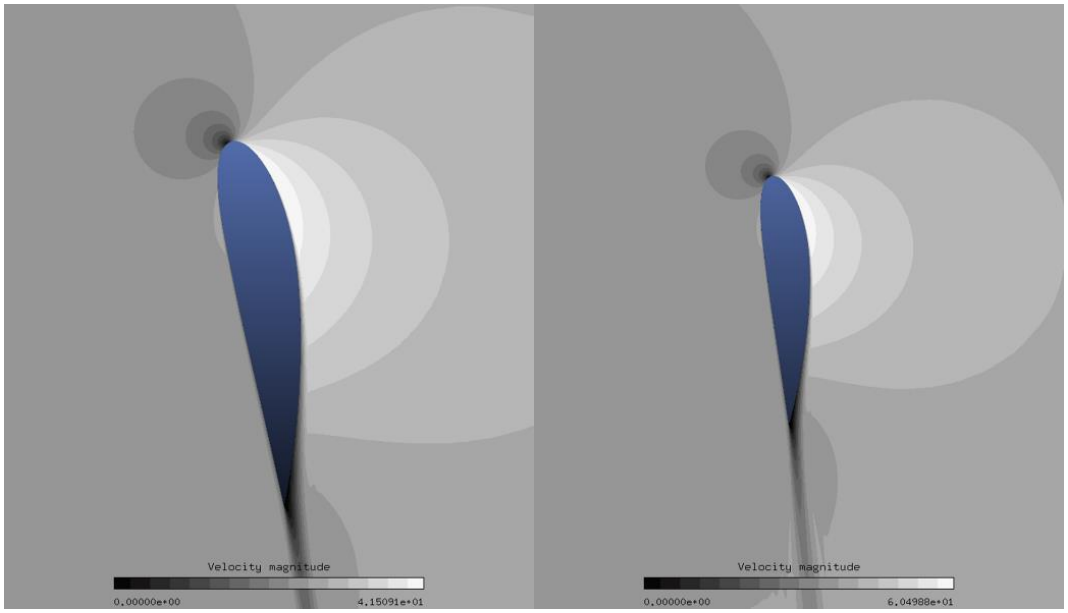

(a) r/R = 0.4 (b) r/R = 0.6

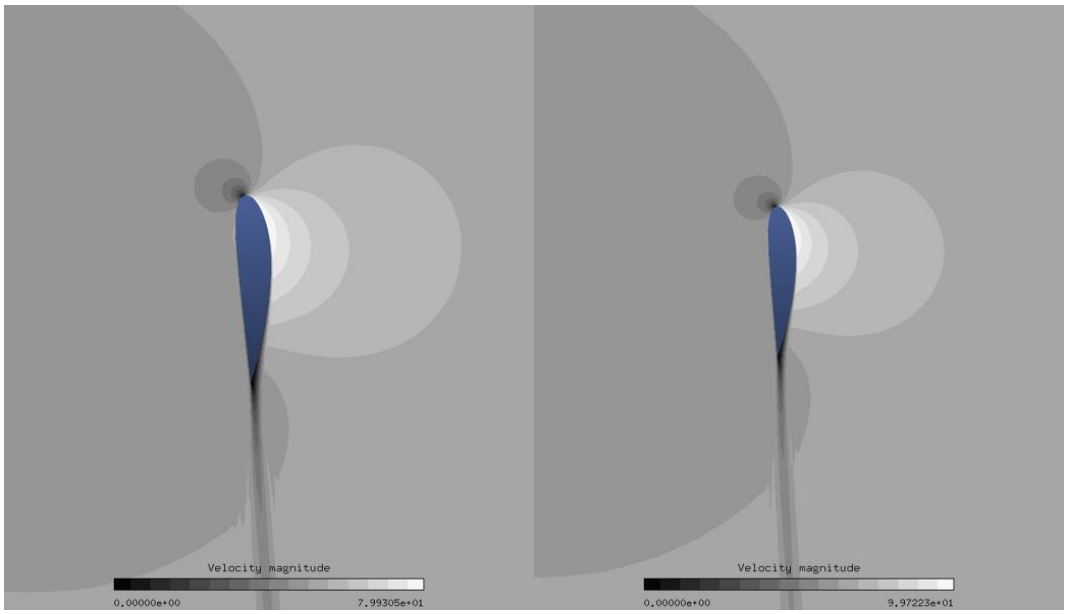

(c) r/R = 0.8 (d) r/R = 1

Figure 3.3. Airflow contours along blade span at different r/R ratios (R = 40 m).

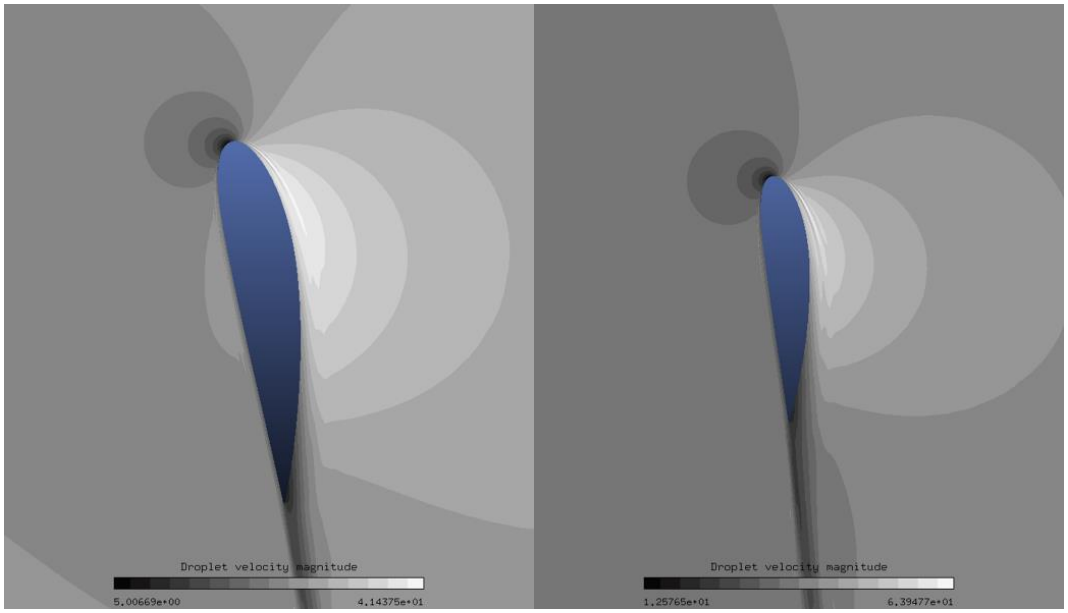

(a) r/R = 0.4 (b) r/R = 0.6

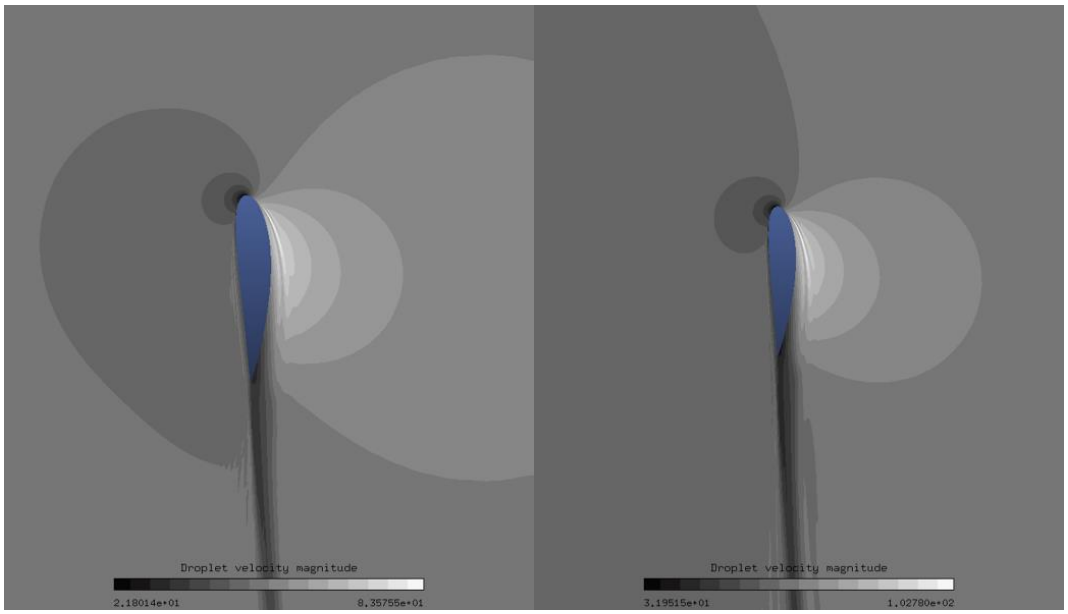

(c) r/R = 0.8 (d) r/R = 1

Figure 3.4. Droplet flow field contours along blade span at different r/R ratios (R = 40 m).

Droplet velocity contours around the entire blade sections are obtained using DROP3D software. As shown in Fig. 3.4, droplet velocity contours are similar to air velocity contours but have slightly different magnitudes. Results indicate that all droplets are in motion around the blade

at a steady-state prior to the freezing process. Lower velocity magnitudes are found at the flow stagnation region.

3.3.2. Pressure Distribution

Pressure coefficients over four different sections along the blade span are presented in Fig. 3.5. Results indicate slight changes in the pressure field due to each blade pitch angle variation. The right side represents the pressure side (positive values), and the left side represents the suction side (negative values). The pressure field significantly affects the aerodynamic characteristics. The results indicate these operating conditions. An optimal blade design could result in similar pressure fields along the blade span sections since sustained performance along the blade span is necessary.

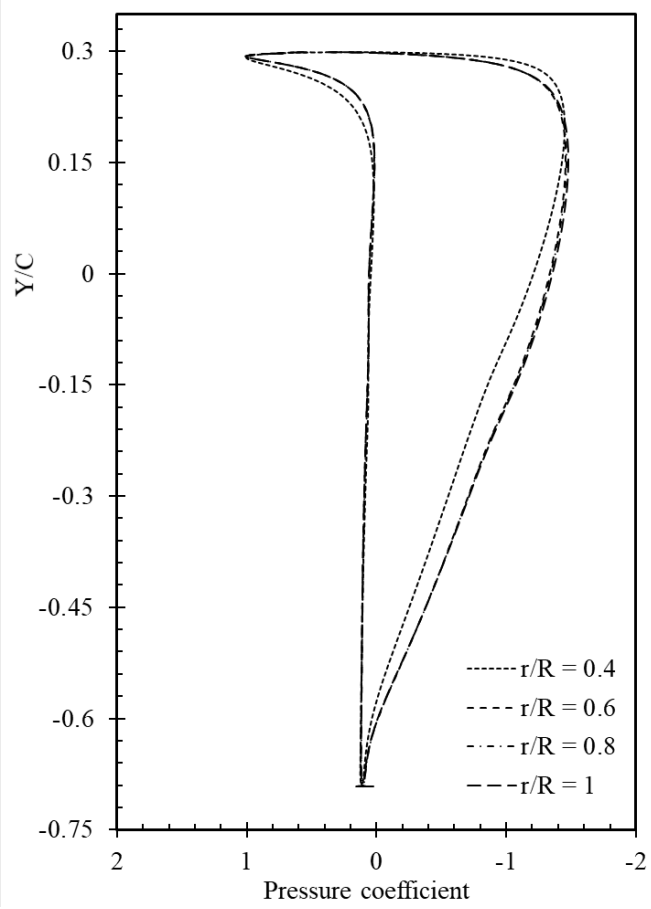

Figure 3.5. Pressure coefficients along blade span at different r/R ratios (R = 40 m).

3.3.3. Droplet Impingement/ Collection

The DROP3D solver obtains droplet water volume fractions in kg/m^3 over the entire domain, including the blade surface. It uses droplet velocity magnitudes to compute local and total collection efficiencies. Fig. 3.6 shows droplet LWC contours over each blade section. Results indicate a hollow region with no droplet attachment towards the blade trailing edge, illustrating the droplet's collection at the leading edge. Fig. 3.7 shows local droplet LWC magnitudes along each blade section in the blade chordwise vertical direction Y/C and blade thickness-wise horizontal direction X/δmax (δmax is the maximum blade thickness). As shown in Figs. 3.7a and 3.7b., results indicate high droplet LWC values at the flow stagnation region (30% of chord length), with more area coverage for sections towards the blade tip.

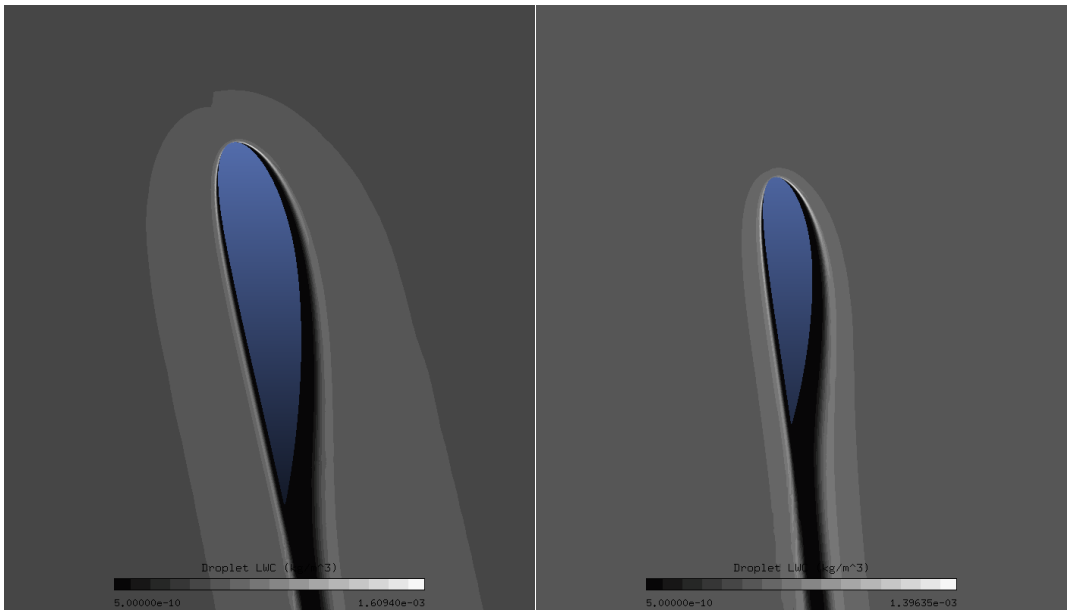

(a) r/R = 0.4 (b) r/R = 0.6

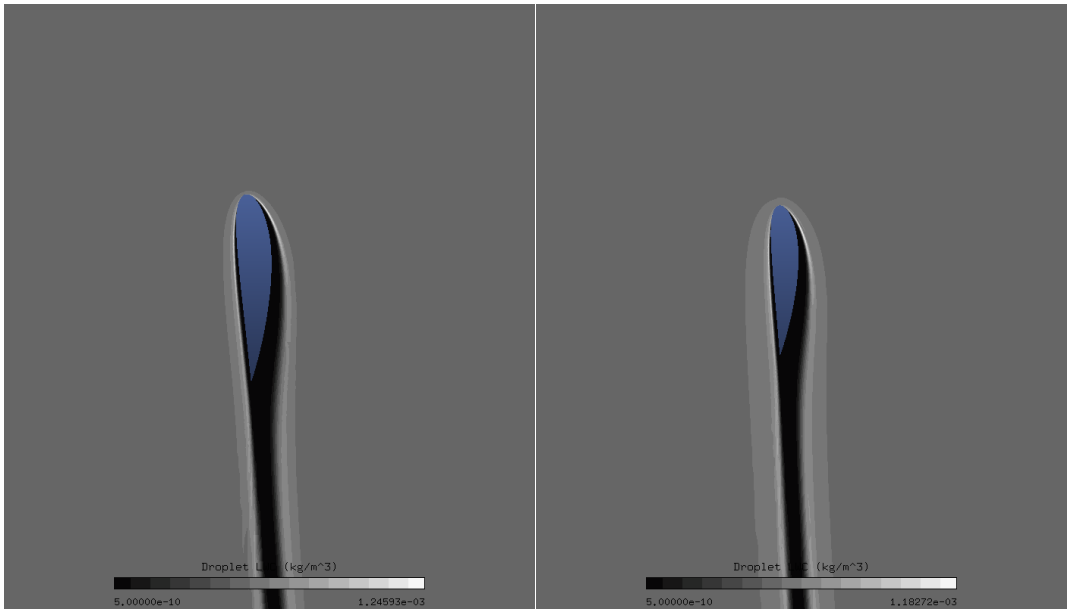

(c) r/R = 0.8 (d) r/R = 1

Figure 3.6. Droplet LWC contours along blade span at different r/R ratios (R = 40 m).

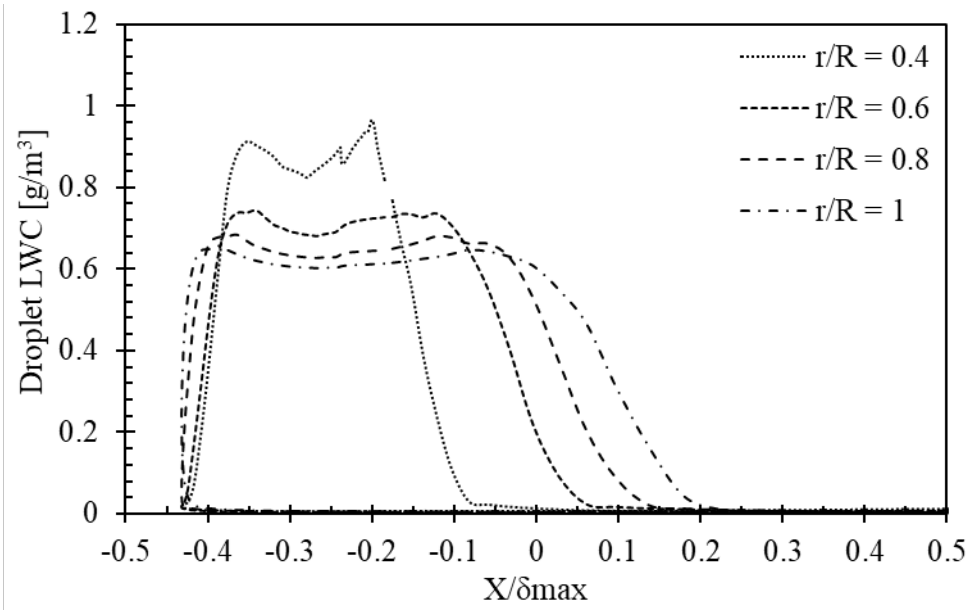

(a)

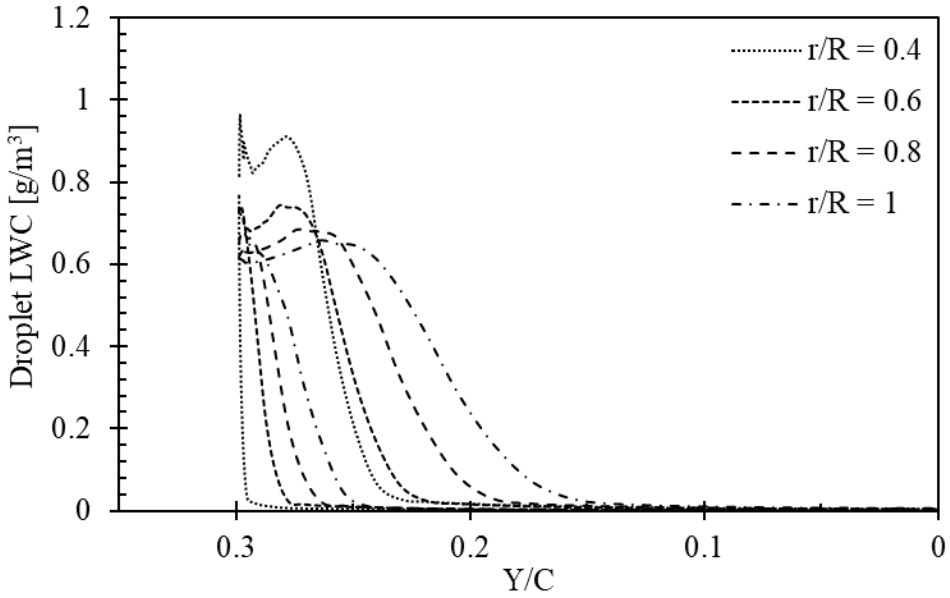

(b)

Figure 3.7. Droplet LWC distribution along blade span at different r/R ratios (R = 40 m) (a) X - direction and (b) Y - direction.

Local droplet collection efficiency over a blade surface depends on the LWC fraction and droplet velocity at a location of interest. Integration of local collection efficiency values over a blade surface impingement area determines the total value for the collection efficiency. Fig. 3.8 shows local droplet collection efficiency values along the four-blade sections in X and Y directions. As shown in Figs. 3.8a and 3.8b, results indicate that more droplet collection and surface acquisition can occur at higher rotational distances towards the blade tip. Results indicate an approximately 2.6 times increase in average collection efficiency value from sections at r/R = 0.4 to sections r/R = 1.

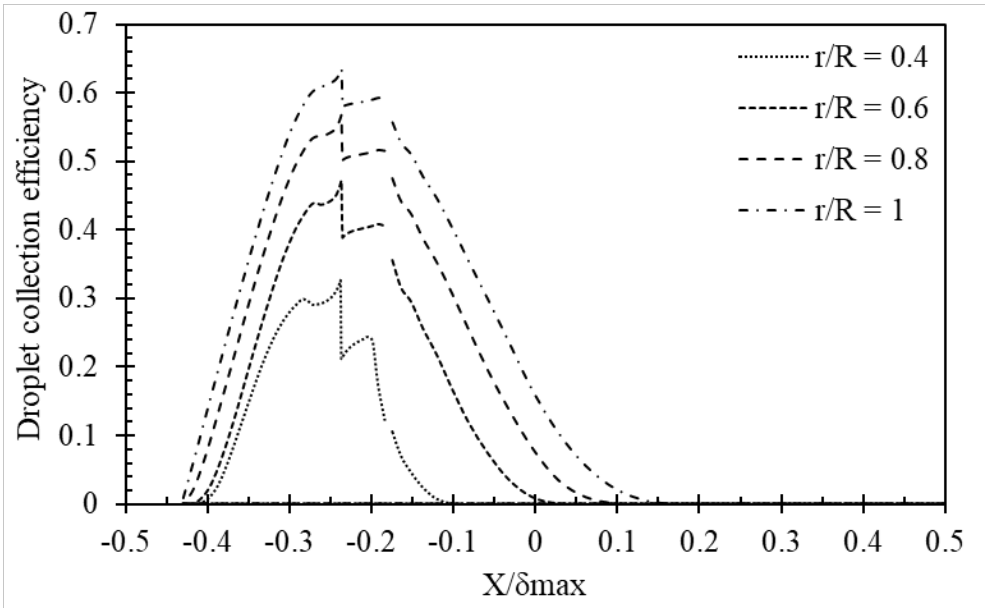

(a)

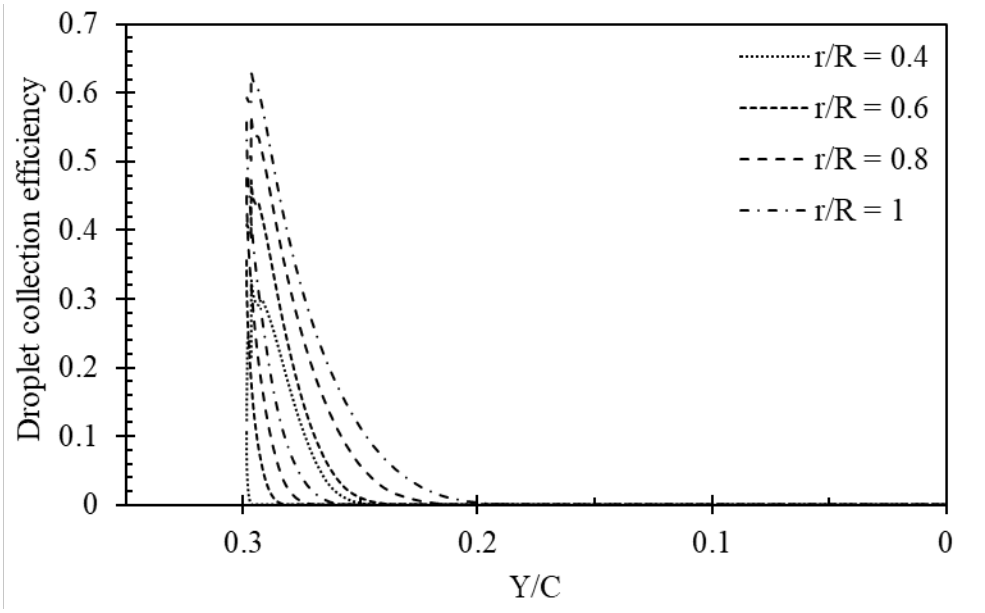

(b)

Figure 3.8. Droplet local collection efficiency distribution along blade span at different r/R ratios (R = 40 m), (a) X - direction and (b) Y - direction.

3.3.4. Ice Distribution and Shape

The ICE3D solver predicts the ice formation caused by impinging droplets as a thin liquid water film on each solid surface. The film may run back when forced by the shear stresses created by the airflow, centrifugal forces, or gravitational forces. The height of the liquid film is predicted at all grid points on the blade surfaces. Based on the surface thermodynamic conditions, part of the water film may freeze, causing ice accretion, evaporation or sublimation. For comparison purposes, the local ice thickness distributions are presented for the different sections along the blade span in Figs. 3.9a and 3.9b. Results show that the maximum ice thickness can occur at the flow stagnation region, characterized by a high water collection efficiency. Results show a lower ice thickness at sections near the base than the tip, suggesting that ice horns are more likely to form on smaller blade sections near the blade tip, as characterized by smaller chord lengths. Results indicate an approximately 3.38 times increase in average ice thickness from sections at r/R = 0.4 to sections r/R = 1.

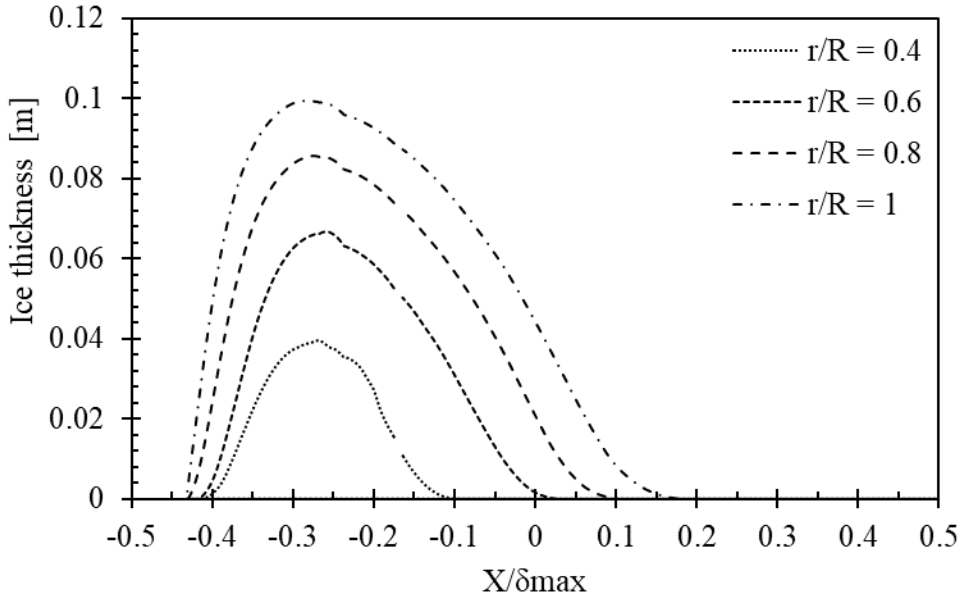

(a)

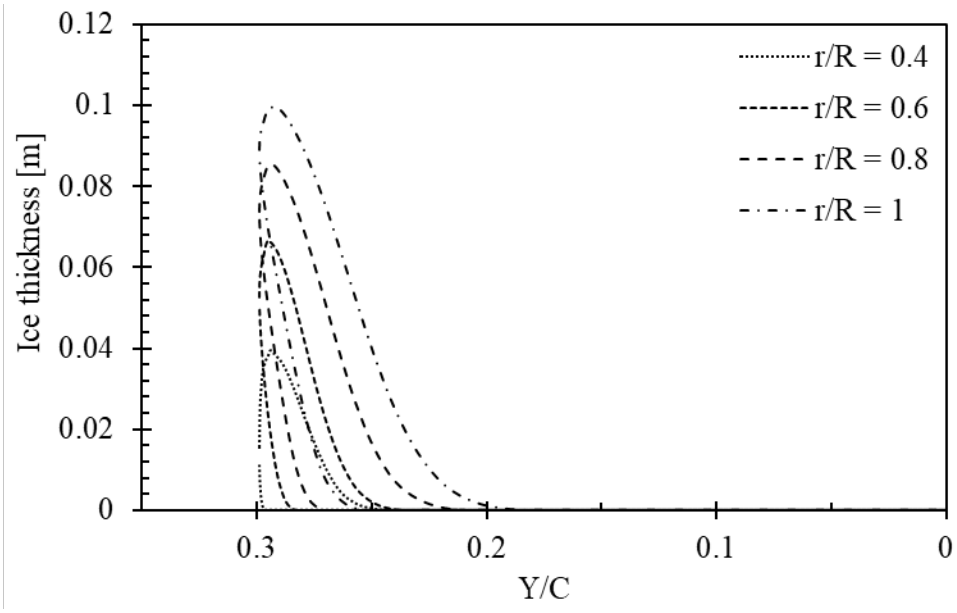

(b)

Figure 3.9. Ice thickness distribution along blade span at different r/R ratios (R = 40 m), (a) X - direction and (b) Y - direction.

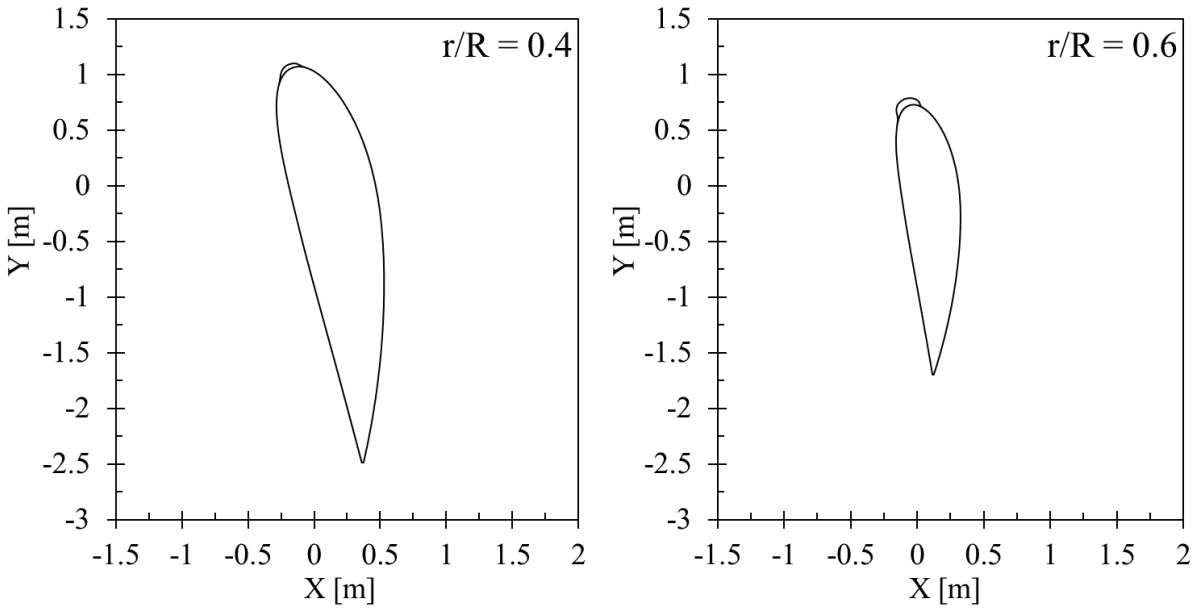

(a) r/R = 0.4

(b) r/R = 0.6

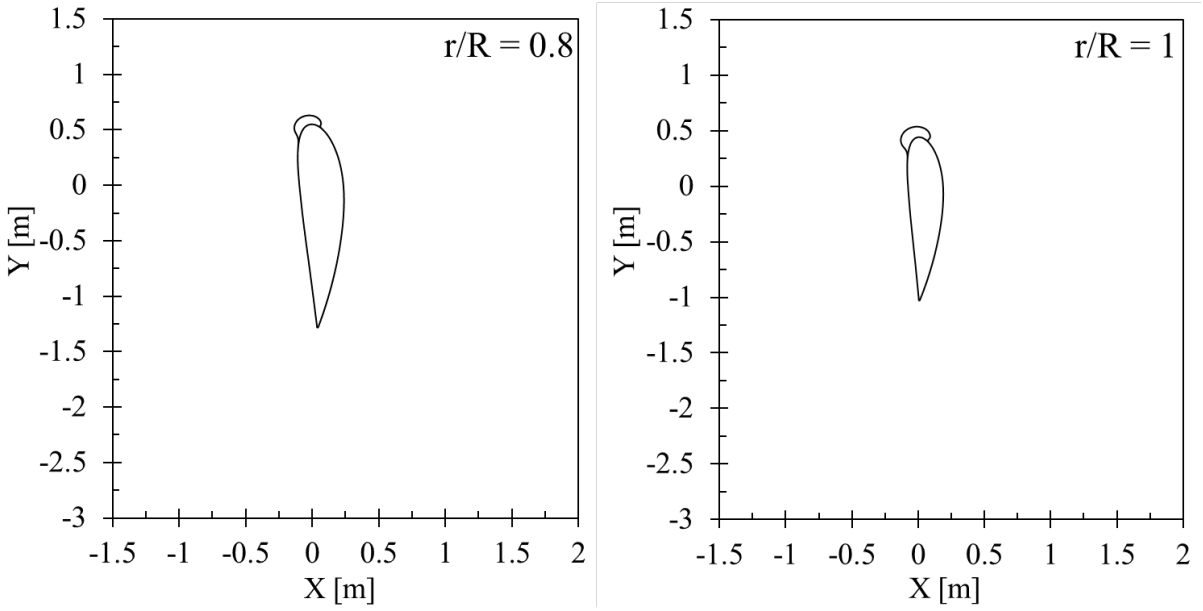

(c) r/R = 0.8 (d) r/R = 1

Figure 3.10. Predicted ice shapes along blade span at different r/R ratios (R = 40 m) (a) X - direction and (b) Y - direction.

3.3.5. Effects of Speed Ratio

The speed ratio is a dimensionless parameter related to the efficiency and wind turbine blade design. Studies recommend an optimal value between 6 and 8 [13]. In this study, the blade model is designed at an optimal TSR value of 7, while ice is investigated at a specific icing condition. Predicted ice loads among different blade span sections are presented. The variation of ice quantity with the sectional speed ratio is shown in Fig. 3.11. Results show higher ice masses accumulate towards the blade tip than the blade root. Ice accretion in terms of mass and shape can be a critical problem for wind turbine blade sections near the tip.

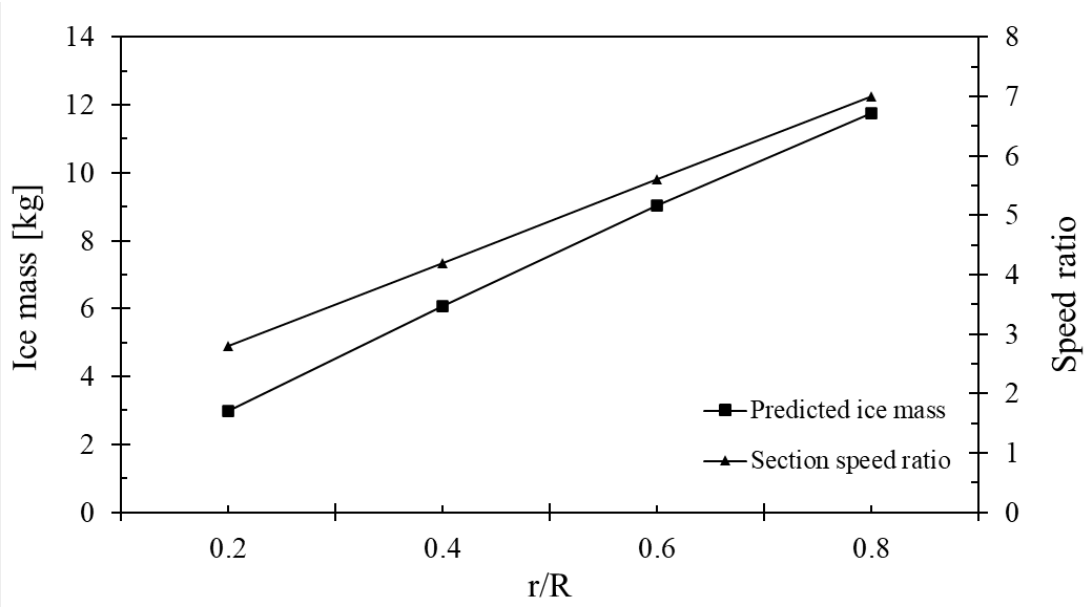

Figure 3.11. Predicted ice mass along blade span at different r/R ratios and sectional speed ratio.

Local ice thickness values are used to predict ice shapes over the geometry. As shown in Fig. 3.11, results indicate comparatively large ice formations at later blade sections towards the blade tip. Results show a 3.95 times increase in ice mass at r/R = 1 when compared to ice at r/R = 0.4. This implies that ice accretion over areas near the blade tip can degrade the aerodynamic performance of a wind turbine blade.

3.4. Conclusions

In this study, ice accretion on a 2 MW power wind turbine blade model was investigated using FENSAP ICE. Four rotating sections on a 40 m radius turbine blade located at 40%, 60%, 80%, 100% of its span were simulated during an icing event. The results indicated high droplet collection efficiencies at the leading edge of each blade section, especially at the flow stagnation point, with an increase of the value towards the blade tip by 2.6 times. Subsequently, larger ice thicknesses were mainly found at the blade's leading edge, with higher accumulations in terms of overall thickness by 3.38 times and mass by 3.95 times towards the tip sections. The results suggest higher

ice loads are expected near the blade tip, contributing to aerodynamic losses in terms of overall lift and drag coefficients. The results provide useful insights for predicting ice accretion along a blade span at different configurations.

References

[1] Jin, J. Y., Virk, M. S., Hu, Q., & Jiang, X. (2020). Study of ice accretion on horizontal axis wind turbine blade using 2D and 3D numerical approach. IEEE Access, 8, 166236-166245.

[2] Reid, T., Baruzzi, G., Ozcer, I., Switchenko, D., & Habashi, W. FENSAP-ICE simulation of icing on wind turbine blades, part 2: ice protection system design. In 51st AIAA Aerospace Sciences Meeting including the New Horizons Forum and Aerospace Exposition (p. 751), Grapevine, Texas, (2013).

[3] Battisti, L. (2015). Wind turbines in cold climates: Icing impacts and mitigation systems. Springer.

[4] Ibrahim, G. M., Pope, K., & Muzychka, Y. S. (2018). Effects of blade design on ice accretion for horizontal axis wind turbines. Journal of Wind Engineering and Industrial Aerodynamics, 173, 39-52.

[5] Han, W., Kim, J., & Kim, B. (2018). Study on correlation between wind turbine performance and ice accretion along a blade tip airfoil using CFD. Journal of Renewable and Sustainable Energy, 10(2), 023306.

[6] Han, Y., Palacios, J., & Schmitz, S. (2012). Scaled ice accretion experiments on a rotating wind turbine blade. Journal of Wind Engineering and Industrial Aerodynamics, 109, 55-67.

[7] Ibrahim, G. M., Pope, K., & Muzychka, Y. S. (2018). Transient atmospheric ice accretion on wind turbine blades. Wind Engineering, 42(6), https://doi.org/10.1177/0309524x18780380

[8] Yirtici, O., Ozgen, S., & Tuncer, I. H. (2019). Predictions of ice formations on wind turbine blades and power production losses due to icing. Wind Energy, 22(7), 945-958.

[9] Virk, M. S., Homola, M. C., & Nicklasson, P. J. (2012). Atmospheric icing on large wind turbine blades. Int. J. Energy Environ, 3(1), 1-8.

[10] ANSYS (2015) FENSAP-ICE User Manual R1.0, Canada.

[11] Naterer, G. F., Advanced Heat Tranfer, 3rd Edition, CRC Press, Boca Raton, FL, 2022.

[12] Lanzafame, R. A., & Messina, M. (2007). Fluid dynamics wind turbine design: Critical analysis, optimization and application of BEM theory. Renewable energy, 32(14), 2291-2305.

[13] Cetin, N. S., Yurdusev, M. A., Ata, R., & Özdamar, A. (2005). Assessment of optimum tip speed ratio of wind turbines. Mathematical and Computational Applications, 10(1), 147-154.

Chapter 4

4. Scaling Formulation of Multiphase Flow and Droplet Trajectories With Rime Ice Accretion on a Rotating Wind Turbine Blade

In this study, scaling and similitude are investigated for ice accretion on a rotating wind turbine blade. Numerical CFD icing simulations are performed using FENSAP ICE software to test the scaling methods and verify the results. A small blade section is scaled six times, and each case is tested at specific flow conditions. Scaled conditions for velocity (streamwise and rotational), droplet size, and icing time are examined. CFD solutions for the flow field (air and droplet) are obtained in terms of the velocity, droplet trajectories, pressure coefficient distributions, ice thickness, and ice shapes, by quantifying the significant parameters involved in the icing process. Recommendations for parameters to be used for rime ice scaling on a rotating blade are presented, and numerical results are reported to support those recommendations.

Numerical results and test conditions are obtained at sea level in wind tunnel facilities for experimental investigation. This study also presents the formulation of non-dimensionlized governing equations for scaling of the flow field, droplet trajectories, and ice accretion on a rotating blade model. It derives a set of non-dimensional groups which govern the flow parameters for a rotating blade, including the Strouhal number, Froude number, drag coefficient of droplets and droplet based Reynolds number, droplet inertia parameter, and two other new parameters. The scaling methodology can also be utilized to determine alternative test conditions to predict rime ice conditions on a rotating blade. The study provides valuable insight to predict ice accretion on large wind turbine blade sections in the field based on scaled smaller blade sections tested in a laboratory setting.

Nomenclature

V	Velocity (m/s)
ρ	Density (kg/m^3)
P	Pressure (Pa)
L_c	Characteristic length (m)
A	Area (m^2)
ϑ	Volume (m^3)
k	Scale factor
t	Time (s)
m	Mass (kg)
$\dot{M}$	Mass flux (kg/m^2)
$\dot{m}$	Mass flow rate (kg/s)
T	Temperature (°C)
Re	Reynolds number
Fr	Froude number
St	Strouhal number
g	Gravitational acceleration (m/s^2)
μ	Dynamic viscosity (Pa·s)
α	Water volume fraction (kg/m^3)
C_d	Droplet drag coefficient
K	Droplet inertia parameter
d	Droplet diameter (m)
A_c	Ice accumulation parameter
C_D	Aerodynamic drag coefficient
C_L	Aerodynamic lift coefficient
δ	Thickness (m)
c	Chord length (m)
β	Total collection efficiency
β_o	Local collection efficiency
$\vec{n}$	Normal surface vector
n	Freezing fraction

Abbreviations

$NREL$	National Renewable Energy Laboratory
IRT	Icing Research Tunnel
LWC	Liquid Water Content
MVD	Median Volume Diameter
BEM	Blade Element Momentum theory
CFD	Computational Fluid Dynamics

Subscripts and Superscripts

a	Air
d	Droplet
R	Relative
r	Distance from the axis of rotation
∞	Stream conditions
o	Initial conditions/local
c	Accumulation
imp	Impingement
ice	Ice
f	Oscillation frequency
f	Full-scale model
s	Scaled model

4.1. Introduction

Northern cold regions have a promising potential for wind power generation. However, atmospheric ice accretion is a challenging problem for wind turbines located in these regions. This can significantly reduce the annual power production of wind farms. Ice accretion on a surface is inherently an unsteady phenomenon [1]. Ice forms on surfaces exposed to atmospheric icing conditions with some liquid water content, freezing temperatures, and areas with high convective cooling rates, such as cold, windy environments or cold climates with frost, snow, and freezing rain [2]. In rime ice conditions, as super-cooled water droplets in the atmosphere collide with the surface of a wind turbine blade, the process of ice formation begins and ice accretion occurs [3]. The cooling effect of the ambient air and the energy released by evaporation significantly impact this process.

For glaze ice accretions, only a fraction of cold water droplets freeze as they collide with an exposed surface where the local temperature is close to freezing. Shear stresses, aerodynamic forces, and gravity affect the remaining water droplets to flow back and freeze downstream [4]. Rime ice accretion typically occurs when the temperature is well below the freezing point [3, 4]. Convective cooling becomes more intense at colder temperatures with freezing of all impinging water droplets upon contact, creating rime ice accretions [4]. Rime ice is usually opaque, granular ice with an accumulated mass concentration along the blade's leading edge [3-7], with lower densities ranging up to 600 kg/m^3 depending on the conditions of soft or hard rime [2]. Rime ice can exist at temperatures ranging from -12 °C to -4 °C and it mainly forms at lower temperatures with less liquid water content and small droplet sizes in the atmosphere [2, 8].

Characteristic features of ice accretion include the size of ice, position, angle, and shape. The degree to which these characteristics are related between lab-scale and actual field conditions has

been examined previously [9- 11]. A scaling method is a procedure to determine the scaled test conditions to produce the same result as exposing the reference model to the desired icing conditions. Due to wind tunnel size limitations, many components of wind turbines cannot be tested in a laboratory at their full size. Furthermore, wind tunnel facilities for icing investigation can only provide limited ranges of air speed, rotational speeds of components, temperatures, droplet sizes, and liquid-water content.

The main objectives of scaling methods are usually to ensure that the flow field, droplet field, and amount of accumulated ice are equivalent relative to the model size. The predicted ice characteristics in terms of shape and distributed thickness, and the aerodynamic processes due to the icing, are the same as would have occurred for the desired test conditions, or reference model size. Thus, geometry, flow field, droplet trajectory and impingement / collection, and heat transfer rates, must be identical for accurate scaling predictions. Previous studies have used similitude analyses to provide equations that can be solved to model the reference conditions and scaled icing conditions. These relationships, however, can often result in contradictory values for one or more of the test conditions. The exact similitude equations usually cannot be implemented rigorously, so simplifications are typically needed to allow them to be used in real-world scaling situations.

Various scaling methods have been derived from the governing equations of heat and fluid flow with various simplifications and assumptions. Previous studies used different ice scaling methods for aircraft icing processes [12]. Scaled prototype models have been tested in icing wind tunnels to study ice characteristics [13]. Previous studies [14] considered three main dimensionless groups that can significantly affect the normalized ice thickness while analyzing the icing scaling problem. These three groups are the Mach, Reynolds, and Weber numbers. A special velocity requirement is needed between scale and reference cases to match each group. Usually similarity of Mach, Reynolds, and Weber numbers simultaneously cannot be achieved. Other past studies [9, 10]

suggested that similarity in a flowfield requires matching of both Reynolds and Mach numbers. These confirmed that both numbers could not be simultaneously matched when the scale model is not at a full size.

Bilanin [15] proposed non-dimensional groups using the Buckingham-Pi theory. Anderson and Bilanin [16] used the Weber number for icing scaling methods and conducted experiments for result verification in the NASA Lewis Icing Research Tunnel (IRT). Langmuir analyzed water droplet trajectories based on a mathematical model and proposed a range of parameters [17]. Anderson and Bragg [18, 19] studied droplet trajectory scaling methods and similarity parameters, including an inertia parameter, Froude number (Fr), and droplet Reynolds number. Ruff [9] analyzed ice scaling equations, conducted experimental investigations, and developed similar scaling laws. This study extends previous scaling methods and introduces new scaling parameters for ice accretion on a rotating wind turbine blade. This scaling approach includes new parameters to scale the flow field, droplet trajectory, and rime ice accretion for a rotating turbine blade.

4.2. Flow Field Formulation and Scaling Parameters

The airflow is characterized by the equations of mass, momentum, and energy conservation. The air continuity and momentum equations for a rotating blade in a relative frame of reference are given by:

$$\frac{\partial \rho_a}{\partial t} + \vec{\nabla} \cdot \left[\rho_a \vec{V}_{R,a}\right] = 0 \tag{1}$$

$$\rho_a \left[\frac{\partial \vec{V}_{R,a}}{\partial t} + \left[\vec{V}_{R,a} \cdot \nabla\right]\vec{V}_{R,a}\right] = \rho_a \vec{g} - \nabla p_a + \mu_a \nabla^2 \vec{V}_{R,a} - \rho_a \vec{\Omega} \times \left[\vec{\Omega} \times \vec{r}\right] - 2\rho_a \left[\vec{\Omega} \times \vec{V}_{R,a}\right] \tag{2}$$

where the last two-term in Equation (2) represent the Coriolis and centrifugal forces. The significant scaling parameters can be obtained by non-dimensionalization of Equation (2). The resulting scaling parameters are defined as follows in Table 4.1.

Table 4.1. Definitions of the scaling parameters

Scaling parameters	Definition
L_c	Characteristic length (m)
V_R	Characteristic relative speed (m/s)
f	Characteristic flow oscillating frequency (1/s)
Ω	Characteristic rotational speed (rad/s)
R	Characteristic distance to the axis of rotation (m)
$P_o - P_\infty$	Reference pressure difference (N/m^2)
g	Gravitational acceleration (m/s^2)

Define the following non-dimensional variables using the scaling parameters in Table 1,

$$t^* = \mathrm{f}t\,, \vec{V}^*_{R,a} = \frac{\vec{V}_{R,a}}{V_{a,\infty}}\,, \vec{\nabla}^* = \vec{\nabla} L_c\,, \vec{g}^* = \frac{\vec{g}}{g}, P^* = \frac{p_a}{P_o - P_\infty}\,, \vec{r}^* = \frac{\vec{r}}{R}\,, \vec{\Omega}^* = \frac{\vec{\Omega}}{\Omega} \tag{3}$$

Rearranging the variables in Equation (3) in terms of the dimensional variables, and inserting into Equation (2) leads to

$$\begin{aligned} &\rho_a \mathrm{f} V_{a,\infty} \frac{\partial \vec{V}^*_{R,a}}{\partial t^*} + \frac{\rho_a {V_{R,a}}^2}{L_c}\left[\vec{\nabla}^* \cdot \vec{V}^*_{R,a}\right]\vec{V}^*_{R,a} = \rho_a g \vec{g}^* - \left[\frac{(P_o - P_\infty)}{L_c}\right]\vec{\nabla}^* P^* + \\ &\left[\frac{\mu_a V_{a,\infty}}{{L_c}^2}\right]{\vec{\nabla}^*}^2 \vec{V}^*_{R,a} - \rho_a \Omega^2 R \vec{\Omega}^* \times \left[\vec{\Omega}^* \times \vec{r}^*\right] - 2\rho_a \Omega V_{a,\infty}\left[\vec{\Omega}^* \times \vec{V}^*_{R,a}\right] \end{aligned} \tag{4}$$

Each additive term in Equation (4) has primary dimensions of $\{\mathrm{M}^1\mathrm{L}^{-2}\mathrm{T}^{-2}\}$. To non-dimensionalize the equation, every term should be multiplied by a constant of $\frac{L_c}{\rho_a {V_{a,\infty}}^2}$ which has primary dimensions of $\{\mathrm{M}^{-1}\mathrm{L}^2\mathrm{T}^2\}$, so that dimensions are canceled. After some rearrangement, the non-dimensional form of Equation (4) becomes:

$$\left[\frac{fL_c}{V_{a,\infty}}\right]\frac{\partial \vec{V}^*_{R,a}}{\partial t^*} + \left[\vec{\nabla}^* \cdot \vec{V}^*_{R,a}\right]\vec{V}^*_{R,a} = \left[\frac{gL_c}{{V_{a,\infty}}^2}\right]\vec{g}^* - \left[\frac{(P_o - P_\infty)}{\rho_a {V_{a,\infty}}^2}\right]\vec{\nabla}^* P^* + \left[\frac{\mu_a}{\rho_a V_{a,\infty} L_c}\right]{\vec{\nabla}^*}^2 \vec{V}^*_{R,a} - \left[\frac{\Omega^2 R L_c}{{V_{a,\infty}}^2}\right]\vec{\Omega}^* \times \left[\vec{\Omega}^* \times \vec{r}^*\right] - \left[\frac{2\Omega L_c}{V_{a,\infty}}\right]\left[\vec{\Omega}^* \times \vec{V}^*_{R,a}\right] \quad (5)$$

Equation (5) can be rewritten in terms of significant dimensionless parameters for the flow field as follows,

$$[St]\frac{\partial \vec{V}^*_{R,a}}{\partial t^*} + \left[\vec{\nabla}^* \cdot \vec{V}^*_{R,a}\right]\vec{V}^*_{R,a} = \left[\frac{1}{Fr^2}\right]\vec{g}^* - [Eu]\vec{\nabla}^* P^* + \left[\frac{1}{Re_a}\right]{\vec{\nabla}^*}^2 \vec{V}^*_{R,a} - \left[\frac{\Omega^2 R L_c}{{V_{a,\infty}}^2}\right]\vec{\Omega}^* \times \left[\vec{\Omega}^* \times \vec{r}^*\right] - \left[\frac{2\Omega L_c}{V_{a,\infty}}\right]\left[\vec{\Omega}^* \times \vec{V}^*_{R,a}\right] \quad (6)$$

where St, Fr, Eu, Re are the Strouhal, Froude, Euler, and stream Reynolds numbers, respectively. The last two terms represent newly-found groups for a rotating frame reference. These dimensionless terms are a function of the air relative velocity for a rotating blade in the relative frame of reference. In this study, these dimensionless groups, including the stream Reynolds number and the newly found groups in Equation (6), are used to scale the flow field around a rotating blade section.

The droplet motion is predicted by solving the partial differential equations for the conservation of mass and momentum. These equations are modified for rotating blades to include the rotational body forces acting on a droplet. The droplet continuity and momentum equations for a rotating blade in the relative frame of reference are expressed as:

$$\frac{\partial \alpha}{\partial t} + \vec{\nabla} \cdot \left[\alpha \vec{V}_{R,d}\right] = 0 \quad (7)$$

$$\alpha \rho_d \vartheta_d \left[\frac{\partial \vec{V}_{R,d}}{\partial t} + \left[\vec{V}_{R,d} \cdot \nabla\right]\vec{V}_{R,d}\right] = \alpha[\rho_d - \rho_a]\vartheta_d \vec{g} + \alpha \vec{D} - \alpha \rho_d \vartheta_d \vec{\Omega} \times \left[\vec{\Omega} \times \vec{r}\right] - 2\alpha \rho_d \vartheta_d \left[\vec{\Omega} \times \vec{V}_{R,d}\right] \quad (8)$$

where α is the water volume fraction and ϑ_d is the droplet volume (droplet shape is assumed spherical). The drag force over a droplet particle moving in the relative flow stream is expressed as:

$$\vec{D} = \frac{1}{2}\rho_a C_d A_d \left|\vec{V}_a - \vec{V}_d\right|^2 \tag{9}$$

Where $\vec{V}_{a,\infty}$ represents the air stream velocity tangent to the trajectory line of the droplet particle and C_d is the droplet drag coefficient. The droplet Reynolds number is defined as:

$$Re_d = \frac{\rho_a d\left|\vec{V}_a - \vec{V}_d\right|}{\mu_a} \tag{10}$$

Substituting the air density from Equation (10) into Equation (9), the drag force becomes:

$$\vec{D} = \frac{1}{8} Re_d \mu_a \pi d C_d \left|\vec{V}_a - \vec{V}_d\right| \tag{11}$$

By inserting the drag force, substituting with the spherical droplet volume, and rearranging, Equation (9) becomes:

$$\frac{\partial \vec{V}_{R,d}}{\partial t} + \left[\vec{V}_{R,d} \cdot \nabla\right]\vec{V}_{R,d} = \left[1 - \frac{\rho_a}{\rho_d}\right]\vec{g} + \left[\frac{3}{4}\frac{C_d Re_d \mu_a}{\rho_d d^2}\right]\left|\vec{V}_a - \vec{V}_d\right| - \vec{\Omega} \times \left[\vec{\Omega} \times \vec{r}\right] - 2\left[\vec{\Omega} \times \vec{V}_{R,d}\right] \tag{12}$$

For droplet trajectory scaling, the significant scaling parameters can be obtained by non-dimensionalization of Equation (12). Similarly, using Equations (3) and considering scaling variables for the droplet flow,

$$\vec{V}^*_{R,d} = \frac{\vec{V}_{R,d}}{V_{a,\infty}} \quad or \quad \vec{V}_{R,d} = V_{a,\infty}\vec{V}^*_{R,d} \tag{13}$$

By substituting and rearranging, the droplet trajectory momentum equation in a non-dimensional form becomes:

$$\mathrm{f}V_{a,\infty}\frac{\partial \vec{V}^*_{R,d}}{\partial t^*} + \frac{{V_{a,\infty}}^2}{L_c}\left[\vec{V}^*_{R,d} \cdot \vec{\nabla}^*\right]\vec{V}^*_{R,d} = \left[1 - \frac{\rho_a}{\rho_d}\right] g\vec{g}^* + \left[\frac{3}{4}\frac{C_d Re_d \mu_a V_{a,\infty}}{\rho_d d^2}\right]\left|\vec{V}^*_a - \vec{V}^*_d\right| - \Omega^2 R\vec{\Omega}^* \times \left[\vec{\Omega}^* \times \vec{r}^*\right] - 2\Omega V_{a,\infty}\left[\vec{\Omega}^* \times \vec{V}^*_{R,d}\right] \tag{14}$$

Therefore, by multiplying every term by a constant of $\frac{L_c}{{V_{a,\infty}}^2}$, the non-dimensional form of the droplet momentum equation becomes:

$$[St]\frac{\partial \vec{V}^*_{R,d}}{\partial t^*} + \left[\vec{V}^*_{R,d} \cdot \vec{\nabla}^*\right]\vec{V}^*_{R,d} = \left[1 - \frac{\rho_a}{\rho_d}\right]\left[\frac{1}{Fr^2}\right]\vec{g}^* + \left[\frac{3}{4}\frac{C_d Re_d \mu_a L_c}{\rho_d d^2 V_{a,\infty}}\right]\left|\vec{V}^*_a - \vec{V}^*_d\right| - \left[\frac{\Omega^2 R L_c}{{V_{a,\infty}}^2}\right]\vec{\Omega}^* \times \left[\vec{\Omega}^* \times \vec{r}^*\right] - \left[\frac{2\Omega L_c}{V_{a,\infty}}\right]\left[\vec{\Omega}^* \times \vec{V}^*_{R,d}\right] \quad (15)$$

Using the dimensionless droplet inertia parameter K as defined in past literature [8-17],

$$K = \frac{\rho_d d^2 V_{a,\infty}}{18\mu_a L_c} \quad (16)$$

where d is the droplet size. Substituting the inertia parameter into the droplet momentum equation leads to its final form as:

$$[St]\frac{\partial \vec{V}^*_{R,d}}{\partial t^*} + \left[\vec{V}^*_{R,d} \cdot \vec{\nabla}^*\right]\vec{V}^*_{R,d} = \left[1 - \frac{\rho_a}{\rho_d}\right]\left[\frac{1}{Fr^2}\right]\vec{g}^* + \left[\frac{C_d Re_d}{24K}\right]\left[\vec{V}^*_a - \vec{V}^*_d\right] - \left[\frac{\Omega^2 R L_c}{{V_{a,\infty}}^2}\right]\vec{\Omega}^* \times \left[\vec{\Omega}^* \times \vec{r}^*\right] - \left[\frac{2\Omega L_c}{V_{a,\infty}}\right]\left[\vec{\Omega}^* \times \vec{V}^*_{R,d}\right] \quad (17)$$

where St, Fr, C_d, Re_d and K are the Strouhal number, Froude number, drag coefficient over the droplet and droplet based Reynolds number, and droplet inertia parameter, respectively. The last two terms represent newly-found groups for the rotating reference frame. These dimensionless terms are functions of the droplet velocity and air stream velocity for a rotating blade in the relative frame of reference.

In this study, the dimensionless groups, including droplet Reynolds number, droplet inertia parameter, and droplet drag coefficient in Equation (17), are used to scale the droplet trajectories around a rotating blade section. Potential empirical correlations [20, 21] are used to obtain the drag coefficient for the droplet as a function of the Reynolds number for specified ranges. If the Stokes Law is applied for a flow around an isolated sphere with a minimal Reynolds number, $Re_d > 1$, the droplet drag coefficient is obtained by:

$$C_d = \frac{24}{Re_d} \tag{18}$$

For extended values of Re_d around spherical droplets, the droplet drag coefficient is obtained [20, 21] by:

$$C_d = \left(\frac{24}{Re_d}\right)\left(1 + 0.1935{Re_d}^{0.6305}\right) \text{ for } 20 \leq Re_d \leq 260$$

$$C_d = \left(\frac{24}{Re_d}\right)\left(1 + 0.15{Re_d}^{0.687}\right) \text{ for } Re_d \leq 1300 \tag{19}$$

$$C_d = 0.4 \text{ for } Re_d > 1300$$

The local and total collection efficiency can be defined in vector form [22] as:

$$\beta_o = -\frac{\alpha \vec{V}_d \cdot \vec{n}}{LWC_\infty V_{a,\infty}} \tag{20}$$

$$\beta = \frac{\int \beta_o dA}{A_{imp}} \tag{21}$$

where α is the local water volume fraction, $\vec{n}$ is the normal surface vector, LWC_∞ is the stream liquid water content and A_{imp} is the total impingement area. This area can be calculated by multiplying the object surface perimeter by the span-wise length.

A control volume can be selected along the stagnation line and extended from the boundary layer to the body's surface to analyze the mass conservation and energy transfer during an icing event. It encloses a distance along the external surface and extends in the span-wise direction. This scaling analysis assumes no conduction heat transfer, no radiative heat transfer, and the energy transfer terms are only used for impingement of super-cooled water droplets, evaporation/sublimation, convection, and ice accretion. Heat and mass transfer phenomena are obtained by solving for the ice accretion and runback. The processes caused by impinging droplets

can be modeled as a thin liquid film on each blade surface. The film may runback, forced by the shear stresses created by the airflow, centrifugal forces, or gravity.

Assuming there will be no water inflow along the surface because a stagnation-point control volume has been selected, the mass balance along the blade stagnation line control volume requires that:

$$\sum \dot{M}_{in} = \sum \dot{M}_{out} \tag{22}$$

$$\dot{M}_{imp} = \dot{M}_{runback} + \dot{M}_{evap/sub} + \dot{M}_{ice} \tag{23}$$

The mass flux balance for the runback water film before freezing on the surface [22] can be expressed as:

$$\rho_f \left[\frac{\partial h_f}{\partial t} + \vec{\nabla} \cdot \left[h_f \bar{V}_f \right] \right] = \dot{M}_{imp} - \dot{M}_{evap/sub} - \dot{M}_{ice} \tag{24}$$

where $\vec{h}_f$ is the fluid (i.e., water) film height and $\bar{V}_f$ is the average film velocity before freezing (as it runs back along the blade surface). The three terms on the right-hand side correspond to the total mass transfer by water droplet impingement (i.e., source for the fluid film), evaporation/sublimation, and ice accretion (i.e., freezing of the liquid film). The freezing fraction is defined as:

$$n = \frac{\dot{M}_{ice}}{\dot{M}_{imp}} \tag{25}$$

At very low temperatures, rime ice can exist. Water droplets impinging on the blade surface freeze upon impact and thus contribute directly to ice formation (i.e., $n = 1$). No water runs back along the blade surface as all total mass freezes upon impact. Also no evaporation / sublimation occurs (i.e., total impingement water mass is converted to ice). The mass flux rate of the total impingement water on a rotating blade can be calculated as:

$$\dot{M}_{imp} = V_{a,\infty} LWC_{\infty} \frac{\int \beta_o dA}{A_{imp}} \tag{26}$$

The total impingement water mass rate is calculated as:

$$\dot{m}_{imp} = V_{a,\infty} LWC_{\infty} A_{imp} \beta \tag{27}$$

The total mass of impinging water is:

$$m_{imp} = V_{a,\infty} LWC_{\infty} A_{imp} \beta t_{ice} \tag{28}$$

where t_{ice} is the total icing event time. The total mass flow rate of rime ice is equal to the mass of impingement water,

$$m_{ice} = V_{a,\infty} LWC_{\infty} A_{imp} \beta t_{ice} \tag{29}$$

4.3. Rime Ice Scaling and Identification of Scaling Parameters

For scaling of ice accretion and achieving similarity, the scaling methodology needs to simulate the blade geometry, mixed flow field, droplet trajectories, and the mass and heat transfer rates associated with the blade surface phenomena of the icing process. During rime ice accretion, all droplets impinging on the blade surface freeze upon impact. The equations for scaling of the flow field, droplet trajectories and total water collection are sufficient to predict this ice type successfully. During glaze ice, a fraction of the total water collected by the blade surface freezes. The energy balance is analyzed along with the mass balance on the icing surface. The rate of water that freezes on the blade surface during glaze ice depends on the local heat balance. Additionally, convective and evaporative mass fluxes and energy terms should be considered for glaze ice accretion.

4.3.1. Geometric Similarity Requirements

Blade geometry scaling requires geometric scaling conditions to be met between both models. The scaled blade geometry (including the airfoil curvature) should be identical to the reference blade geometry and other geometrical parameters, such as the blade surface roughness, material, and tilt/twist angle. Scaling should ensure similarity in the chord length (X), airfoil curvature thickness (Y), and span-wise length (Z). The scale factor k is defined as:

$$k = \frac{L_{c_f}}{L_{c_s}} \qquad \left[i.e., k = \frac{X_f}{X_s} = \frac{Y_f}{Y_s} = \frac{Z_f}{Z_s}\right] \tag{30}$$

The scale factor represents the ratio between the characteristic lengths L_c of both full-size and scaled-down geometries.

4.3.2. Flow Field Scaling Requirements

The dimensionless analysis for the airflow field modeling for a rotating blade suggests maintaining the significant parameters, including the relative flow Reynolds number and the two terms representing performance speed ratios. Thus, similarity can be achieved in the airflow field between the reference (full size) and scaled models (smaller size). Holding one dimensionless group from Eq. (6) constant between subscale and full-scale models is sufficient for scaling one variable. When the Strouhal, Froude, Euler, or stream Reynolds number scale with the stream velocity, the last two parameters in Eq. (6) will scale the rotational velocity based on the scale factor.

The air-stream flow Reynolds number is given by:

$$\left[Re_{a,\infty}\right]_s = \left[Re_{a,\infty}\right]_f \tag{31}$$

$$\left[\frac{\rho_a V_{a,\infty} L_c}{\mu_a}\right]_s = \left[\frac{\rho_a V_{a,\infty} L_c}{\mu_a}\right]_f$$

The newly found non-dimensional groups that represent performance speed ratios are obtained as:

$$\left[\frac{\Omega^2 R L_c}{{V_{a,\infty}}^2}\right]_s = \left[\frac{\Omega^2 R L_c}{{V_{a,\infty}}^2}\right]_f \tag{32}$$

$$\left[\frac{2\Omega L_c}{V_{a,\infty}}\right]_s = \left[\frac{2\Omega L_c}{V_{a,\infty}}\right]_f \tag{33}$$

These scaling Equations (31), (32), and (33) can be used to scale the operating parameters such as wind speed, rotational speed, and rotational radius (i.e., distance to the axis of rotation) based on the scale factor k. Solving the equations and neglecting compressibility effects, the flow stream velocity scales as:

$$\left[V_{a,\infty}\right]_s = k\left[V_{a,\infty}\right]_f \tag{34}$$

The rotational radius scales as:

$$[R]_s = \frac{[R]_f}{k} \tag{35}$$

The rotational speed of the blade scales as:

$$[\Omega]_s = k^2[\Omega]_f \tag{36}$$

4.3.3. Droplet Trajectories and Impingement Scaling Requirements

The droplet trajectory scaling requires that the total mass of the water that reaches each part of the blade surface must be similar. The trajectory analysis for the droplet momentum equation presents the significant dimensionless parameters to consider. Maintaining these scaling parameters can sufficiently satisfy the requirements for producing similar droplet trajectories

between the scaled and reference models. In this study, a significant dimensionless group that is considered is:

$$\left[\frac{C_d Re_d}{24K}\right]_s = \left[\frac{C_d Re_d}{24K}\right]_f \tag{37}$$

Equation (37) can be used to scale the droplet flow conditions (including the droplet size) based on the scale factor k. Each dimensionless parameter in the group relies on the characteristic length, directly or indirectly.

Maintaining one parameter from the group such as the inertia parameter retains the others (i.e., drag and Reynolds). Solving the equations and neglecting the compressibility effects, the droplet diameter scaling can be done either by the Reynolds number as:

$$[Re_d]_s = [Re_d]_f$$

$$\left[\frac{\rho_a d\left|\vec{V}_a - \vec{V}_d\right|}{\mu_a}\right]_s = \left[\frac{\rho_a d\left|\vec{V}_a - \vec{V}_d\right|}{\mu_a}\right]_f \tag{38}$$

$$[d]_s = \frac{[d]_f}{k}$$

or by using the droplet inertia parameter as:

$$[K]_s = [K]_f$$

$$\left[\frac{\rho_d d^2 V_{a,\infty}}{\mu_a L_c}\right]_s = \left[\frac{\rho_d d^2 V_{a,\infty}}{\mu_a L_c}\right]_f \tag{39}$$

$$[d]_s = \frac{[d]_f}{k}$$

As mentioned previously, the scaling of the droplet size will ensure an equal drag coefficient over the droplet since it mainly depends on the Reynolds number.

4.3.4. Ice Scaling Requirements

The amount of ice that accumulates on the blade surface depends on the amount of water in the atmosphere (i.e., LWC) and the amount of water that reaches and freezes on the blade surface. The concept of the freezing fraction, n, can be possible for two cases - one is when there is no local freezing of water, n = 0, and another when all the water that reaches the surface of the model freezes upon impact, n = 1 (i.e., rime ice). Thus, the freezing fraction is another similarity parameter that should be considered for ice scaling [10, 13, 23]. The freezing fraction represents the rate of ice growth with time and can be expressed as:

$$\frac{d\delta_{ice}}{dt_{ice}} = \frac{n\dot{M}_{imp}}{\rho_{ice}} \tag{40}$$

where δ_{ice} is the local ice thickness, ρ_{ice} is the local ice density, and t_{ice} is the icing time. Although the local collection efficiency β_o is expected to vary with time as the ice shape changes slightly, if both β_o and δ_{ice} are assumed to be constant while icing process, Equation (40) can be integrated for the icing time to obtain the local ice thickness δ_{ice} as follows,

$$\delta_{ice} = \frac{nV_{a,\infty}LWC_{\infty}\beta_o t_{ice}}{\rho_{ice}} \tag{41}$$

One approach to scale ice shape is that the local thickness of ice normalized by the characteristic model dimension must be similar between the scaled models and reference model,

$$\left[\frac{\delta_{ice}}{L_c}\right]_s = \left[\frac{\delta_{ice}}{L_c}\right]_f \tag{42}$$

Modifying Equation (41) to include total collection efficiency leads to introduce a scaling parameter called the ice accumulation parameter A_c, defined as:

$$A_c = \frac{nV_{a,\infty}LWC_{\infty}\beta t_{ice}}{\rho_{ice}L_c} \tag{43}$$

Therefore, to ensure successful scaling of the local ice thicknesses everywhere on the blade surface, the ice accumulation parameters must be maintained between the scaled and the reference models.

$$[A_c]_s = [A_c]_f$$
$$\left[\frac{V_{a,\infty} LWC_\infty \beta t_{ice}}{\rho_{ice} L_c}\right]_s = \left[\frac{V_{a,\infty} LWC_\infty \beta t_{ice}}{\rho_{ice} L_c}\right]_f \quad (44)$$

Equation (44) can be used to scale icing conditions (i.e., such as LWC or icing time) using the scale factor k. In this analysis, it is assumed that there is no significant change in total collection efficiency. Thus, it is canceled from Equation (44), and the stream LWCs are maintained. Therefore, the icing times scales as:

$$[t_{ice}]_s = \frac{[t_{ice}]_f}{k^2} \quad (45)$$

4.4. Scaling Methodology

4.4.1. Scaled Blade Models

In this section, flow field scaling is investigated for similar rotating blade sections with scaled sizes located at different scaled radii. This will provide useful insights for scaling predictions for wind turbine rime icing. The selected geometry is a section of a turbine blade. The blade section geometry scaling is achieved in all three spatial dimensions using the scale factor k. A non-symmetrical airfoil (NERL S809) is selected for this study. The flow conditions on each model are obtained based on a similitude analysis and scaling equations previously mentioned. As shown in Fig. 4.1, six similar blade sections are numerically investigated at scaled distances to the axis of rotation. The rotational direction is a counterclockwise direction for all rotating blades. Each blade

origin point is set at 0.3 of the chord length to approximate the center of gravity; hence, the total chord length of the blade can be described along the x-axis as -0.3 to 0.7.

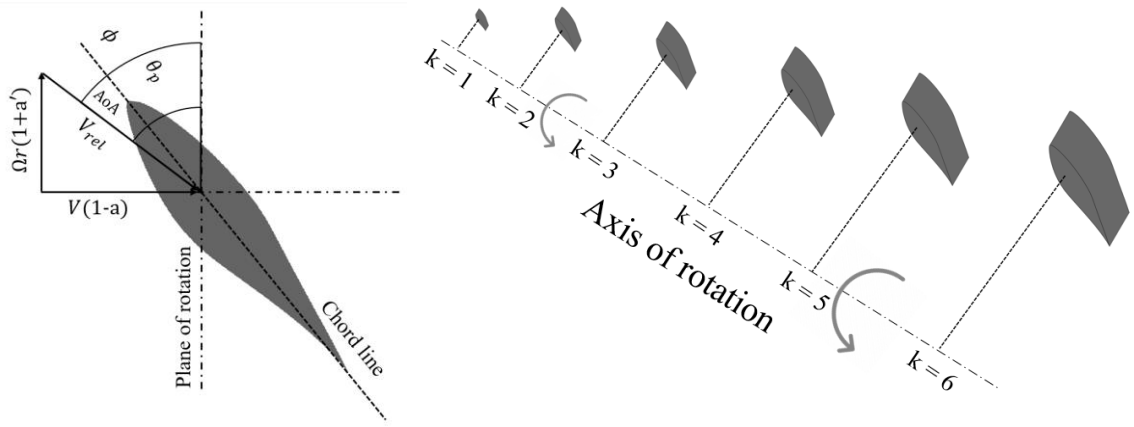

Figure 4.1. Discretization of the rotating scaled blade sections and aerodynamic orientation.

For optimal blade rotation, the Blade Element Momentum (BEM) theory is applied to obtain the optimal pitch angle of the blade section, $\tan\phi = \left[\frac{2}{3\lambda}\right]$ (i.e., at an optimum axial induction factor, a = 1/3) based on the tip speed ratio and the designated airfoil optimal angle of attack, (i.e., at C_L/C_D = maximum) for the selected Reynolds number (i.e., 5×10^5) [24]. A unity scale (i.e., k = 1) factor represents the smallest blade size, and the blade is scaled up to six times as large (i.e., k = 6). Values for each model dimension and each section area are shown in Table 4.2. Applying Eq. (30), the scale factor value reflects what is shown in Table 4.2.

Table 4.2. Scaled blade geometry characteristics

Parameter	**Scale factor k**					
	1	2	3	4	5	6
Chord length (m)	0.15	0.3	0.45	0.6	0.75	0.9
Span wise length (m)	0.05	0.1	0.15	0.2	0.25	0.3
Section reference area (m^2) (i.e., Chord by span)	0.0075	0.03	0.0675	0.12	0.1875	0.27
Area impingement (m^2) (i.e., Perimeter by span)	0.0155	0.062	0.1396	0.2481	0.3877	0.5584

4.4.2. Computational Mesh and Discretization

This numerical study investigates rime ice scaling using ANSYS FENSAP ICE. A CFD mesh is created for each blade model to compute the flow field solution and predict ice accretion characteristics. Each CFD mesh boundary conditions include a wall (i.e., blade section surface), inlet, outlet, and symmetrical topology. Each computational grid is constructed of high-resolution hexahedral elements, ranging in approximately 360 to 630 thousand elements. High-resolution hexahedral mesh elements with a growth rate of 1.15 are created for each blade model surface (see Fig. 4.2). A corresponding y-value of 1 with a first layer below 10^{-4} is computed based on the flow conditions to ensure that the CFD domain around each blade surface is appropriately sized for an accurate simulation. A one-equation Spalart Allmaras turbulence model is used for modeling of the turbulent flow around the blade sections [25]. Successful convergence is achieved for air and droplet flow field solution residuals.

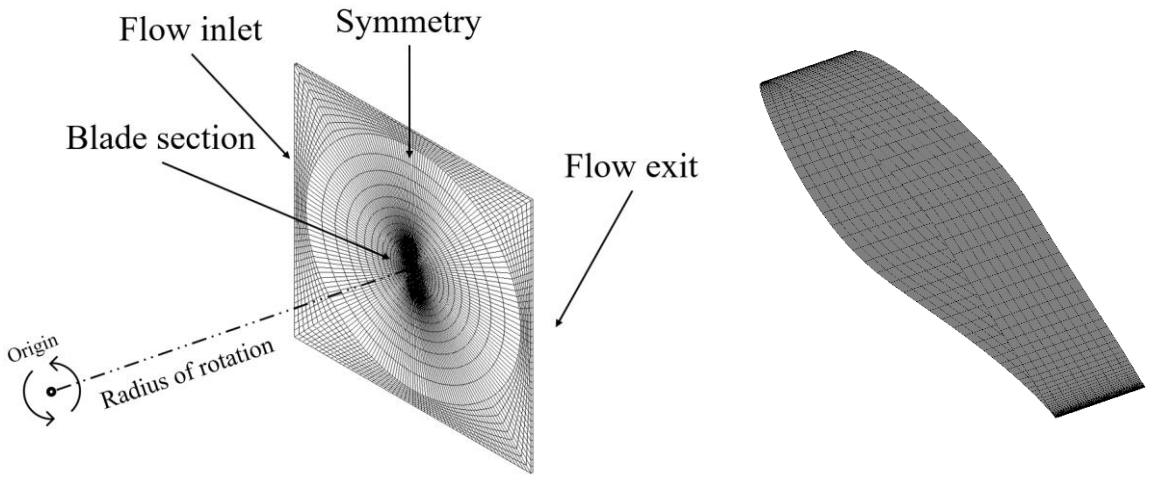

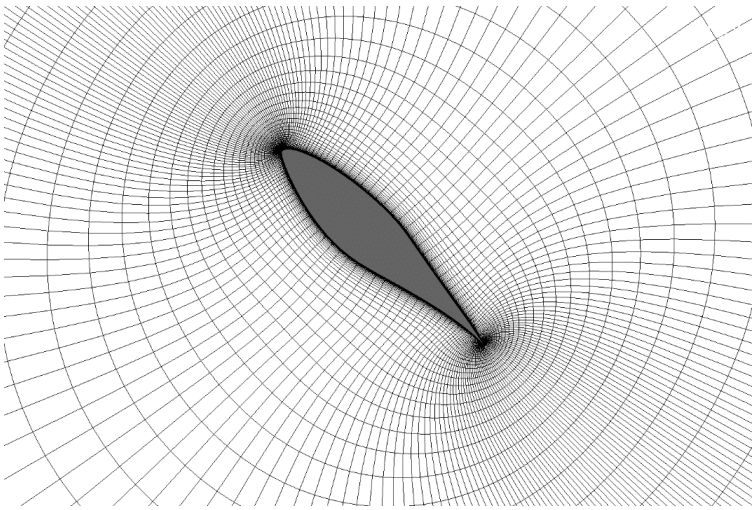

Figure 4.2. Discretization of the CFD grid boundary conditions for the blade surface.

4.4.3. Numerical Test Conditions

The flow field solution, droplet solution, and ice accretion characteristics are obtained to analyze the scaling effects. In this study, several parameters are maintained constant during the tests, including atmospheric pressure, temperature and blade surface roughness, LWC, tip speed ratio, and Reynolds number. The angle of attack is maintained constant during the tests at 7 degrees. Other parameters are scaled using the similarity relations based on the scale factor, k including blade section dimensions, flow stream velocity, rotational speed, rotational radius, droplet size, and icing time. Flow, droplet, and ice accretion parameters are investigated at a temperature of -10 °C. The droplet distribution in the mixed flow is modeled as monodisperse droplet formation at a selected droplet size, which is available in the droplet solver. The liquid water content in the flow stream is specified at 0.3 g/m^3 as lower LWC_∞ values characterize rime ice conditions. The test conditions are summarized in Table 4.3.

Table 4.3. Test conditions for the scaling method

Parameter	Test conditions	Scale factor k					
		1	2	3	4	5	6
Flow stream temperature (°C)	Maintained	-10	-10	-10	-10	-10	-10
Angle of attack (deg.)	Maintained	7					
Stream velocity (m/s)	Scaled	41.5	20.75	13.83	10.37	8.3	6.9
Rotational velocity (rpm)	Scaled	198	49.5	22	12.375	7.92	5.5
Rotational radius (m)	Scaled	1	2	3	4	5	6
LWC_{∞} (g/m^3)	Maintained	0.3	0.3	0.3	0.3	0.3	0.3
MVD (µm)	Scaled	8	16	24	32	40	48
Icing time (hrs)	Scaled	0.25	1	2.25	4	6.25	9

4.5. Results and Discussion

Air velocity contours are presented in Fig. 4.3. The air velocity magnitudes corresponding to each model scale factor are shown below each contour. The results indicate close similarity in the air velocity contours for varied blade section sizes at uniform flow field dimensionless groups (i.e., flow stream Reynolds number and two performance speed ratio terms). Higher air velocity magnitudes can be found over small-sized scaled sections compared to the large sections.

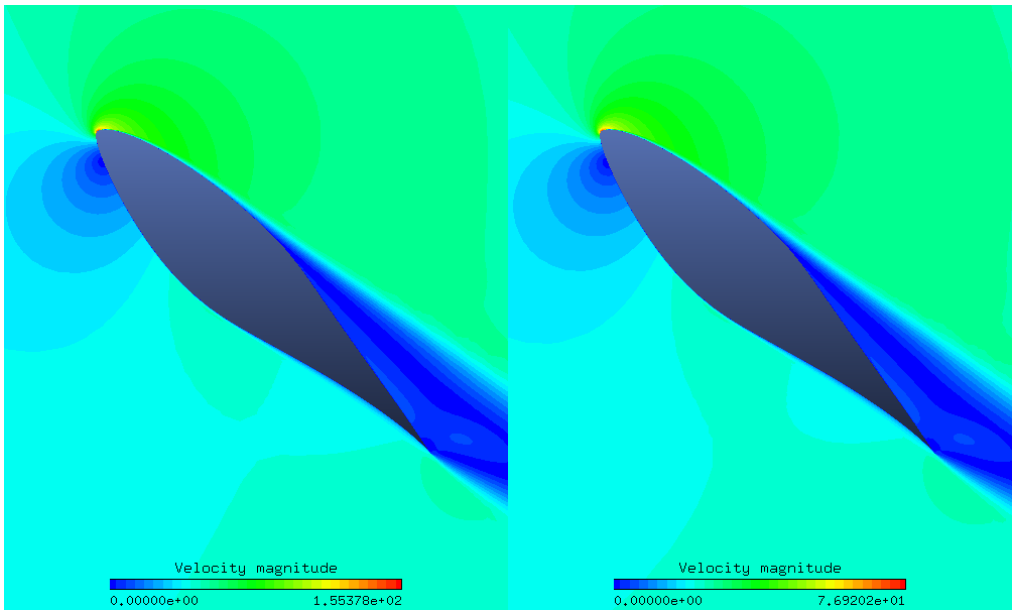

(a) k = 1 (b) k = 2

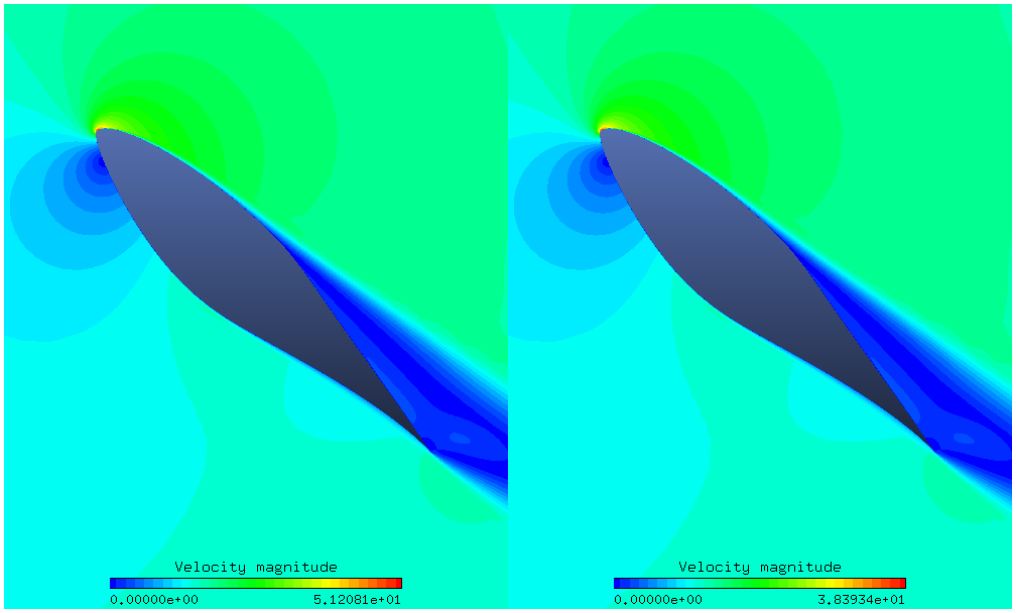

(c) k = 3 (d) k = 4

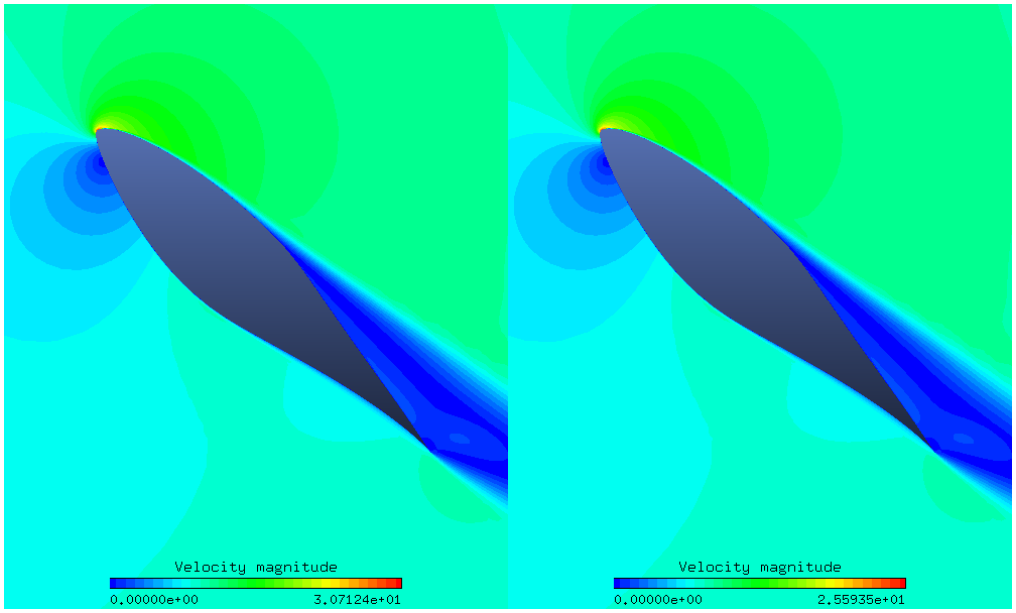

(e) k = 5 (f) k = 6

Figure 4.3. Air velocity contours for different model scale factors.

As illustrated in Fig. 4.4, pressure distributions along similar blades are compared. Each blade origin point along the x-axis (i.e., x = 0) is set at 0.3 of the chord length to approximate the center of gravity; hence, the total chord length of the blade can be described along the x-axis as -0.3 to

0.7. The pressure coefficient profile mainly depends on the flow angle of attack. Results show a similar pressure distribution for all blade sizes at scaled flow conditions.

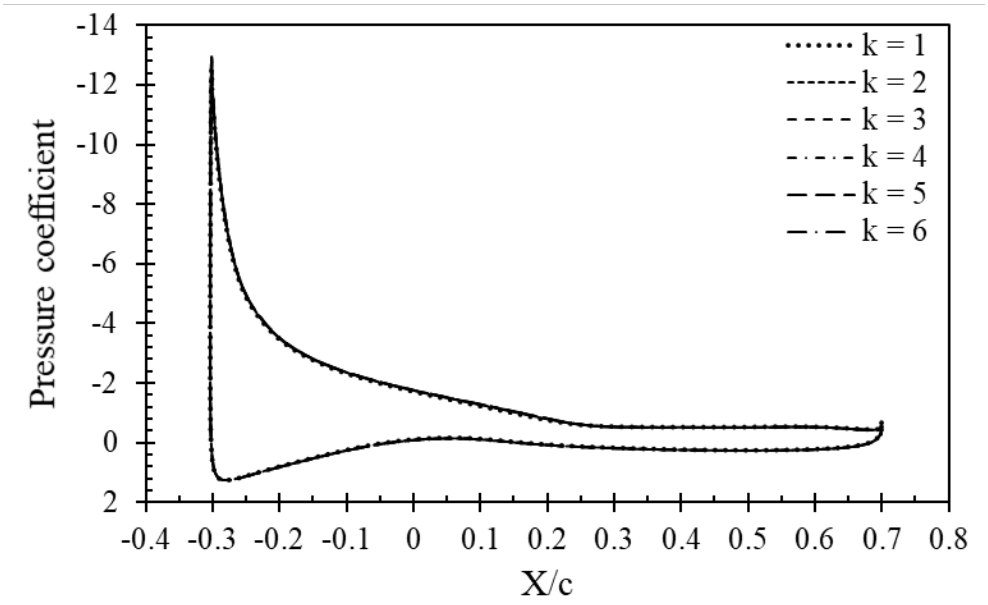

Figure 4.4. Pressure coefficient for different model scale factors.

The droplet solution is obtained numerically using a DROP 3D solver. Velocity magnitudes of the droplets injected in the domain for each blade surface are computed. Droplet velocity contours are presented in Fig. 4.5. Droplet velocity magnitudes are shown under each contour. Results indicate close similarity in the droplet field for all blade model sizes at constant droplet flow scaling parameters, including droplet Reynolds number, inertia parameter, and droplet drag coefficient. Higher droplet velocity magnitudes can be found over small-sized scaled sections compared to large sections.

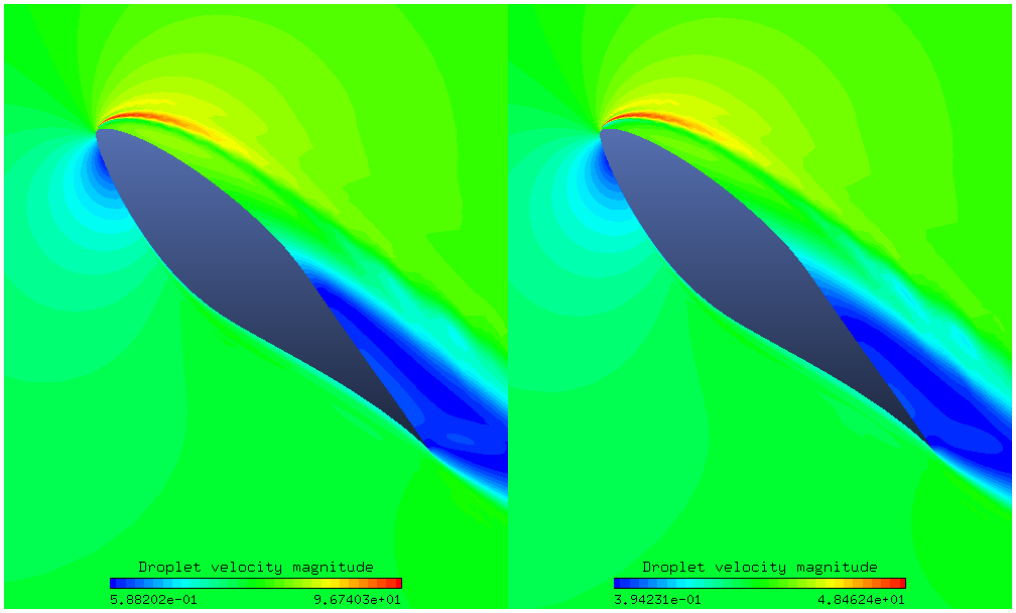

(a) k = 1 (b) k = 2

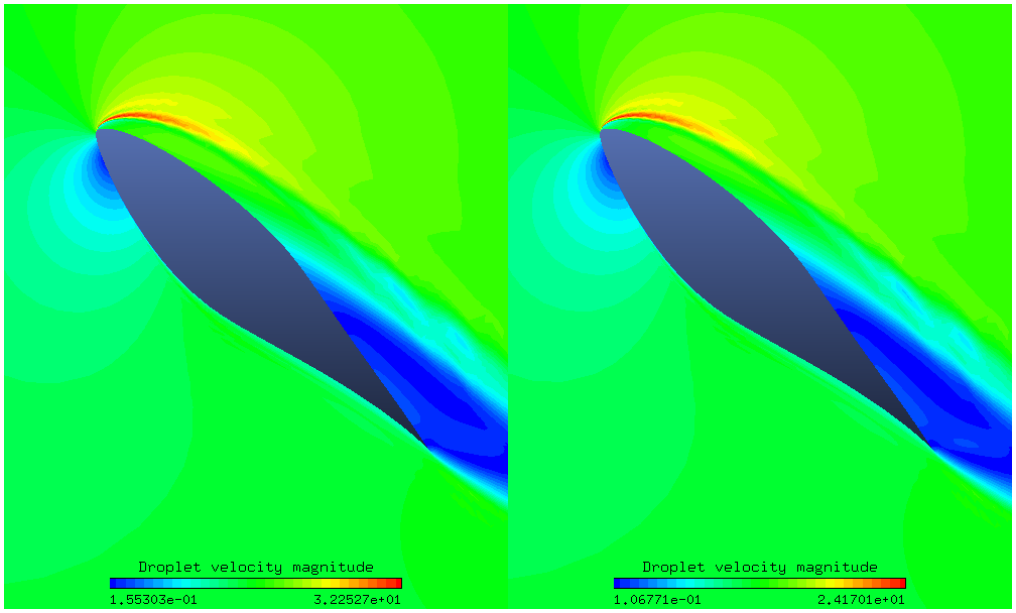

(c) k = 3 (d) k = 4

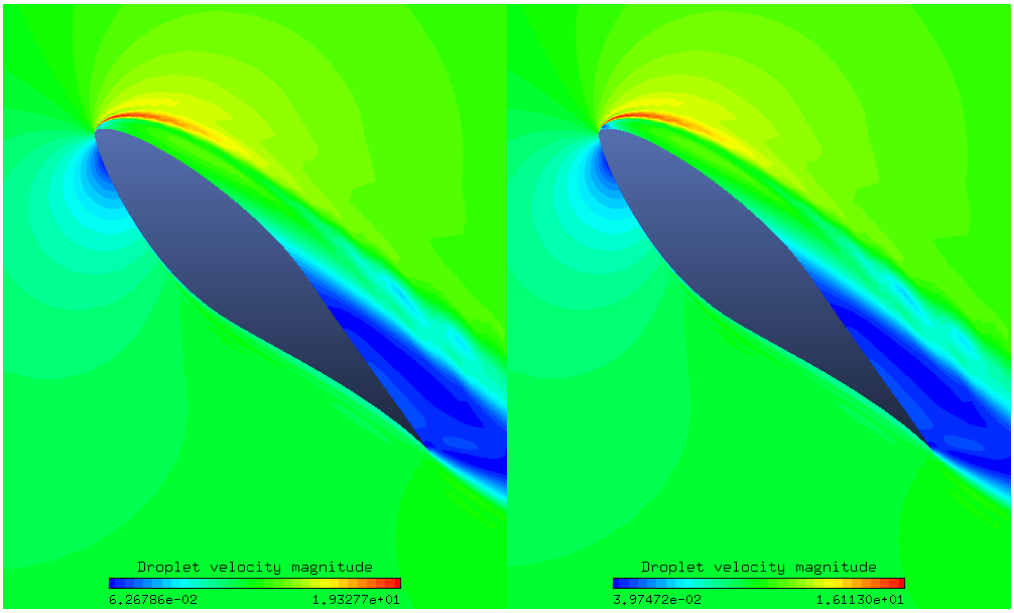

(e) k = 5 (f) k = 6

Figure 4.5. Droplet velocity contours for different model scale factors.

The liquid water volume fractions over the entire domain are computed using the DROP 3D solver. Droplet LWC contours are shown in Fig. 4.6. Results indicate that at the stagnation region on the blade surface, higher values of LWC exist. Results show that the droplet flow is usually separated at the leading edge with only water droplets at the first 30% of the chord length, causing a region of no droplets up to the trailing edge. The blue color represents this observation in each contour. The droplet concentration and separation at the leading edge are highly dependent on the flow angle of attack. Results indicate remarkable similarity at scaled droplet flow conditions. High LWCs contribute to ice formation at the associated locations, especially at the stagnation location. As illustrated in Figs. 4.7a and 4.7b, the droplet LWC magnitudes are plotted along with the horizontal and vertical directions for the blade wall surface for comparison purposes. These plots represent LWC magnitudes over each blade's surface pressure and suction sides. Results indicate a discrepancy with scaled LWC distributions around all scaled blade models at the LWC stream conditions. This represents a dimensional variable while each blade size differs. These distributions

will result in similar ice masses from a scaling perspective. Local LWC magnitudes around the blade surface, droplet velocity magnitudes, and the airfoil wetted surface determine the local droplet collection efficiency value based on Eq. (20). Considering the discrepancy in magnitudes of all Eq. (20) variables, successful scaling would be satisfied if the droplet collection efficiency values were matched between models.

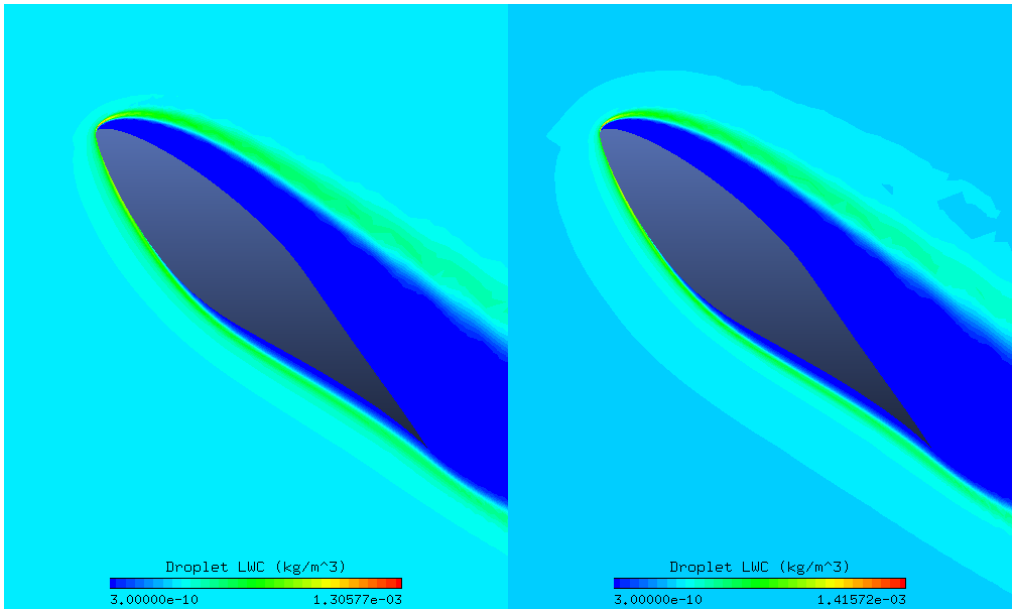

(a) k = 1 (b) k = 2

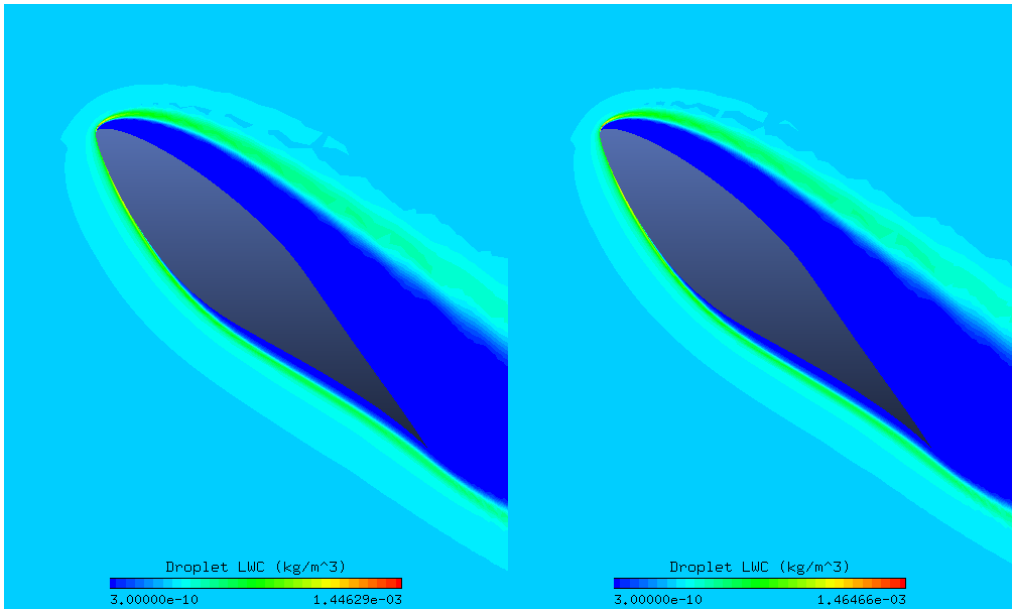

(c) k = 3 (d) k = 4

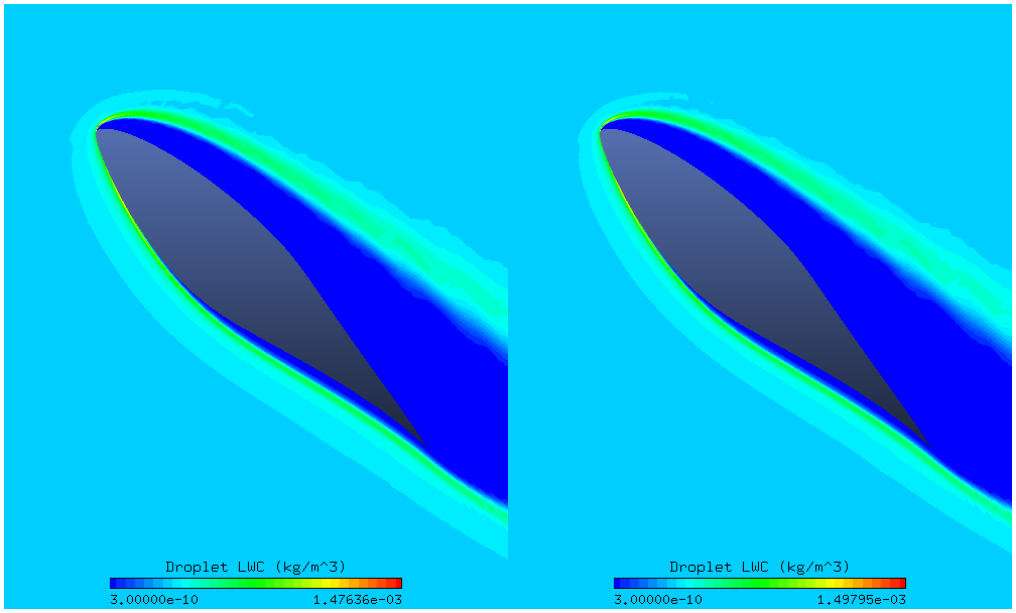

(e) k = 5 (f) k = 6

Figure 4.6. Droplet LWC contours for different model scale factors.

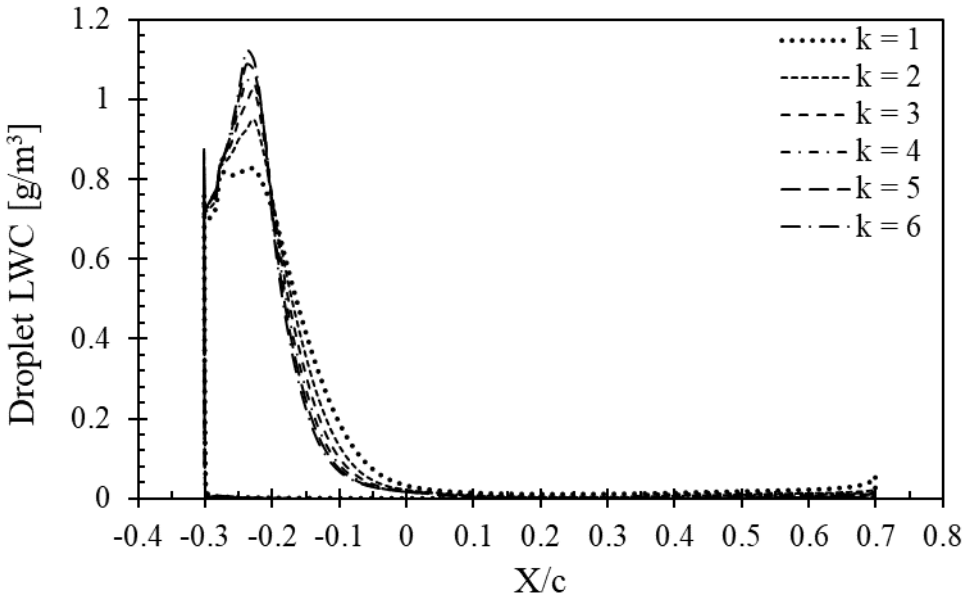

(a)

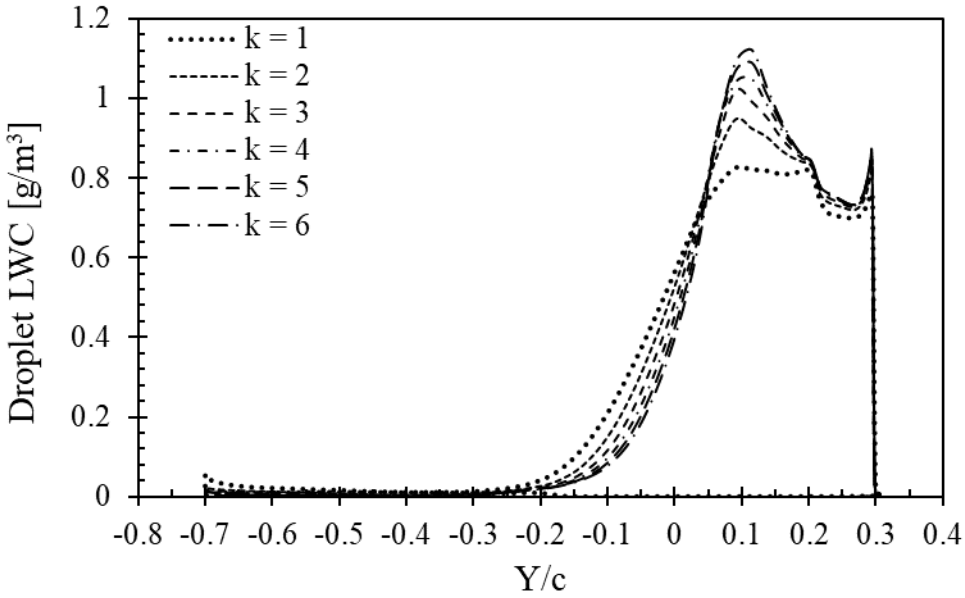

(b)

Figure 4.7. Droplet LWC distribution for different model scale factors: (a) along the x-direction and (b) along the y-direction.

Droplet collection efficiencies are also computed numerically using the DROP 3D solver. The collection efficiency magnitude typically ranges from 0 to 1, where higher values up to 1 can only exist at the stagnation point of the flow. Plots presented in Fig. 4.8a show the distribution of the collection efficiency along the horizontal direction and are highlighted at the leading-edge location where most droplets collide with the blade surface. The plots presented in Fig. 4.8b show the distribution of collection efficiency in the vertical direction. As shown in Fig. 4.8b, most droplets impinge up to 10% of the blade chord-wise direction at the leading edge. Results indicate close similarity in the collection efficiency profiles for all scaled model sizes at scaled droplet flow conditions.

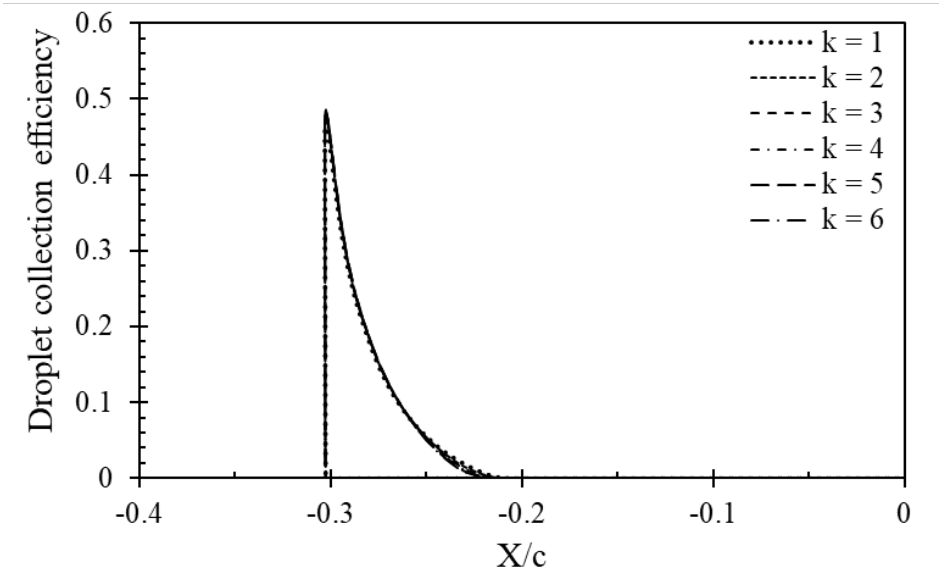

(a)

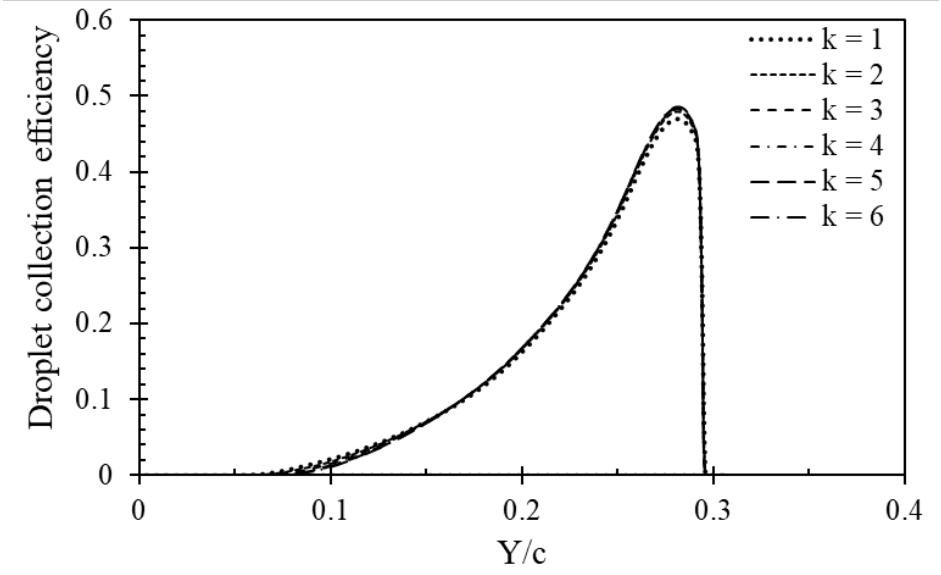

(b)

Figure 4.8. Droplet collection efficiency distribution for different model scale factors: (a) along the x-direction and (b) along the y-direction.

The ICE3D solver computes ice thickness distributions and predicts accreted ice shapes. Ice thicknesses are plotted along the horizontal and the vertical directions, all ice accretions occur at the blade's leading edge up to 10% of the chord-wise direction. Higher values of ice thicknesses accumulate at a location near the flow stagnation line. The flow angle of attack determines the location of the stagnation point and allocates the ice accretion on the blade surface. Results indicate

that all scaled blade sizes have scaled ice thicknesses at scaled icing conditions. Local ice thickness values are non-dimensionalized for comparison. Plots along the horizontal and vertical directions are presented in Figs. 4.9a and 4.9b, respectively. Results again show close similarity in the ice thickness distribution for all blades at scaled icing conditions.

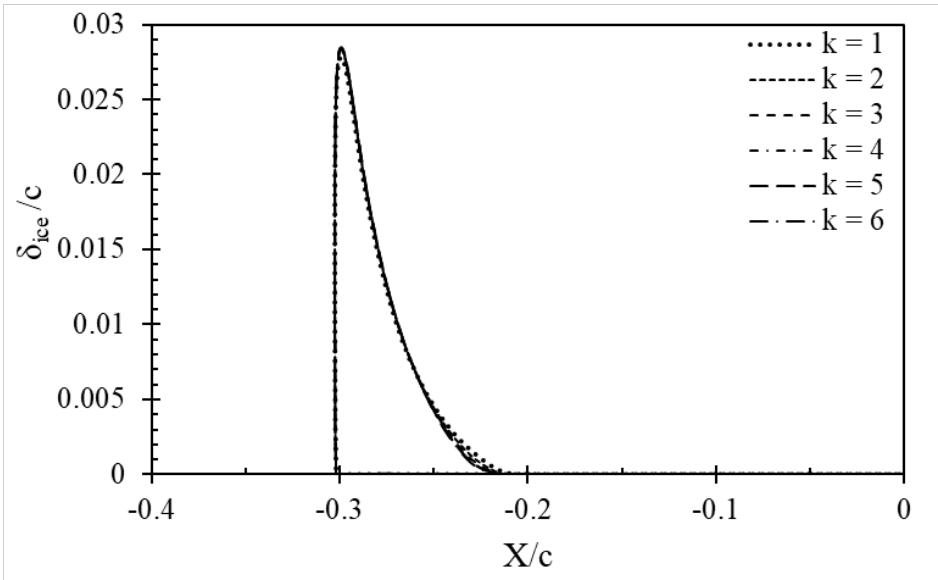

(a)

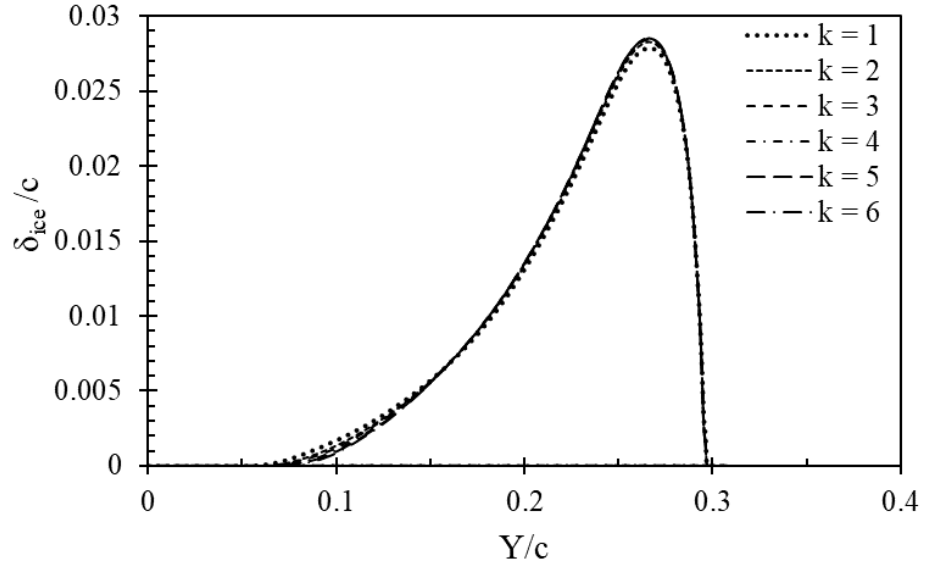

(b)

Figure 4.9. Normalized local ice thickness distribution for different model scale factors: (a) along the x-direction and (b) along the y-direction.

Ice shapes are predicted for each blade profile. As illustrated in Fig. 4.10, results show that the scaling methodology to predict scaled flow conditions allows predictions of closely similar ice shapes between all scaled model sizes and scaled icing conditions.

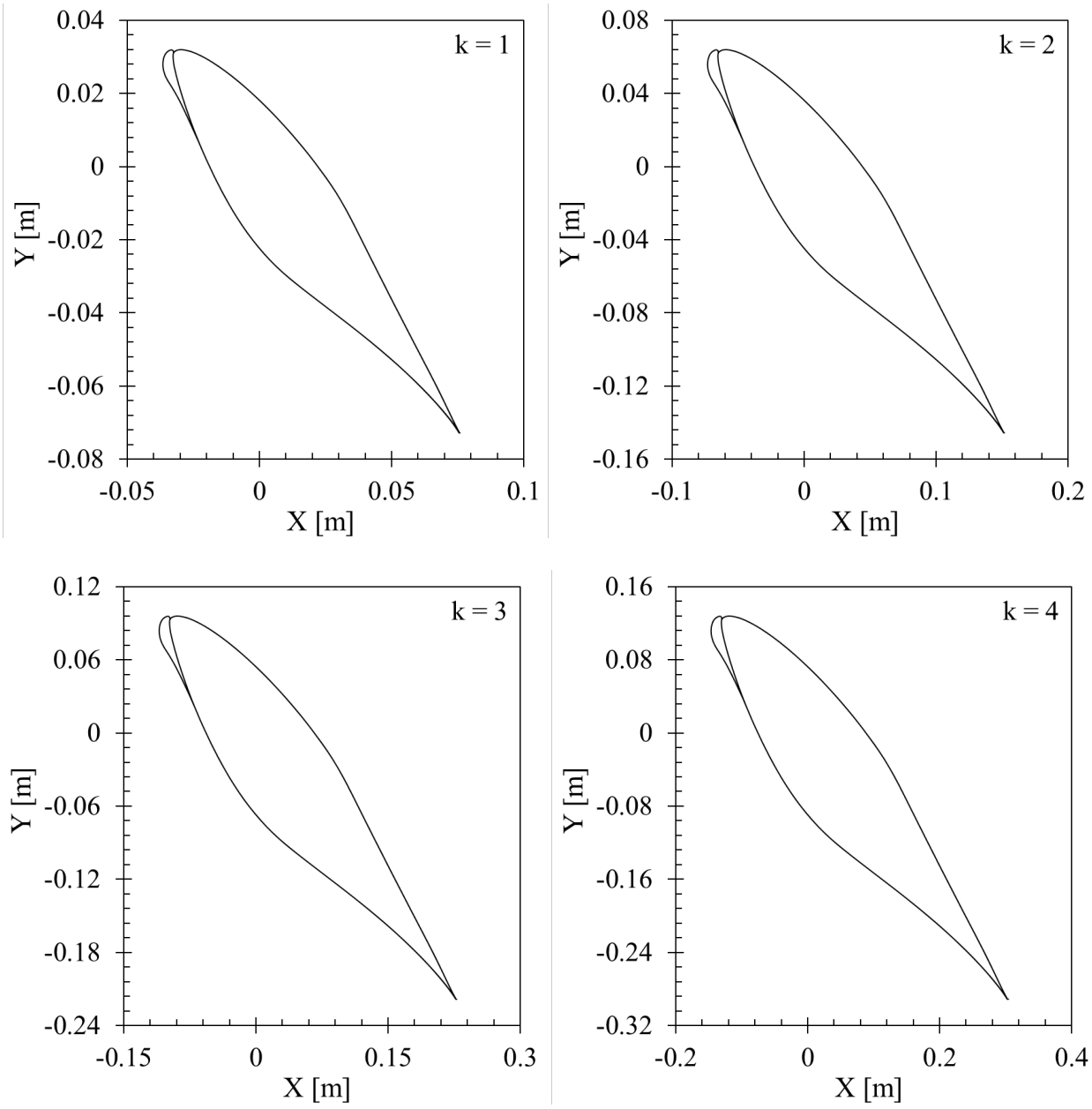

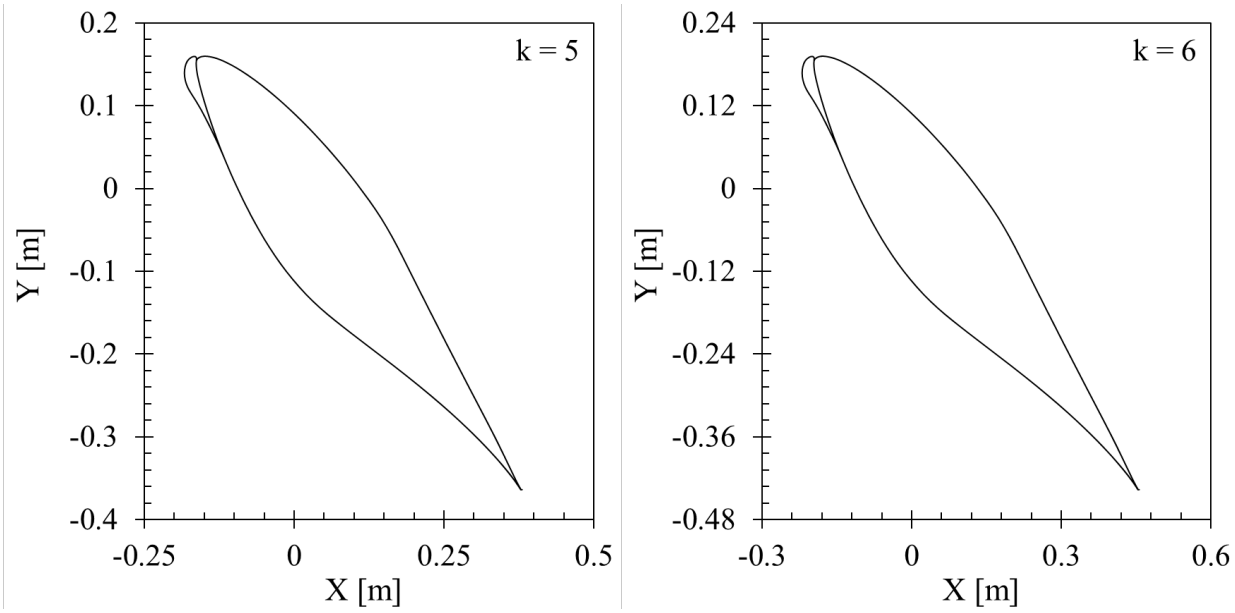

Figure 4.10. Predicted ice shapes for different model scale factors.

All values of the scaling parameters in this study as input conditions and for the flow field and rime ice scaling are presented in Table 4. As presented in Table 4.4, maintaining these dimensionless groups leads to relations to scale variables between scaled models. For result verification, comparisons for output parameters including collection efficiencies (local, total, and maximum values), normalized maximum ice thickness, and scaled ice masses are included in Table 4.4. Results show equal total β and maximum $\beta_{o_{max}}$ (i.e., at the flow stagnation point) collection efficiencies values for all the scaled blade sections, confirming the assumptions and indicating successful droplet trajectory and impingement scaling methodologies.

Table 4.4. Dimensionless scaling parameters

Inputs							
Scale factor	Re_a	$\frac{\Omega^2 R L_c}{V_{a,\infty}{}^2}$	$\frac{2\Omega L_c}{V_{a,\infty}}$	Re_d	C_d	K	A_c
1	5×10^5	0.037	0.134	26.7	2.1	0.064	81.3
2	5×10^5	0.037	0.134	26.7	2.1	0.064	81.3
3	5×10^5	0.037	0.134	26.7	2.1	0.064	81.3
4	5×10^5	0.037	0.134	26.7	2.1	0.064	81.3
5	5×10^5	0.037	0.134	26.7	2.1	0.064	81.3
6	5×10^5	0.037	0.134	26.7	2.1	0.064	81.3
Outputs							
Scale factor	$\int \beta_o dA$ [m^2]	β_{max}	β	$\delta_{\substack{ice \\ max}}$ [m]	$\frac{\delta_{\substack{ice \\ max}}}{L_c}$	m_{ice} [kg]	
1	0.00021	0.470	0.01415	0.00417	0.02784	0.002	
2	0.00087	0.480	0.01413	0.00848	0.02827	0.019	
3	0.00196	0.482	0.01410	0.01277	0.02839	0.066	
4	0.00349	0.484	0.01407	0.01707	0.02845	0.156	
5	0.00544	0.484	0.01404	0.02135	0.02847	0.304	
6	0.00783	0.485	0.01403	0.02564	0.02849	0.525	

Further analysis aims to verify the current scaling method for rime ice accretions on wind turbine blades. Experimental data [11] for rime ice scaling are compared with current scaling method predictions for a specific case. Test conditions for an Adverse Environment Rotor Test Stand (AERTS) in a wind tunnel (WT), Case 19 [11], are examined. Scaled conditions are calculated in the current study. The test conditions are shown in Table 4.5.

Table 4.5. Test conditions for rime ice scaling

Test variables	**NREL VI Rotor AERTS WT Case 19 [11]**	**Current rime ice scaling method**	
Blade airfoil	NREL S809		
Angle of attack (deg.)	8		
Radial location (r/R)	0.95		
Scale factor	1	1	2
Chord length (m)	0.2667	0.2667	0.5334
Flow stream temperature (°C)	-8.9	-8.9	-8.9
Stream velocity (m/s)	42	42	21
Rotational velocity (rpm)	84	84	21
Rotational radius (m)	1.016	1.016	2.032
LWC (g/m^3)	0.047	0.047	0.047
MVD (μm)	26.6	26.6	53.2
Icing time (mins)	54.1	54.1	216.4

As shown in Fig. 4.11, experimentally obtained non-dimensional rime ice distributions on the NREL S809 airfoil are compared with FENSAP ICE predictions at scaled conditions. The results show good agreement with experimental predictions.

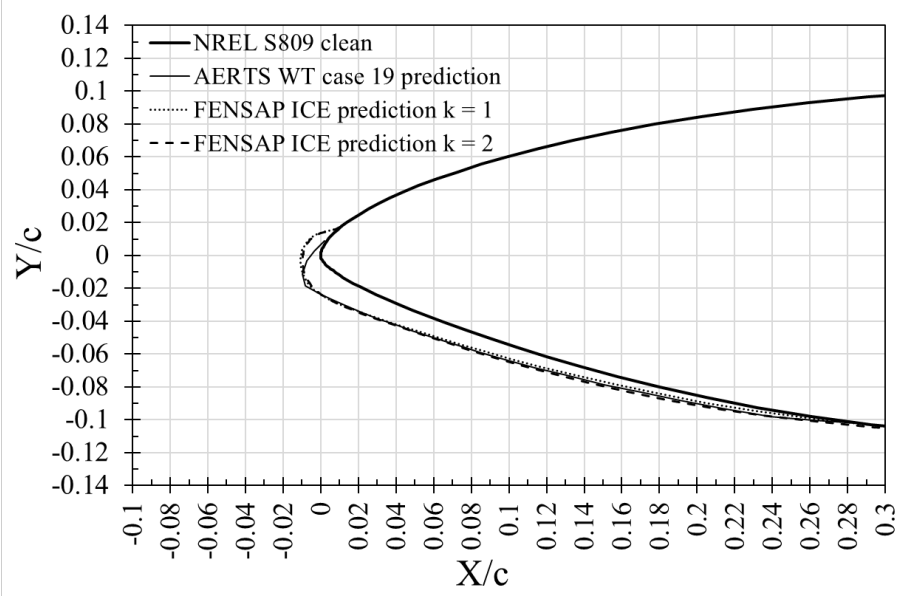

Figure 4.11. Comparison of experimental and numerical results of rime ice shapes on NREL S809 airfoil.

The study provided an analysis for the governing equations, proposed new parameters for scaling, and used them to calculate scaled flow conditions. The numerical predictions validated the methodology by producing scaled ice characteristics and the flow field around scaled geometries. Results indicate successful ice accretion scaling in terms of ice thickness and mass. The results show the corresponding scaled maximum ice thickness and total ice mass for each scaled blade model, with a minimal percentage difference of 0.5%. Results indicate equal normalized local ice thickness values as assumed for all scaled blade sections, thereby validating the ice scaling methodology in this study.

4.6. Conclusions

This study presented a scaling analysis of rime ice accretion on a rotating blade. The study described the formulation for the significant scaling parameters of the flow field, droplet trajectory, and ice accretion. Previous scaling parameters and newly derived variables were developed to scale the air and droplet flows. Significant scaling dimensionless groups include the Reynolds number, two performance speed ratios for the rotational forces, droplet inertia, drag over the droplet, and ice accumulation parameter. Scaling relations were obtained based on the change in characteristic length between scaled and reference bodies. The scaling relations can scale the flow stream velocity, blade rotational speed, blade radius, droplet size, LWC, and icing time.

The scaling method in this analysis includes both the blade section size scaling and icing conditions. The rime ice scaling was investigated numerically using FENSAP ICE software. A blade section with a specific curvature was scaled up to six times using a scale factor. The test conditions for each scaled blade section were calculated using similarity relations. The scaling method leads to nearly identical air and droplet flow fields, droplet collection and ice characteristics at different flow conditions. The results in this study provided useful insights to accurately predict

rime ice accretion on large wind turbine blade sections based on smaller blades tested in laboratory conditions. Future research will experimentally examine the applicability and limits of these scaling parameters.

References

[1] Switchenko, D., Habashi, W., Reid, T., Ozcer, I., & Baruzzi, G. (2014). FENSAP-ice simulation of complex wind turbine icing events, and comparison to observed performance data. 32nd ASME Wind Energy Symposium. https://doi.org/10.2514/6.2014-1399

[2] Kraj, A. G., & Bibeau, E. L. (2010). Measurement method and results of ice adhesion force on the curved surface of a wind turbine blade. Renewable Energy, 35(4), 741–746. https://doi.org/10.1016/j.renene.2009.08.030

[3] Reid, T., Baruzzi, G., Ozcer, I., Switchenko, D., & Habashi, W. (2013). FENSAP-ice simulation of icing on wind turbine blades, part 1: Performance degradation. 51st AIAA Aerospace Sciences Meeting Including the New Horizons Forum and Aerospace Exposition. https://doi.org/10.2514/6.2013-750

[4] Reid, T., Baruzzi, G., Ozcer, I., Switchenko, D., & Habashi, W. (2013). FENSAP-ice simulation of icing on wind turbine blades, part 2: Ice protection system design. 51st AIAA Aerospace Sciences Meeting Including the New Horizons Forum and Aerospace Exposition. https://doi.org/10.2514/6.2013-751

[5] Battisti, L. (2015). Wind turbines in cold climates: Icing impacts and mitigation systems. Springer.

[6] Ibrahim, G.M., Pope, K., & Muzychka, Y.S. (2018). Effects of blade design on ice accretion for horizontal axis wind turbines. Journal of Wind Engineering and Industrial Aerodynamics 173, 39-52. https://doi.org/10.1016/j.jweia.2017.11.024

[7] Hu, L., Zhu, X., Chen, J., Shen, X., & Du, Z. (2018). Numerical simulation of rime ice on NREL phase VI blade. Journal of Wind Engineering and Industrial Aerodynamics, 178, 57–68. https://doi.org/10.1016/j.jweia.2018.05.007

[8] Fortin, G., & Perron, J. (2009). Wind turbine icing and de-icing. 47th AIAA Aerospace Sciences Meeting Including The New Horizons Forum and Aerospace Exposition. https://doi.org/10.2514/6.2009-274

[9] Anderson, D. N. (2004). Manual of scaling methods. NASA CR, 212875.

[10] Ruff, G. A. (1985). Analysis and verification of the icing scaling equations. volume 1. https://doi.org/10.21236/ada162226

[11] Han, Y., Palacios, J., & Schmitz, S. (2012). Scaled ice accretion experiments on a rotating wind turbine blade. Journal of Wind Engineering and Industrial Aerodynamics, 109, 55–67. https://doi.org/10.1016/j.jweia.2012.06.001

[12] Potapczuk, M. G. (2013). Aircraft icing research at NASA glenn research center. Journal of Aerospace Engineering, 26(2), 260–276. https://doi.org/10.1061/(asce)as.1943-5525.0000322

[13] Anderson, D. (1995). Methods for scaling icing test conditions. 33rd Aerospace Sciences Meeting and Exhibit. https://doi.org/10.2514/6.1995-540

[14] Anderson, D. (1994). Rime-, mixed- and glaze-ice evaluations of three scaling laws. 32nd Aerospace Sciences Meeting and Exhibit. https://doi.org/10.2514/6.1994-718

[15] Bilanin, A. (1988). Proposed modifications to ice accretion/icing scaling theory. 26th Aerospace Sciences Meeting. https://doi.org/10.2514/6.1988-203

[16] Bilanin, A., & Anderson, D. (1995). Ice accretion with varying surface tension. 33rd Aerospace Sciences Meeting and Exhibit. https://doi.org/10.2514/6.1995-538

[17] Langmuir, I., & Blodgett, K. B. (1949). A mathematical investigation of water droplet trajectories. General Electric Co., Research Laboratory.

[18] Anderson, D., & Tsao, J.-C. (2003). Additional results of ice-accretion scaling at SLD conditions. 41st Aerospace Sciences Meeting and Exhibit. https://doi.org/10.2514/6.2003-390

[19] Bragg, M. B. (1982). A similarity analysis of the droplet trajectory equation. AIAA journal, 20(12), 1681-1686.

[20] Clift, R., Grace, J. R., & Weber, M. E. (2006). Bubbles, drops, and particles. Dover Publications, Inc.

[21] Naterer, G. F., Advanced Heat Transfer, 3rd Edition, CRC Boca Raton, FL, 2022.

[22] ANSYS, (2015). FENSAP-ICE User Manual R1.0, Canada.

[23] Anderson, D. (1996). Further evaluation of traditional icing scaling methods. 34th Aerospace Sciences Meeting and Exhibit. https://doi.org/10.2514/6.1996-633

[24] NREL's S809 airfoil (S809-NR). (n.d.). Retrieved September 21, 2022, from http://airfoiltools.com/airfoil/details?airfoil=s809-nr

[25] Spalart, P., & Allmaras, S.. (1992). A one-equation turbulence model for aerodynamic flows. 30th Aerospace Sciences Meeting and Exhibit. https://doi.org/10.2514/6.1992-439.

Chapter 5

5. Extended Scaling Approach for Droplet Flow and Glaze Ice Accretion on a Rotating Wind Turbine Blade

This study presents and analyzes a non-dimensional model of the flow field and droplet trajectories with glaze ice accretion on a rotating wind turbine blade. The formulation leads to similitude relationships for glaze ice accretion to evaluate new scaling parameters corresponding to the rotation of the blade. New scaling parameters are developed to determine ice scaling conditions based on the geometry scale factor of a wind turbine blade. The scaling methodology can be used to determine alternative test conditions and predict glaze icing conditions on a full-scale wind turbine blade. Numerical CFD icing simulations are performed using ANSYS FENSAP ICE software. A turbine blade model is developed using blade element momentum theory (BEM). Each blade size is tested at specific flow conditions using the scaling equations.

Scaled conditions for velocity (streamwise and rotational), droplet size, and icing time are tested. CFD solutions for the flow field are obtained for comparisons of the velocity, droplet trajectories, pressure coefficient distributions, ice thickness, and ice shapes. Recommended parameters to be used for glaze ice scaling on a rotating blade are presented and numerical results are reported to support these recommendations. The study provides new insights into modeling of glaze ice accretion on large wind turbine blades based on smaller scaled blade sections tested in a laboratory setting.

Nomenclature

A Area (m^2)

A_c Ice accumulation parameter

b Relative heat factor

c Chord length (m)

c_p Specific heat capacity (J/kg.K)

F_{ce} Centrifugal force (N)

F_{co} Coriolis forces (N)

d Diameter (m)

$\vec{D}$ Drag force (N)

C_d Droplet drag coefficient

Eu Euler number

E Total internal energy (kJ)

$\dot{E}$ Energy rate (J/s)

Fr Froude number

g Gravitational acceleration (m/s^2)

H Total enthalpy (kJ)

h Heat transfer coefficient ($W/m^2.K$)

h_g Gas phase mass transfer by diffusion ($kg/s.m^2$)

k Scale factor

K Droplet inertia parameter

L Latent heat (kJ/kg)

Le Lewis number

L_c Characteristic length (m)

m Mass (kg)

$\dot{M}$ Mass flux ($kg/m^2.s$)

$\dot{m}$ Mass flow rate (kg/s)

Ma Mach number

Nu Nusselt number

n Freezing fraction

$\vec{n}$ Normal surface vector

Pr Prandtl number

P Pressure (Pa)

$\dot{q}$ Heat transfer (J/s)

R Radius (m)

Re Reynolds number

R_v Gas constant

REC Recovery factor

r Distance to the axis of rotation (m)

Sc Schmidt number

St Strouhal number

T Temperature (°C)

t Time (s)

V Velocity (m/s)

Latin and Greek symbols:

β Total collection efficiency

β_o Local collection efficiency

ε Surface emissivity (J/m^2)

κ Thermal conductivity (W/m.K)

ϑ Volume (m^3)

Ω Rotational velocity (rad/s)

ρ Density (kg/m^3)

μ Dynamic viscosity (Pa·s)

δ_{ij} Kronecker delta

τ_{ij} Shear stress tensor (N/m^2)

α Local water volume fraction (kg/m^3)

γ Specific heat ratio

θ Air energy transfer parameter (°C)

ϕ Droplet energy transfer parameter (°C)

σ Stefan-Boltzmann constant (W/m^2.K^4)

α Thermal diffusivity (m^2/s)

δ Thickness (m)

λ_r Local tip speed ratio

Abbreviations

$AEDC$ Arnold Engineering Development Center

BEM Blade Element Momentum theory

CFD Computational Fluid Dynamics

IRT Icing Research Tunnel

LWC Liquid Water Content

$NREL$ National Renewable Energy Laboratory

MVD Median Volume Diameter

Ps Parameters

TSR Tip speed ratio

Subscripts and Superscripts

a Air

a Axial induction factor

c Accumulation

$conde/evap$ Condensation/evaporation

$cond$ Conduction

cv Convection

cd Conduction

d Droplet

$evap/subl$ Evaporation/Sublimation

e Edge of boundary layer

ext External

f Oscillation frequency

f Full-scale model, film

$freeze/melt$ Freezing / melting

$film$ Film

g Gas-phase

h Height

imp Impingement

in Into system

i Specific internal energy, inlet

ice Ice

o Initial conditions/Local

out Out of the system

p Position of interest

R Relative

rec Recovery

r Distance from the axis of rotation

ref Reference conditions

rad Radiation

$Storage$ Stored in the system

s Scaled model

v Vapour

w Wall

∞ Stream conditions

5.1. Introduction

Icing of wind turbines can significantly reduce the power output of wind farms located in cold climates [1, 2]. Ice accumulates on surfaces exposed to windy environments in cold climates with frost, snow, and/or freezing rain [3]. Super-cooled droplets include freezing drizzle and freezing rain [4]. The formation of ice on a wind turbine surface occurs through impingement of super-cooled droplets. Each layer of ice layer is formed upon the previous layer. The process is governed by the impingement of super-cooled water droplets and the local thermodynamics of the freezing process on the blade surface [5]. Ice accretion on a blade surface usually degrades its aerodynamic performance [6, 7] by decreasing lift and increasing drag [8, 9]. Scaling methods using wind tunnel tests and computational tools are common approaches for assessing wind turbine performance during icing conditions.

Scaling methods aim to match conditions of the flow field, droplet trajectories, and amount of accumulated ice so they are equivalent between different geometries. The predicted ice characteristics in terms of type, shape, distributed thickness, and the aerodynamic processes due to icing are the same as they would have occurred for the desired test conditions for a reference blade size. Glaze ice accretions can be severe for wind turbines, especially at near-zero temperatures [10]. Glaze ice accretion usually forms at temperatures ranging from -6 °C to 0 °C. It mainly forms in conditions with a high liquid water content and large droplet sizes in the atmosphere. Glaze ice appears nearly transparent. It has a high density of around 900 kg/m^3, and forms horns and feathers, which can be distributed along a portion of the surface due to runback [10-12].

The heat transfer and surface water flows are key processes in glaze ice scaling analyses. Convective cooling effects of the ambient air and the energy released by evaporation significantly impact the icing process. Only a fraction of cold water droplets freeze in the impingement area as

they collide with an exposed surface where the local temperature is nearly freezing. The resulting layer of liquid surface water influence the shape of the accreted ice. Shear stresses, aerodynamic forces, and gravity affect the remaining liquid water droplets to run back and freeze downstream [13, 14]. Characteristic features of ice include the size, quantity, position, angle, and shape. The degree to which these characteristics are related between lab-scale and actual field measurements has been reported previously [15-17].

Ice scaling methods are procedures to analyze scaled test conditions to predict actual icing conditions on large-scale wind turbines. Due to wind tunnel size limitations, various components of wind turbines cannot be tested in a laboratory at their full size. Furthermore, wind tunnel facilities for icing investigations can only provide limited ranges of airflow speeds, rotational speeds of components, temperatures, droplet sizes and liquid-water contents. Thus, reference model scaling and test-condition scaling are needed when the desired test conditions are outside the facility's operating capability [15, 16]. Past studies have used scaled conditions in icing wind tunnels to study ice characteristics [18].

Previous studies used different ice scaling methods for aircraft icing scaling. These have used similitude analyses to provide a set of scaling equations that can be solved to analyze the reference conditions using scaled icing conditions. Simplifications are typically needed to allow the scaling equations to be used in real-world ice conditions [18-22]. Aircraft scaling tests were performed at the Arnold Engineering Development Center (AEDC) and NASA Glenn's Icing Research Tunnel (IRT) using different scaling methods by matching the scale and reference values of the similarity parameters.

Six similarity parameters are commonly used for ice scaling. These parameters include a droplet inertia parameter to ensure similarity in droplet trajectories, an ice accumulation parameter to ensure similarity in total ice quantity, and four other parameters derived from the energy balance:

the freezing fraction, relative heat factor, an air energy transfer parameter and water energy transfer parameter [18-23]. Ruff [20] analyzed the icing scaling equations, conducted experimental investigations, and developed scaling laws based on five similarity parameters.

The matching of each scaling parameter to its respective reference value allows the scaling of MVD, time, LWC, temperature and pressure. Bilanin [24] presented a non-dimensional analysis using the Buckingham-Pi theory and further recommended [14] the Weber's number as a similarity parameter to scale surface water effects. Anderson and Bilanin [18, 24] used the Weber number for icing scaling methods and conducted experiments for result verification in the NASA Lewis Icing Research Tunnel (IRT). Anderson and Ruff [20, 25] reported scaling results for glaze ice based on the Weber and Reynold numbers. Langmuir analyzed water droplet trajectories using a mathematical model and proposed a range parameter [26]. Anderson and Bragg [20, 27] also reported droplet trajectory scaling methods and similarity parameters, including an inertia parameter, Froude number (Fr), and droplet Reynolds number.

Unlike past studies, this study aims to develop scaling parameters that can scale ice accretions on a rotating blade. Previous scaling studies for aircraft icing were created for icing processes over stationary models and have not been applied or tested for a rotating turbine blade. This study's findings extend previous aircraft icing scaling methods, test their applicability, and introduce new scaling parameters for ice scaling on a rotating wind turbine blade. The scaling approach in this study will introduce new parameters to scale the rotational forces in the flow field, droplet trajectory, and ice accretion over a rotating blade.

5.2. Flow Field Formulation and Scaling Parameters

The continuity and momentum equations will be converted to a relative frame of reference for a rotating blade to account for rotational effects. In cartesian tensor notation,

$$\frac{\partial \rho_a \vec{V}_{R,a}}{\partial t} + \nabla \cdot \left[\rho_a \vec{V}_{R,a} \vec{V}_{R,a}\right] = \rho_a \vec{g} + \nabla \cdot \left[-\delta_{ij} p_a + \tau_{ij}\right] + \vec{F}_{ext} \tag{1}$$

$$\vec{F}_{ext} = \vec{F}_{co} + \vec{F}_{ce} = -2\rho\left[\vec{\Omega} \times \vec{V}\right] - \rho\vec{\Omega} \times \left[\vec{\Omega} \times \vec{r}\right] \tag{2}$$

where $\vec{F}_{ext}$ represents external forces in the momentum equation which consists of the Coriolis force $\vec{F}_{co}$ and the centrifugal force $\vec{F}_{ce}$. Substituting Eq. (2) into (1), the momentum equation becomes:

$$\frac{\partial \rho_a \vec{V}_{R,a}}{\partial t} + \nabla \cdot \left[\rho_a \vec{V}_{R,a} \vec{V}_{R,a}\right] = \rho_a \vec{g} + \nabla \cdot \left[-\delta_{ij} p_a + \tau_{ij}\right] - \rho_a \vec{\Omega} \times \left[\vec{\Omega} \times \vec{r}\right] - 2\rho_a\left[\vec{\Omega} \times \vec{V}_{R,a}\right] \tag{3}$$

where δ_{ij} is the Kronecker delta ($\delta = 0$ for $i \neq j$ and $\delta = 1$ for $i = j$) and τ_{ij} is the stress tensor,

$$\tau_{ij} = \mu_a \left[\delta_{jk} \nabla_k v^i + \delta_{ik} \nabla_k v^j - \frac{2}{3} \delta_{ij} \nabla_k v^k\right] \tag{4}$$

The energy conservation equation can be written as:

$$\frac{\partial \rho_a E_{R,a}}{\partial t} + \nabla \cdot \left[\rho_a \vec{V}_{R,a} H_{R,a}\right] = \rho_a \vec{g} \cdot \vec{V}_{R,a} + \nabla \cdot \left[\kappa_a [\nabla T_a] + V_{R,i} \tau_{ij}\right] \tag{5}$$

where κ, E and H are the air's relative thermal conductivity, internal energy and total enthalpy,

$$E_{R,a} = e + \frac{1}{2}\left[\vec{V}_{R,a}{}^2 - \left[\vec{\Omega} \times \vec{r}\right]^2\right] \tag{6}$$

$$H_{R,a} = h + \frac{1}{2}\left[\vec{V}_{R,a}{}^2 - \left[\vec{\Omega} \times \vec{r}\right]^2\right] \tag{7}$$

where $\vec{V}_{R,a}$ is the relative velocity in the rotating frame of reference, and $\left[\vec{\Omega} \times \vec{r}\right]$ is the tangential velocity of the rotating frame.

Various models can be used for flow turbulence, including Spalart-Allmaras, and k-ε/ω turbulence models. The effects of turbulence will be represented in the momentum equations via the eddy viscosity hypothesis. The air continuity and momentum equations for a rotating blade in a relative frame of reference become:

$$\frac{\partial \rho_a}{\partial t} + \vec{\nabla} \cdot \left[\rho_a \vec{V}_{R,a}\right] = 0 \tag{8}$$

$$\rho_a \left[\frac{\partial \vec{V}_{R,a}}{\partial t} + \left[\vec{V}_{R,a} \cdot \vec{\nabla}\right]\vec{V}_{R,a}\right] = \rho_a \vec{g} - \vec{\nabla} p_a + \mu_a \nabla^2 \vec{V}_{R,a} - \rho_a \vec{\Omega} \times \left[\vec{\Omega} \times \vec{r}\right] - 2\rho_a \left[\vec{\Omega} \times \vec{V}_{R,a}\right] \tag{9}$$

where the last two terms in Eq. (9) represent the Coriolis and centrifugal forces.

Table 5.1. Definitions of the scaling parameters

Scaling parameters	Definition
L_c	Characteristic length (m)
V_R	Characteristic relative speed (m/s)
f	Characteristic flow oscillating frequency (1/s)
Ω	Characteristic rotational speed (rad/s)
R	Characteristic distance to the axis of rotation (m)
$P_o - P_\infty$	Reference pressure difference (N/m^2)
g	Gravitational acceleration (m/s^2)

Defining non-dimensional variables using scaling parameters in Table 5.1,

$$t^* = \mathrm{f}t\,, \vec{V}^*{}_{R,a} = \frac{\vec{V}_{R,a}}{V_{a,\infty}}\,, \vec{\nabla}^* = \vec{\nabla} L_c\,, \vec{g}^* = \frac{\vec{g}}{g}, P^* = \frac{p_a}{P_o - P_\infty}\,, \vec{r}^* = \frac{\vec{r}}{R}\,, \vec{\Omega}^* = \frac{\vec{\Omega}}{\Omega}$$
$$t = \frac{t^*}{\mathrm{f}}\,, \vec{V}_{R,a} = V_{a,\infty} \vec{V}^*{}_{R,a}\,, \vec{g} = g\vec{g}^*\,, \vec{\nabla} = \frac{\vec{\nabla}^*}{L_c}\,, p_a = P^*[P_o - P_\infty]\,, \vec{r} = R\vec{r}^*\,, \vec{\Omega} = \Omega\vec{\Omega}^* \tag{10}$$

Rearranging variables in Eq. (10) and using them in Eq. (9),

$$\rho_a \mathrm{f} V_{a,\infty} \frac{\partial \vec{V}^*{}_{R,a}}{\partial t^*} + \frac{\rho_a {V_{R,a}}^2}{L_c}\left[\vec{\nabla}^* \cdot \vec{V}^*{}_{R,a}\right]\vec{V}^*{}_{R,a} = \rho_a g \vec{g}^* - \left[\frac{(P_o - P_\infty)}{L_c}\right]\vec{\nabla}^* P^* +$$
$$\left[\frac{\mu_a V_{a,\infty}}{{L_c}^2}\right]{\vec{\nabla}^*}^2 \vec{V}^*{}_{R,a} - \rho_a \Omega^2 R \vec{\Omega}^* \times \left[\vec{\Omega}^* \times \vec{r}^*\right] - 2\rho_a \Omega V_{a,\infty}\left[\vec{\Omega}^* \times \vec{V}^*{}_{R,a}\right] \tag{11}$$

After some rearrangement, the non-dimensional form of Eq. (11) can be rewritten in terms of significant dimensionless parameters for the flow field as follows,

$$[St]\frac{\partial \vec{V}^*{}_{R,a}}{\partial t^*} + \left[\vec{\nabla}^* \cdot \vec{V}^*{}_{R,a}\right]\vec{V}^*{}_{R,a} = \left[\frac{1}{Fr^2}\right]\vec{g}^* - [Eu]\vec{\nabla}^* P^* + \left[\frac{1}{Re_a}\right]{\vec{\nabla}^*}^2 \vec{V}^*{}_{R,a} -$$
$$\left[\frac{\Omega^2 R L_c}{{V_{a,\infty}}^2}\right]\vec{\Omega}^* \times \left[\vec{\Omega}^* \times \vec{r}^*\right] - \left[\frac{2\Omega L_c}{V_{a,\infty}}\right]\left[\vec{\Omega}^* \times \vec{V}^*{}_{R,a}\right] \tag{12}$$

where St, Fr, Eu, Re are the Strouhal, Froude, Euler, and stream Reynolds numbers, respectively. The Strouhal number describes the oscillating flow mechanisms, while the Froude number represents the ratio of inertial forces to gravitational flow forces. The Euler number describes pressure forces to inertial forces, and the Reynolds number describes the inertial forces to viscous forces. The last two terms represent newly-found dimensionless groups describe the rotational and inertial forces in flow. These dimensionless terms are a function of the air relative velocity for a rotating blade in the relative frame of reference. The dimensionless groups, including the stream Reynolds number and the newly found groups in Eq. (12), will be used to scale the flow field around a rotating blade.

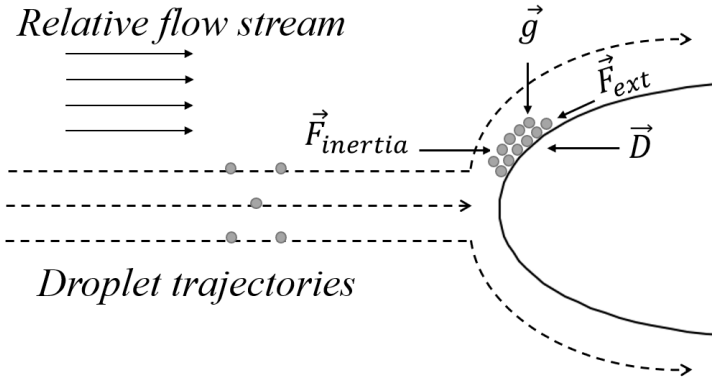

Figure 5.1. Schematic of forces over rotating blade with impinging droplets.

These equations are modified for rotating blades to include the rotational body forces acting on a droplet. As shown in Fig 5.1, the forces on a droplet include inertial, gravitational, drag and external forces. The droplet continuity and momentum equations for a rotating blade in the relative frame of reference are expressed as:

$$\frac{\partial \alpha}{\partial t} + \vec{\nabla} \cdot \left[\alpha \vec{V}_{R,d}\right] = 0 \tag{13}$$

$$\alpha \rho_d \vartheta_d \left[\frac{\partial \vec{V}_{R,d}}{\partial t} + \left[\vec{V}_{R,d} \cdot \vec{\nabla}\right]\vec{V}_{R,d}\right] = \alpha[\rho_d - \rho_a]\vartheta_d \vec{g} + \alpha \vec{D} + \alpha \vec{F}_{ext} \tag{14}$$

$$\alpha\rho_d\vartheta_d\left[\frac{\partial\vec{V}_{R,d}}{\partial t}+\left[\vec{V}_{R,d}\cdot\vec{\nabla}\right]\vec{V}_{R,d}\right]=\alpha[\rho_d-\rho_a]\vartheta_d\vec{g}+\alpha\vec{D}-\alpha\rho_d\vartheta_d\vec{\Omega}\times\left[\vec{\Omega}\times\vec{r}\right]-2\alpha\rho_d\vartheta_d\left[\vec{\Omega}\times\vec{V}_{R,d}\right] \tag{15}$$

where α is the water volume fraction and ϑ_d is the droplet volume. The droplet shape is assumed spherical. The drag force over a droplet moving in the relative flow stream is expressed as:

$$\vec{D}=\frac{1}{2}\rho_a C_d A_d\left|\vec{V}_a-\vec{V}_d\right|^2 \tag{16}$$

where $\vec{V}_{a,\infty}$ represents the air velocity tangent to the trajectory line of the droplet particle and C_d is the droplet drag coefficient. The droplet Reynolds number is defined as:

$$Re_d=\frac{\rho_a d\left|\vec{V}_a-\vec{V}_d\right|}{\mu_a} \tag{17}$$

Substituting the air density from Eq. (17) into (16), as well as the spherical droplet volume, and rearranging, Eq. (15) becomes:

$$\frac{\partial\vec{V}_{R,d}}{\partial t}+\left[\vec{V}_{R,d}\cdot\vec{\nabla}\right]\vec{V}_{R,d}=\left[1-\frac{\rho_a}{\rho_d}\right]\vec{g}+\left[\frac{3}{4}\frac{C_d Re_d\mu_a}{\rho_d d^2}\right]\left|\vec{V}_a-\vec{V}_d\right|-\vec{\Omega}\times\left[\vec{\Omega}\times\vec{r}\right]-2\left[\vec{\Omega}\times\vec{V}_{R,d}\right] \tag{18}$$

For droplet trajectory scaling, the significant scaling parameters can be obtained by non-dimensionalization of Equation (18). Considering scaling variables for the droplet flow,

$$t^*=\mathrm{ft}\,,\vec{V}^*{}_{R,d}=\frac{\vec{V}_{R,d}}{V_{a,\infty}}\,,\vec{\nabla}^*=\vec{\nabla}L_c\,,\vec{g}^*=\frac{\vec{g}}{g}\,,\vec{r}^*=\frac{\vec{r}}{R}\,,\vec{\Omega}^*=\frac{\vec{\Omega}}{\Omega}$$
$$t=\frac{1}{\mathrm{f}}t^*\,,\vec{V}_{R,d}=V_{a,\infty}\vec{V}^*{}_{R,d}\,,\vec{\nabla}=\frac{\vec{\nabla}^*}{L_c}\,,\vec{g}=g\vec{g}^*\,,\vec{r}=R\vec{r}^*\,,\vec{\Omega}=\Omega\vec{\Omega}^* \tag{19}$$

Rearranging, the non-dimensional form of the droplet momentum equation becomes:

$$[St]\frac{\partial\vec{V}^*{}_{R,d}}{\partial t^*}+\left[\vec{V}^*{}_{R,d}\cdot\vec{\nabla}^*\right]\vec{V}^*{}_{R,d}=\left[1-\frac{\rho_a}{\rho_d}\right]\left[\frac{1}{Fr^2}\right]\vec{g}^*+\left[\frac{C_d Re_d}{24K}\right]\left[\vec{V}^*{}_a-\vec{V}^*{}_d\right]-\left[\frac{\Omega^2 RL_c}{V_{a,\infty}{}^2}\right]\vec{\Omega}^*\times\left[\vec{\Omega}^*\times\vec{r}^*\right]-\left[\frac{2\Omega L_c}{V_{a,\infty}}\right]\left[\vec{\Omega}^*\times\vec{V}^*{}_{R,d}\right] \tag{20}$$

where St, Fr, C_d, Re_d and K are the Strouhal, Froude, drag coefficient over the droplet and droplet Reynolds numbers, and droplet inertia parameter, respectively. The dimensionless droplet inertia parameter K was derived in past literature [15-31] as:

$$K = \frac{\rho_d d^2 V_{a,\infty}}{18 \mu_a L_c} \tag{21}$$

where d is the droplet size. The last two terms represent newly-found groups for the rotating reference frame. These dimensionless terms are functions of the droplet velocity and air stream velocity for a rotating blade in the relative frame of reference.

The dimensionless groups, including droplet Reynolds number, droplet inertia parameter, and droplet drag coefficient in Eq. (21), are used to scale the droplet trajectories around a rotating blade section. Empirical correlations [12, 32, 33] are used to obtain the drag coefficient for the droplet as a function of the Reynolds number for specified ranges. If the Stokes law is applied for flow around a sphere at a small Reynolds number, $Re_d < 1$, the droplet drag coefficient is obtained by $C_d = \frac{24}{Re_d}$ for extended values of Re_d around spherical droplets. Over a wider range of Reynolds numbers, the droplet drag coefficient is obtained by:

$$\begin{gathered} C_d = \left[\frac{24}{Re_d}\right]\left[1 + 0.1935 {Re_d}^{0.6305}\right] \quad \text{for } 20 \le Re_d \le 260 \\ C_d = \left[\frac{24}{Re_d}\right]\left[1 + 0.15 {Re_d}^{0.687}\right] \quad \text{for } Re_d \le 1300 \\ C_d = 0.4 \quad \text{for } Re_d > 1300 \end{gathered} \tag{22}$$

The droplet internal energy transport equation of the droplets can be written as:

$$\frac{\partial E}{\partial t} + \frac{\partial \left[v_j E\right]}{\partial x_j} = \alpha\left[\dot{q}_{conv} + \dot{q}_{conde/evap} + \dot{q}_{rad} + \dot{q}_{freeze/melt}\right] \tag{23}$$

where E is the total internal energy of the droplet, and the terms on the right side represent the energy transfer between the droplets and airflow. This includes convection, absorption or emission

due to radiative heat transfer and additional mass coupling effects that cause condensation/evaporation and freezing/melting. The total internal energy is expressed as:

$$E = \alpha i = \alpha \left[i_{ref} + \int_{T_{ref}}^{T_i} c_p[T] dT \right] \tag{24}$$

where i represents the specific internal energy of the droplet and c_p is the specific heat of the droplets.

Upon droplet impingement on the ice surface, the total collection efficiency is a dimensionless parameter that indicates how many droplets are collected by the surface. It represents the ratio of the actual mass of impinging droplets to the maximum value that would occur if the droplets followed straight-line trajectories. Langmuir and Blodgett [26] developed correlations of the local collection efficiency at the flow stagnation location using a modified droplet inertia parameter. The local and total collection efficiency can be defined in vector form [34, 35] as:

$$\beta_o = -\frac{\alpha \vec{V}_d \cdot \vec{n}}{LWC_\infty V_{a,\infty}} \tag{25}$$

$$\beta = \frac{\int \beta_o dA}{{L_\infty}^2} = \frac{\int \beta_o dA}{A_{imp}} \tag{26}$$

where α is the local water volume fraction, $\vec{n}$ is the normal surface vector, LWC_∞ is the stream liquid water content and A_{imp} is the total impingement area. This area can be calculated by multiplying the object's surface perimeter by the span-wise length.

Consider a flow stream in a tube that contains droplets distributed with different sizes and liquid water content. The local collection efficiency is the fraction of the liquid water content that impacts the blade. The smaller droplets in the distribution will mostly follow the air streamline around the blade, while the larger droplets will be more likely to strike the blade surface. By applying the mass

conservation equation across two terminals of a flow streamline, the local collection efficiency is defined in a two-dimensional coordinate system as:

$$\beta_{xy} = \frac{A_{\infty,i}}{A_p} = \frac{LWC_p\vec{V}_p}{LWC_{\infty,i}\vec{V}_{\infty,i}} \tag{27}$$

where i and p refer to the stream inlet and blade's surface position of interest. When an entire blade rotates in the relative frame of reference, the blade moves due to the applied relative velocity at that position of interest and its magnitude changes radially along the blade span in the z-direction. Thus, the 3-D definition of the local collection efficiency becomes:

$$\beta_{xyz} = \frac{LWC_p\vec{V}_{R,p}}{LWC_{\infty,i}\vec{V}_{\infty,i}} = \frac{A_{\infty,i}\vec{V}_{R,p}}{A_p\vec{V}_p} = \beta_{xy}\frac{\vec{V}_{R,p}}{\vec{V}_p} \tag{28}$$

The streamline expansion can be expressed by an induction factor a, which is the fractional decrease in wind velocity between the freestream and wind turbine rotor. It is expressed as:

$$a = \frac{\vec{V}_{\infty,i} - \vec{V}_p}{\vec{V}_{\infty,i}} \qquad \vec{V}_p = \vec{V}_{\infty,i}(1-a) \tag{29}$$

The relative velocity acting on the rotating blade is found by:

$$\vec{V}_{R,p} = \sqrt{\vec{V}_p{}^2 + \left[\vec{\Omega}\times\vec{r}\right]^2} = \sqrt{\left[\vec{V}_{\infty,i}(1-a)\right]^2 + \left[\vec{\Omega}\times\vec{r}\right]^2} \tag{30}$$

Define the local speed ratio, λ_r at a distance r along the blade span and relate it to the blade tip speed ratio λ at a full radius R as:

$$\lambda_r = \frac{\vec{\Omega}\times\vec{r}}{\vec{V}_{\infty,i}} \qquad \lambda_r = \lambda\left[\frac{r}{R}\right] \tag{31}$$

Substituting Eq. (31) into (30) and rearranging leads to:

$$\frac{\vec{V}_{R,p}}{\vec{V}_p} = \sqrt{\left[1 + \left[\frac{\lambda_r}{1-a}\right]^2\right]} = \sqrt{\left[1 + \left[\frac{\lambda}{1-a}\right]^2\left[\frac{r}{R}\right]^2\right]} \tag{32}$$

Therefore, the local collection efficiency at any 2-D plane location along the blade span is:

$$\beta_{xyz} = \beta_{xy}\sqrt{\left[1 + \left[\frac{\lambda}{1-a}\right]^2 \left[\frac{r}{R}\right]^2\right]} \tag{33}$$

Thus, the local collection on a rotating blade is expressed as:

$$\beta_o = -\frac{\alpha\vec{V}_d \cdot \vec{n}}{LWC_\infty V_{a,\infty}}\sqrt{\left[1 + \left[\frac{\lambda}{1-a}\right]^2 \left[\frac{r}{R}\right]^2\right]} \tag{34}$$

These expressions will be used in the analysis of impinging droplets on the ice surface.

5.3. Formulation of Mass and Energy Conservation

A control volume at the flow stagnation location, Fig. 5.2, can be selected along the stagnation line and extended from the boundary layer to the blade's surface. It encloses a distance along the external surface and extends in the span-wise direction to analyze the mass and energy transport during an icing event. This analysis considers two ice accretion cases: one for rime ice and another for glaze ice. Heat and mass transfer predictions are obtained by solving the ice accretion and droplet runback. The processes caused by impinging droplets can be modelled as a thin liquid film on the blade surface. The film may run back, due to shear stresses created by the airflow, centrifugal forces, or gravity. The velocity of the liquid film $\vec{V}_f$ is a function of the coordinates (x, z) on the blade surface and y (normal) to the surface.

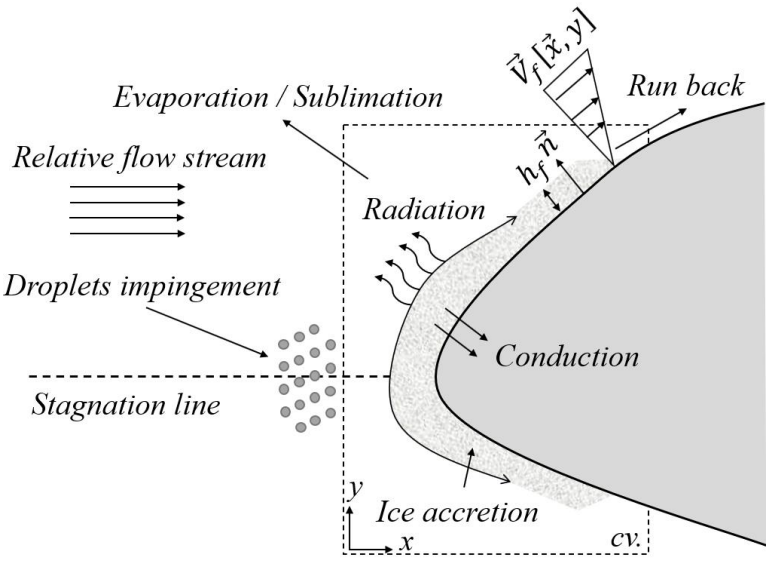

Figure 5.2. Discretization of a stagnation point control volume over a blade leading edge.

Considering a 2-D case, and assuming a linear profile for the film velocity, normal to the blade surface wall, with zero velocity imposed at the wall (no-slip condition),

$$\vec{V}_f[\vec{x},y] = \frac{y}{\mu_f}\vec{\tau}_{a,w}[\vec{x}] \tag{35}$$

where $\tau_{a,w}$ is the air shear stress at the blade surface wall, which is the main driving force for the flowing liquid film. Assuming a thin liquid film during the icing process [34], the mean film velocity across the film thickness can expressed as:

$$\bar{V}_f[\vec{x},y] = \frac{1}{h_f}\int_0^{h_f}\vec{V}_f[\vec{x},y]dy = \frac{h_f}{2\mu_f}\tau_{a,w}[\vec{x}] \tag{36}$$

where h_f is the fluid (water) film height / thickness and $\bar{V}_f$ is the average film velocity before freezing (as it runs back along the blade surface). During rime ice accretion, heat transfer or surface water expressions are not important for consideration as all impinging droplets freeze upon impact. But for glaze ice accretion, all heat transfer and surface film flow expressions are required for the analysis. Assuming there will be no water inflow along the surface because a stagnation-point control volume has been selected, the mass balance along the flow stagnation point control volume requires that:

$$\dot{M}_{film} = \dot{M}_{imp} - \dot{M}_{evap/subl} - \dot{M}_{ice} \tag{37}$$

The mass flux balance for the runback water film before freezing [34] can be expressed as:

$$\rho_f \left[\frac{\partial h_f}{\partial t} + \vec{\nabla} \cdot \left[h_f \bar{V}_f \right] \right] = \dot{M}_{imp} - \dot{M}_{evap/subl} - \dot{M}_{ice} \tag{38}$$

The three terms on the right side correspond to the total mass transfer by water droplet impingement (i.e., source for the fluid film), evaporation/sublimation, and ice accretion (i.e., freezing of the liquid film). Numerically, fluid film flow on all blade wall surfaces consists of a balance of impinging water, evaporation/ sublimation, convection and phase-change phenomena driven by the heat fluxes.

The freezing fraction is a dimensionless parameter that is defined as the ratio between ice mass and impinging water mass (i.e., $n = \frac{\dot{M}_{ice}}{\dot{M}_{imp}}$). The freezing fraction is usually less than unity (i.e., $n < 1$) during glaze ice condition. Heat flux rates contribute directly to the icing process. The mass of liquid film running back on the blade surface is controlled by the freezing fraction,

$$\dot{M}_{film} = \dot{M}_{imp}[1 - n] - \dot{M}_{evap/subl} \tag{39}$$

The total liquid water mass collected is the impingement of super-cooled water droplets in the air. The mass flux of the total impingement of water on a rotating blade can be expressed as:

$$\dot{M}_{imp} = V_{a,\infty} LWC_{\infty} \beta \tag{40}$$

The freezing process of the super-cooled droplets is instantaneous or delayed, depending on how rapidly the latent heat of fusion is released from the water. The ice mass flux is a function of freezing fraction and impinging water mass flux,

$$\dot{M}_{ice} = n V_{a,\infty} LWC_{\infty} \beta \tag{41}$$

The evaporative mass flux is typically recovered from the convective heat flux. The total mass flux and rate of water that evaporates/sublimates [35] are expressed as:

$$\dot{M}_{evap/subl} = h_g\left[\rho_{v,w} - \rho_{v,e}\right] = h_g\left[\frac{P_{v,w}}{R_v T_w} - \frac{P_{v,e}}{R_v T_e}\right] \tag{42}$$

where h_g is the gas-phase mass transfer coefficient by diffusion, $\rho_{v,w}$ is the water vapour density at the blade surface wall, and $\rho_{v,e}$ is the vapour density at the edge of the boundary layer. These densities can be calculated by the universal gas law using the pressure, temperature and gas constant R_v.

Anderson and Ruff [15, 16] predicted this evaporative mass flux using the difference in partial vapour pressure at the surface wall and the atmosphere. The gas mass transfer coefficient can be estimated using correlations. This gas-phase mass transfer coefficient, h_g, is evaluated using the analogy to the convective heat transfer coefficient h_{cv}. The relationship between the two coefficients is expressed by Ref. [36] using Schmidt, Prandtl and Lewis numbers as:

$$h_g = \frac{h_{cv}}{c_{p,a}}\left[\frac{Pr}{Sc}\right]^{\frac{2}{3}} \quad or \quad h_g = \frac{h_{cv}}{\rho_a c_{p,a}[Le]^{2/3}} \tag{43}$$

Assuming the same selected control volume to formulate the energy balance on an icing surface using the First Law of Thermodynamics,

$$\rho_f\left[\frac{\partial h_f c_{p,f}\tilde{T}_f}{\partial t} + \vec{\nabla}\cdot\left[h_f\bar{V}_f c_{p,f}\tilde{T}_f\right]\right] = \dot{E}_{imp} - \dot{E}_{evap/subl} - \dot{E}_{ice} - \dot{E}_{conv} - \dot{E}_{rad} - \dot{E}_{cond} \tag{44}$$

where the first three terms on the right side are the energy transfer from the impinging super-cooled droplets, evaporation, and ice accretion. The last three terms refer to convective, radiative and conductive heat transfer rates, respectively.

The total energy transfer of impinging droplets is the energy lost from the liquid film surface to raise the temperature of the impinging droplets to the freezing point; in addition to the energy gained by the liquid film surface from the kinetic energy of the impinging droplets striking the blade surface,

$$\dot{E}_{imp} = V_{a,\infty} LWC_{\infty} \beta \left[c_{p,f} \left[\tilde{T}_{\infty} - \tilde{T}_f \right] + \frac{\left\| \vec{V}_d \right\|^2}{2} \right] \tag{45}$$

where $\tilde{T}_{\infty}$ is the approximate stream temperature, $\tilde{T}_f$ is the equilibrium temperature at the air/ droplet/ liquid film / ice / wall interface.

The evaporative energy transfer is the product of the evaporated water mass and the latent heat of vaporization L_{evap}, due to heat lost from the liquid film surface. Similar to evaporation, the heat lost from the surface due to ice sublimation is the product of the evaporated ice mass rate and the latent heat of sublimation, both expressed as:

$$\dot{E}_{evap} = \dot{m}_{evap} L_{evap}; \qquad \dot{E}_{subl} = \dot{m}_{subl} L_{subl} \tag{46}$$

The sublimation of ice is usually negligible compared to the evaporation of liquid.

A portion of the total energy of the impingement of droplets is consumed during the freezing process. Typically, the total energy of ice accretion is the energy gained by the surface due to the release of latent heat from the super-cooled droplets added to the heat gained by the surface due to the release of sensible heat from the ice as it cools from the freezing point to the blade surface temperature,

$$\dot{E}_{ice} = \dot{m}_{ice} \left[c_{p,ice} \left[\tilde{T}_{ice} - T|_{0°\mathrm{C}} \right] - L_{fusion} \right] \tag{47}$$

where L_{fusion} is the latent heat of fusion and $\tilde{T}_{ice}$ is equilibrium temperature of ice surface and $T|_{0°\mathrm{C}}$ is the freezing temperatures (i.e., 0°C).

The airflow over the blade surface leads to convection heat transfer, which depends on the difference between the total flow stream temperature and ice film surface temperature and the convective heat transfer coefficient, expressed as

$$\dot{E}_{conv} = h_{cv} \left[\tilde{T}_f - \tilde{T}_{ice,rec} \right] \qquad \tilde{T}_{ice,rec} = T_{a,\infty} \left[1 + REC \left[\frac{\gamma - 1}{2} \right] Ma^2 \right] \tag{48}$$

where $\tilde{T}_{ice,rec}$ is the total temperature which is related to the static stream temperature $T_{a,\infty}$ of the airflow, REC is a recovery factor to address the effects of energy loss due to friction, and its value is evaluated theoretically as $REC = \sqrt{Pr}$ for laminar flow and as $REC = \sqrt[3]{Pr}$ for turbulent flow. Ma is the Mach number and γ is the specific heat ratio of air. The convective heat transfer coefficient is correlated [15, 16] for icing over a cylinder and a leading edge of airfoils as:

$$Nu_a = 1.14[Re_a]^{0.5}[Pr_a]^{0.4} \tag{49}$$

The temperature at which the air properties are obtained can be assumed as the average temperature of the air stream and blade wall surface temperature.

The energy lost from the ice film due to radiative heat transfer is expressed as:

$$\dot{E}_{rad} = \sigma\varepsilon\left[{T_\infty}^4 - {T_f}^4\right] \tag{50}$$

where σ is the Stefan-Boltzmann constant and ε is the emissivity of the ice film surface. This energy term can be negligible when there is no difference between the ice surface and ambient stream temperature.

The rate of conduction heat transfer through the accreted ice is influenced by the temperature difference between the ice film thickness at the initial icing temperature T_o and the blade wall surface T_w. The energy loss term is expressed by a conduction heat transfer coefficient h_{cd} as:

$$\dot{E}_{cond} = h_{cd}[T_o - T_w] \tag{51}$$

where h_{cd} is a function of thermal conductivity, κ_i, and thermal diffusivity, α_i, of the ice film [36]. The conduction effects are insignificant for longer icing times because after a few seconds, the ice forms quickly, generating an insulation layer over the object's surface. Thus this energy term can be neglected; however, for wet icing or de-icing simulations, this term should be included.

Several dimensionless similarity parameters can be derived from the energy balance. Tribus [38] introduced a relative heat factor b. This factor relates the energy of impingement droplets and convection energy terms,

$$b = \frac{\dot{M}_{imp} c_{p,f}}{h_{cv}} = \frac{V_{a,\infty} LWC_{\infty} \beta_o c_{p,f}}{h_{cv}} \tag{52}$$

The following parameters have been used in past literature for ice scaling on aircraft. These two parameters relate to the air and droplet energy transfer as:

$$\theta = \left[T_w - T_{a,\infty} - \frac{{V_{a,\infty}}^2}{2c_{p,a}} \right] + \frac{\dot{m}_{evap} L_{evap}}{h_{cv}} \tag{53}$$

$$\phi = \left[T|_{0°\mathrm{C}} - T_{a,\infty} - \frac{{V_{a,\infty}}^2}{2c_{p,f}} \right] \tag{54}$$

The scaling method will maintain energy terms to scale the thermodynamics of ice accretion.

5.4. Similitude Analysis and Icing Scaling Requirements

For a similitude analysis, the scaling methodology needs to simulate the blade geometry, mixed flow field, droplet trajectories, and the mass and energy transfer rates associated with the blade surface phenomena during the icing process. The dimensionless groups are used as scaling equations to scale flow variables between reference and scaled models. A summary of ice scaling methods used in past studies for aircraft icing is presented in Table 2.

Table 5.2. Comparison of past and current scaling methods.

Method	Test variables							Scaling parameters									
	V	Ω	R	T	d	LWC	t	Re	Ma	We	K	A_c	n	b	ϕ	θ	Rotational Ps.
Past scaling methods																	
ONERA [39]	C	*	*	S	S	C	C	*	*	*	M	M	M	*	*	*	*
Olsen [40, 41]	M	*	*	C	M	S	C	*	*	*	M	M	M	*	*	*	*
Anderson [13,15,18-20,22,23,25,28-30,31,45]	C	*	*	M	S	C	C	*	*	*	M	M	M	M	M	M	*
Bilanin [14, 24]	C	*	*	M	S	C	C	*	*	M	M	M	M	M	*	*	*
Kind [42-44]	C	*	*	M	S	C	C	*	*	M	M	M	*	*	*	M	*
AEDC, Ruff [16,19,20,45]	C	*	*	M	S	C	C	*	*		M	M	M	M	M	M	*
Current scaling method																	
Current study for glaze ice scaling	C	C	C	M	C	C	C	M	*	*	M	C	M	M	*	*	M

{M} To be matched between the scaled and reference models or found as matched based on results
{C} To be calculated using the scaling equations
{S} To be specified
{*} Not considered in the analysis

5.4.1. Geometrical Scaling Requirements

Blade geometry scaling requires geometric scaling conditions to be met between both models. The scaled blade geometry (including the airfoil curvature) should be identical to the reference blade geometry and other geometrical design parameters, such as the blade surface roughness, material, and tilt/twist angle. Turbine blade scaling should ensure similarity in the chord length (X), airfoil curvature thickness (Y), and span-wise length (Z). The scale factor k is defined as:

$$k = \frac{L_{c_f}}{L_{c_s}} \qquad \left[i.e., k = \frac{X_f}{X_s} = \frac{Y_f}{Y_s} = \frac{Z_f}{Z_s}\right] \tag{55}$$

The scale factor represents a ratio between the characteristic length L_c of both full-size and scaled-down geometries.

5.4.2. Flow Field Scaling Requirements

Using the Reynolds number alone is insufficient to scale the flow over similar rotating blades since equivalent rotational speeds for each similar model should be identified. The new dimensionless parameters representing the speed ratios can address this issue. Thus, similarity can be achieved in the airflow field between the reference (full size) and scaled models (smaller size). The scaling parameters in this study to scale the flow field are outlined as follows. Similitude of the air-stream flow Reynolds number is given by:

$$\left[\frac{\rho_a V_{a,\infty} L_c}{\mu_a}\right]_s = \left[\frac{\rho_a V_{a,\infty} L_c}{\mu_a}\right]_f \tag{56}$$

The newly found non-dimensional groups that represent performance speed ratios are obtained as:

$$\left[\frac{\Omega^2 R L_c}{{V_{a,\infty}}^2}\right]_s = \left[\frac{\Omega^2 R L_c}{{V_{a,\infty}}^2}\right]_f \tag{57}$$

$$\left[\frac{2\Omega L_c}{V_{a,\infty}}\right]_s = \left[\frac{2\Omega L_c}{V_{a,\infty}}\right]_f \tag{58}$$

Solving the equations and neglecting compressibility effects, these scaling equations (56), (57), and (58) can be used to scale the operating parameters such as wind speed, rotational speed, and rotational radius (i.e., distance to the axis of rotation) based on the scale factor k. When the characteristic length L_c of the geometry is replaced by the radius of the blade R, Equation (58) can be expressed as the operating TSR between models. In this study, the Strouhal number has not been used since the flow is assumed to be steady; thus, there is no change in flow oscillation frequency between small and full-scale models, leading to the same scaling conditions for flow stream

velocity. Further scaling analysis using the Strouhal number may be needed to scale unsteady flows over a vertical-axis wind turbine.

5.4.3. Droplet Trajectory and Total Impingement Scaling Requirements

Droplet scaling parameters are needed to produce geometrically coincident impingement regions and identical distributions on similar geometries. The droplet trajectory scaling requires that the total mass of the droplets reaching each part of the blade surface be similar. The trajectory analysis for the droplet momentum equation presents the significant dimensionless parameters. Maintaining these scaling parameters can sufficiently satisfy the requirements for producing similar droplet trajectories between the scaled and reference models. Similitude of the relevant dimensionless group is given by:

$$\left[\frac{C_d Re_d}{24K}\right]_s = \left[\frac{C_d Re_d}{24K}\right]_f \tag{59}$$

Equation (59) can be used to scale the droplet flow conditions (including the droplet size) based on the scale factor k. Each dimensionless parameter in the group relies on the characteristic length, directly or indirectly. Maintaining one parameter from the group such as the inertia parameter, retains the others (i.e., drag and Reynolds). Equating, the droplet diameter scaling can be done either by the Reynolds number as:

$$\left[\frac{\rho_a d\left|\vec{V}_a - \vec{V}_d\right|}{\mu_a}\right]_s = \left[\frac{\rho_a d\left|\vec{V}_a - \vec{V}_d\right|}{\mu_a}\right]_f \tag{60}$$

or by using the droplet inertia parameter as:

$$\left[\frac{\rho_d d^2 V_{a,\infty}}{\mu_a L_c}\right]_s = \left[\frac{\rho_d d^2 V_{a,\infty}}{\mu_a L_c}\right]_f \tag{61}$$

As mentioned previously, the scaling of the droplet size will ensure an equal drag coefficient over the droplet since its correlations mainly depend on the Reynolds number. Droplet trajectory scaling assures the distribution of the droplet impingement on similar bodies. For scaled ice accretions to start growing under similar conditions, the total mass flow rate of impinging droplets on the blade surface should be scaled as:

$$\left[\dot{m}_{imp}\right]_s = \frac{\left[\dot{m}_{imp}\right]_f}{k} \tag{62}$$

The amount of ice that accumulates on the blade surface depends on the amount of water in the atmosphere (i.e., LWC) and the total mass of droplets that impacts and freezes on the blade surface.

The freezing fraction is another similarity parameter that is significant for glaze ice scaling. The freezing fraction represents the rate of ice growth with time and can be expressed as:

$$\frac{d\delta_{ice}}{dt_{ice}} = \frac{n\dot{m}_{imp}}{\rho_{ice}} \tag{63}$$

where δ_{ice} is the local ice thickness, ρ_{ice} is the local ice density, and t_{ice} is the icing time. Although the local collection efficiency β_o is expected to vary with time as the ice shape changes, if both β_o and δ_{ice} are assumed to be constant during the icing process, Eq. (63) can be integrated for the icing time to obtain the local ice thickness δ_{ice} as follows,

$$\delta_{ice} = \frac{nV_{a,\infty}LWC_{\infty}\beta_o t_{ice}}{\rho_{ice}} \tag{64}$$

One approach to scale ice shape is that the local thickness of ice normalized by the characteristic model must be similar between the scaled models and reference model,

$$\left[\frac{\delta_{ice}}{L_c}\right]_s = \left[\frac{\delta_{ice}}{L_c}\right]_f \qquad \left[i.e., \ \left[\frac{\delta_{ice}}{c}\right]_s = \left[\frac{\delta_{ice}}{c}\right]_f\right] \tag{65}$$

Modifying Eq. (64) in a non-dimensional form and including the total collection efficiency leads to a scaling parameter called the ice accumulation parameter A_c, defined as:

$$A_c = \frac{nV_{a,\infty}LWC_{\infty}\beta t_{ice}}{\rho_{ice}L_c} \tag{66}$$

Therefore, the ice accumulation parameters must be maintained between the scaled and reference models to ensure successful scaling of the local ice thicknesses everywhere on the blade surface.

$$\left[\frac{nV_{a,\infty}LWC_{\infty}\beta t_{ice}}{\rho_{ice}L_c}\right]_s = \left[\frac{nV_{a,\infty}LWC_{\infty}\beta t_{ice}}{\rho_{ice}L_c}\right]_f \tag{67}$$

Equation (67) can be used to scale icing conditions (i.e., such as LWC or icing time) using the scale factor k. This analysis assumes that there is no significant change in total collection efficiency during the icing process.

5.4.4. Thermodynamic Scaling Requirements

Thermodynamic considerations are required for scaling the accreted ice characteristics in terms of type, density and surface roughness characteristics for similar geometries. The temperature affects the heat transfer rates during the icing process. Many thermodynamic scaling parameters have been proposed in past icing scaling studies without highlighting their physical significance. The relative heat factor is determined as:

$$\left[\frac{V_{a,\infty}LWC_{\infty}\beta c_{p,f}}{h_{cv}}\right]_s = \left[\frac{V_{a,\infty}LWC_{\infty}\beta c_{p,f}}{h_{cv}}\right]_f \tag{68}$$

where h_{cv} is estimated with Equation (49). If the scaling relations are obtained for the flow and droplet trajectories, then similarity in the convective heat fluxes will be assured. Previous studies used the droplet's energy transfer potential and similarity parameters for surface temperature and stream temperature scaling. In this study, these requirements can be satisfied by maintaining temperature conditions over the scaled blade geometries, with no heating applied to the surfaces during the icing process.

5.5. Scaling Methodology

The scaling method in this section starts with a flow analysis, determination of scaling parameters and testing of calculated scaled conditions on scaled blade geometries using FENSAP ICE. A visualization of the scaling methodology is presented in Figure 5.3:

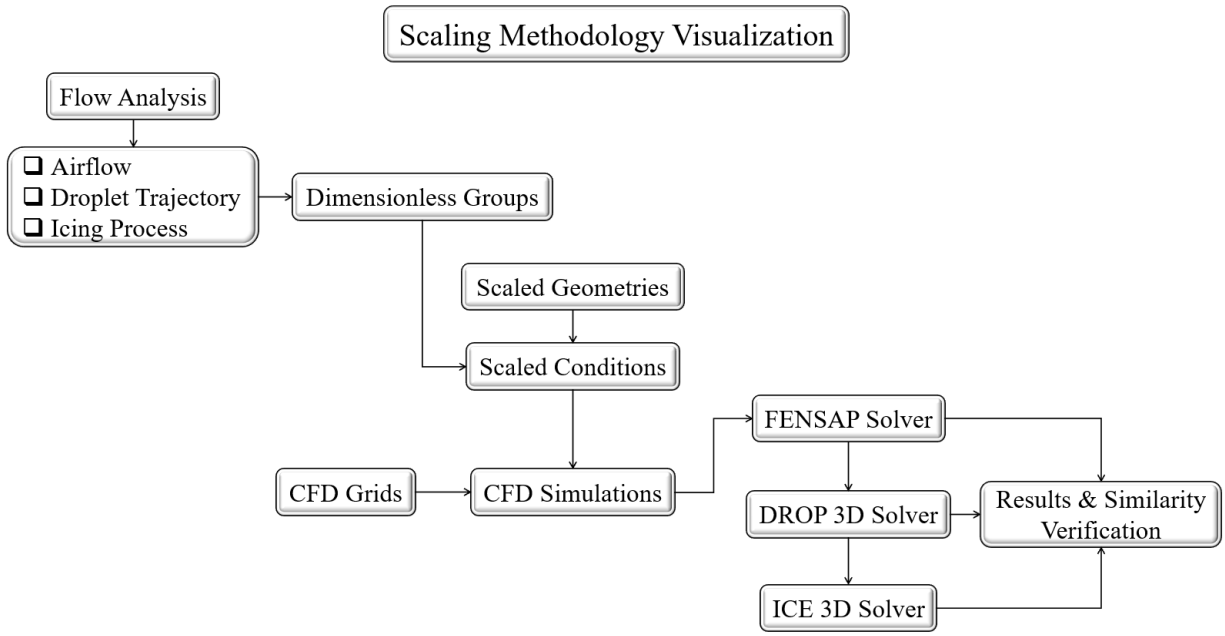

Figure 5.3. Visualization of the scaling process.

5.5.1. Scaled Turbine Blade Models

This section investigates the flow field scaling around similar rotating wind turbine blades with scaled sizes and radii. The selected geometry is an entire turbine blade model. The blade geometry scaling is achieved in all three spatial dimensions using the scaling factor k. Four NACA non-symmetrical airfoils are used for the blade design in this study. The airfoils vary in thickness along the blade span (i.e., NACA 4426 at the root to NACA 4415 at the tip). The flow variables for each case are obtained based on the previous similitude analysis and scaling equations. As shown in Fig. 5.4, five similar blade sizes with scaled radii at scaled distances from their center of gravity to their

axis of rotation are numerically investigated. The rotational direction is a counterclockwise direction for all rotating blades.

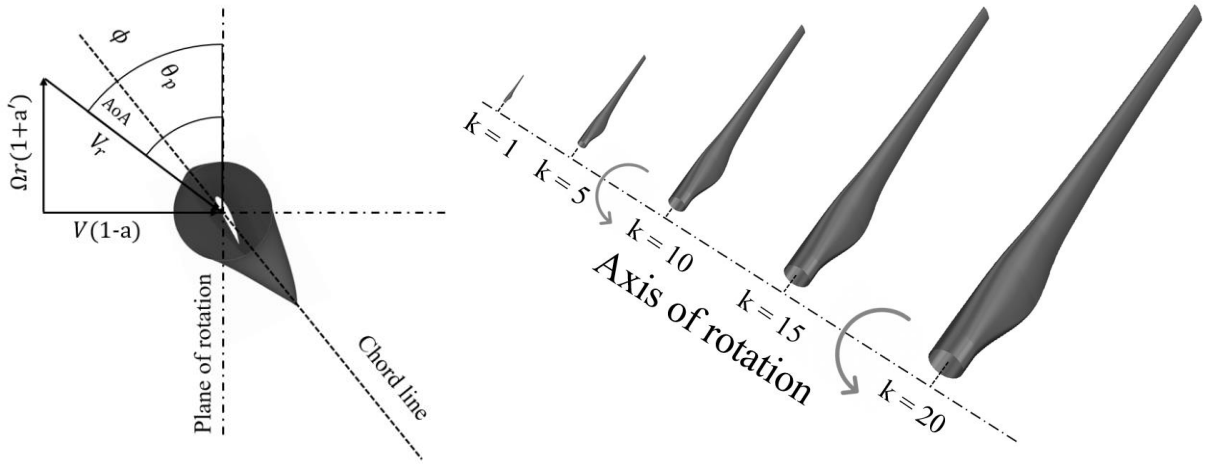

Figure 5.4. Discretization of the rotating scaled blade sections and aerodynamic orientation.

An effective flow distribution around a rotating turbine blade requires careful design considerations. The Blade Element Momentum (BEM) theory [46] is applied in the design process of the entire blade geometry to obtain the chord length variation along the blade model span (i.e., at a TSR of 7). A scale of unity (i.e., k = 1) represents the smallest blade model size. The blade geometry is scaled up to 20 times as large (i.e., k = 20). Values for each blade dimension and area are shown in Table 5.3. The impingement area is the wetted surface area (i.e., airfoil profile perimeter by span length) where the droplets impact and the reference area is the wing surface area (i.e., chord by span length).

Table 5.3. Scaled blade geometry characteristics

Parameter	**Scale factor, k**				
	1	5	10	15	20
Average chord length (m)	0.062	0.31	0.62	0.93	1.24
Average airfoil perimeter (m)	0.15	0.76	1.53	2.29	3.1
Blade radius (m)	1	5	10	15	20
Reference area (m^2)	0.062	1.55	6.2	13.95	24.8
Area impingement (m^2)	0.153	3.825	15.3	34.42	61.2

5.5.2. Computational Mesh and Discretization

This numerical study used ANSYS FENSAP ICE. Each case is simulated by steady-state simulations for the flow field for a rotating blade in the relative frame of reference. A CFD hybrid mesh consisting of structured and unstructured domains is created for each blade model to compute the flow field solution and predict ice accretion characteristics. CFD grid boundary conditions include a no-slip wall (i.e., entire blade surface), inlet, outlet, and slip outer wall boundary (see Fig. 5). High-resolution hexahedral mesh elements with a growth rate of 1.15 are created for each blade model surface (see Fig. 5). A corresponding y-value of 1 with a first layer below 10^{-4} is computed based on the applied flow conditions to ensure that the CFD domain around each blade surface is appropriately sized for an accurate simulation.

A Spalart-Allmaras turbulence model is used for modelling of the turbulent flow around the blade. It can resolve the entire flow field down to the blade wall. Successful convergence was achieved for air and droplet flow field residuals. The CFD domain spacing around each blade surface is sized appropriately for an accurate simulation. A convergence criterion of 10^{-5} is used for all simulations. A mesh independence study was performed, using six different grid sizes, ranging from 0.8 to 4.2 million elements. The residuals had not converged for a mesh of 0.8 million elements. No significant changes in the results in terms of velocity contours, pressure distributions and predicted ice shapes were predicted for meshes larger than 2.64 million elements. Each blade model in this study uses a CFD grid of approximately 3.35 million elements (Fig. 5.5).

Figure 5.5. Discretization of the CFD grid boundary conditions, Grid sectional view and blade grid surface.

5.5.3. Test Conditions

The flow field solution, droplet flow solution, and glaze ice accretion characteristics were obtained to analyze the scaling effects. This study maintains several parameters constant during the tests, including atmospheric pressure, temperature, blade surface roughness, tip speed ratio, and Reynolds number. Other parameters are scaled using the similarity relations based on the scale factor k, including blade geometry, flow stream velocity, rotational speed, rotational radius, droplet size, LWC and icing time. Flow, droplet, and ice accretion parameters are investigated at a temperature of -4 °C, where glaze ice is expected [10].

The droplet distribution in the mixed flow is modelled as monodisperse droplet formation at a selected droplet size, which is available in the droplet solver. Since this droplet model is not computationally intensive compared to other equations in the droplet solver, in this model, the solution is obtained for one specified droplet size. In other models, such as Lang-D and Lang-C distributions, consisting of 4 to 6 different droplet sizes, the solution is averaged after each droplet size solution is computed. The ice surface roughness is modelled using a sand-grain beading model.

This study uses a constant ice density of 917 kg/m^3. The test conditions are summarized in Table 5.4.

Table 5.4. Test conditions for the scaling method

Parameter	Test conditions	Scale factor, k				
		1	5	10	15	20
Flow stream temperature (°C)	Maintained	-4				
Blade surface temperature (°C)	Maintained	0				
Stream velocity (m/s)	Scaled	25	5	2.5	1.67	1.25
Rotational velocity (rpm)	Scaled	1671.2	66.9	16.8	7.5	4.1
Rotational radius (m)	Scaled	1	5	10	15	20
TSR	Maintained	7				
Stream LWC (g/m^3)	Scaled	0.1	0.5	1	1.5	2
MVD (μm)	Scaled	4	20	40	60	80
Icing time (hrs)	Scaled	0.125	0.625	1.25	1.875	2.5

In this study, a large blade operating at a TSR of 7 is selected. The critical icing occurrence is assumed to occur at lower speed operation. The scaled conditions listed in Table 4 are calculated to maintain the dimensionless groups constant between all scales. The corresponding relations to the scale factor are given as follows:

$$\left[V_{a,\infty}\right]_s = k\left[V_{a,\infty}\right]_f,\ [R]_s = \frac{[R]_f}{k},\ [\Omega]_s = k^2[\Omega]_f,\ [d]_s = \frac{[d]_f}{k},\ [LWC]_s = \frac{[LWC]_f}{k},\ [t_{ice}]_s = \frac{[t_{ice}]_f}{k} \tag{69}$$

The conditions applied to the smallest blade can be used for wind tunnel testing to represent large blade operating conditions. The blade models are similar in geometry but not real-world speed operating conditions.

All scaling parameters in this study as input conditions for the flow field and glaze ice conditions scaling are presented in Table 5.5. As shown in Table 5.5, maintaining these dimensionless groups leads to relations to scale flow variables between scaled models. For verification of results, a

summary of the previously shown parameters, including local collection efficiencies and normalized ice thickness along all blade sizes and comparisons for other output parameters, including scaled masses, freezing fractions and energy terms, are shown in Table 5.5. Results show that for scaled flow conditions, equal freezing fractions, normalized local ice thicknesses, similar scaled ice accretion shapes, and scaled energy quantities, are obtained.

Table 5.5. Dimensionless scaling parameters

Inputs								
Scale factor	Re_a	Rotational Parameters		Re_d	C_d	K	A_c	b
		$\left[\frac{\Omega^2 R L_c}{{V_{a,\infty}}^2}\right]$	$\left[\frac{2\Omega L_c}{V_{a,\infty}}\right]$					
1	1.24×10^5	0.07	0.12	8.04	4.86	0.024	19.88	M
5	1.24×10^5	0.07	0.12	8.04	4.86	0.024	19.88	M
10	1.24×10^5	0.07	0.12	8.04	4.86	0.024	19.88	M
15	1.24×10^5	0.07	0.12	8.04	4.86	0.024	19.88	M
20	1.24×10^5	0.07	0.12	8.04	4.86	0.024	19.88	M

Outputs										
Scale factor	$\beta_o\|_{\frac{r}{R}}$	$\frac{\delta_{ice}}{c}\Big\|_{\frac{r}{R}}$	m_{evap} (kg)	m_{imp} (kg)	m_{ice} (kg)	n	E_{evap} (kJ)	E_{imp} (kJ)	E_{ice} (kJ)	E_{ice} (kJ)
1	M	M	0.0001	0.0072	0.0066	0.925	0.41	0.09	1.57	1.05
5	M	M	0.043	0.932	0.888	0.952	108.8	15.6	304.1	179.5
10	M	M	0.35	7.462	7.082	0.949	894.6	125.8	2424.1	1403.5
15	M	M	1.20	25.18	23.82	0.945	3021.9	425.3	8154.5	4707.2
20	M	M	2.86	59.69	56.20	0.941	7173.8	1008.6	19237.3	11054.8

5.6. Results and Discussion

Airflow and droplet solutions are obtained numerically using FENSAP and DROP 3D solvers, respectively. Velocity magnitudes of air and droplets into the domain over each blade surface are computed. Air and droplet velocity contours are presented in Figs. 5.6 for each blade size from the root to the tip (i.e. 0.2, 0.4, 0.6, 0.8, 1 r/R). Higher velocity magnitudes can be found over small-size blades compared to the large blades, especially at sections near the blade tip. Droplet velocity

magnitudes are slightly higher than air velocity due to the different flow inertial forces. Considering the air and droplet motion in the flow stream, the drag and buoyancy forces will be the same for both, but the gravitational forces will be larger for the heavier object. Thus, droplets will move faster.

Results indicate close similarity in the velocity contours for varied full blade sizes from root to tip sections at matched flow field dimensionless groups (i.e., flow stream Reynolds number and two performance speed ratio terms). Also, the results indicate close similarity in the droplet field for varied full blade sizes from root to tip sections at constant droplet trajectory scaling parameters, including the droplet Reynolds number, inertia parameter, and droplet drag coefficient.

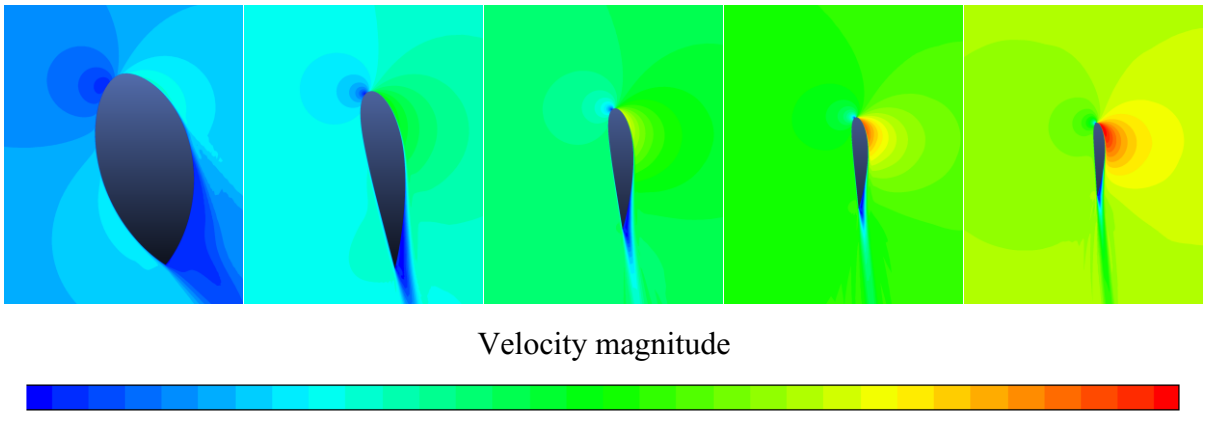

(a) k = 1, 0.2 r/R to 1 r/R

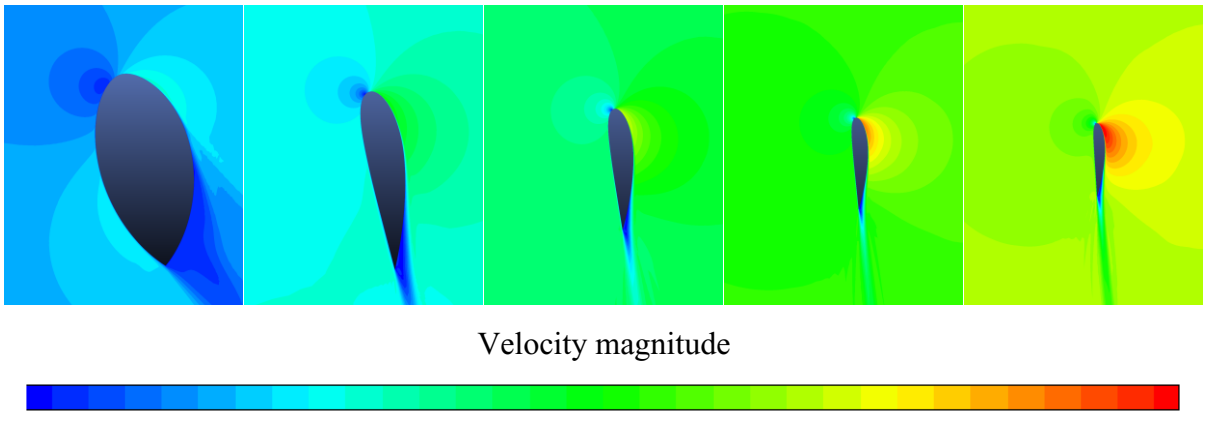

(b) k = 5, 0.2 r/R to 1 r/R

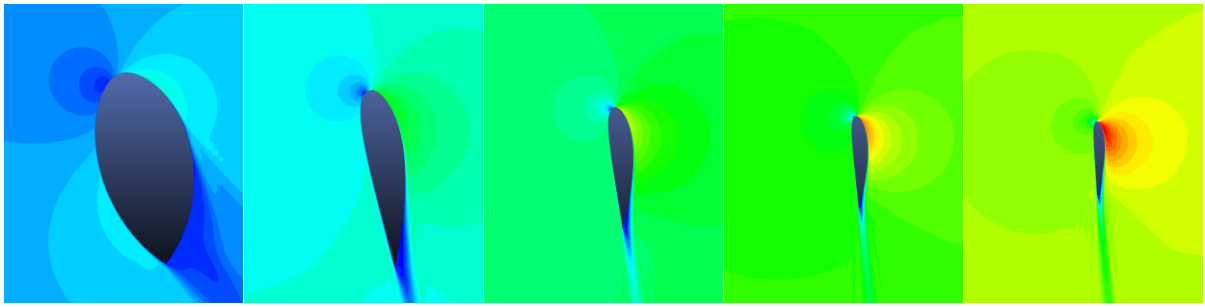

Velocity magnitude

0 V_a = 26.1 m/s, V_d = 28.2 m/s

(c) k = 10, 0.2 r/R to 1 r/R

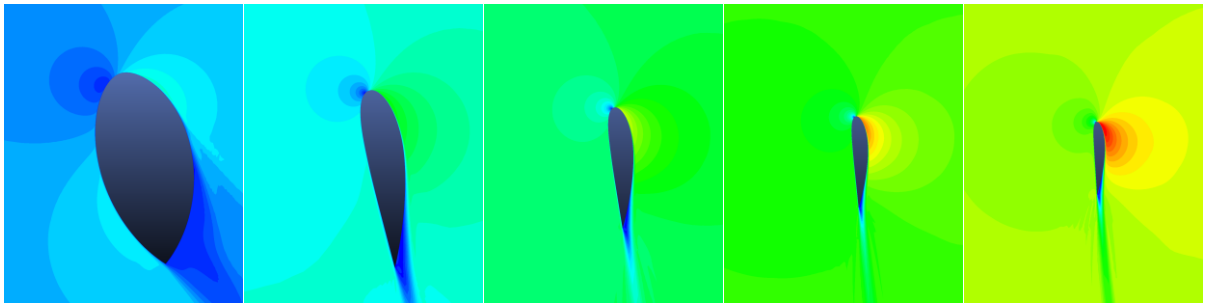

Velocity magnitude

0 V_a = 17.4 m/s, V_d = 18.7 m/s

(d) k = 15, 0.2 r/R to 1 r/R

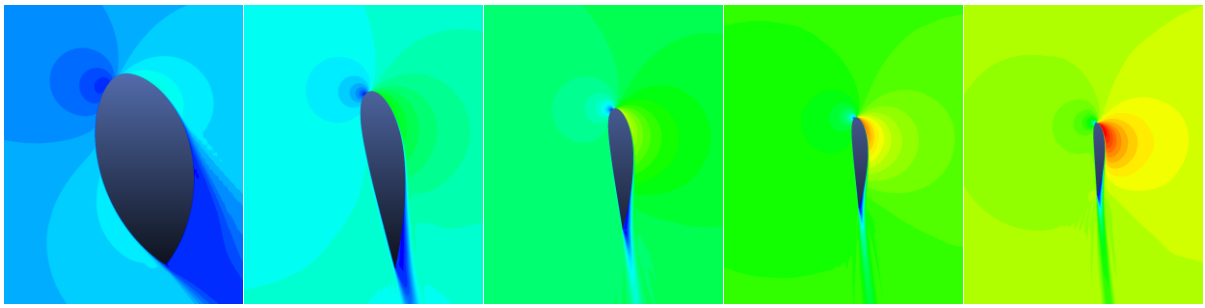

Velocity magnitude

0 V_a = 13.1 m/s, V_d = 14.1 m/s

(e) k = 20, 0.2 r/R to 1 r/R

Figure 5.6. Air velocity contours along blade span for different blade model scale factors.

As illustrated in Figs. 5.7a and 5.7b, pressure distributions along similar blades are compared for nearby root and tip sections (i.e., 0.4 and 1 r/R). The pressure coefficient profile mainly depends on the flow angle of attack. Since flow angle and blade twist vary along the blade span, the results show varied pressure distributions over different sections along the span. Results show similar normalized local pressure distributions for similar locations for scaled blade sizes at scaled flow conditions. This suggests successful flow field scaling. Average pressure coefficient values are found quantitatively identical at the same locations for all blade model sizes.

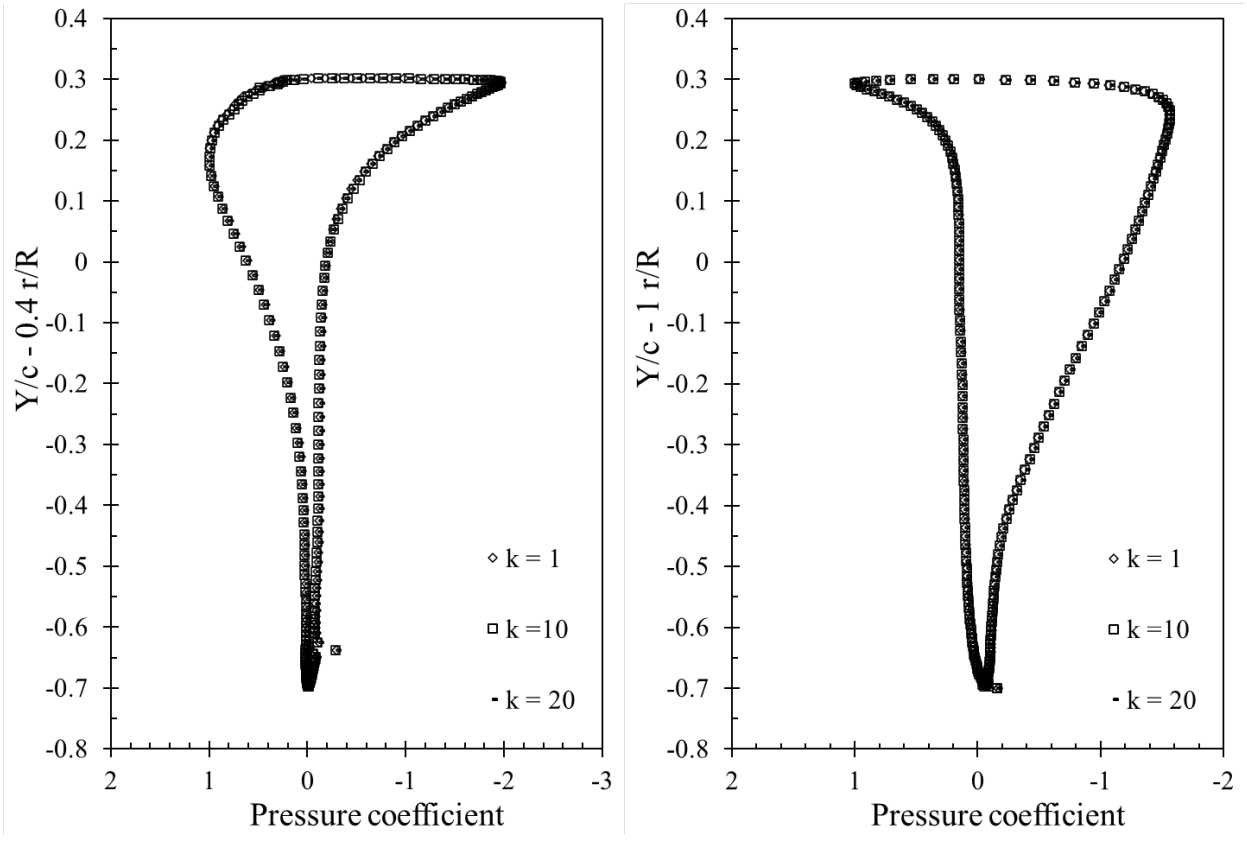

(a) (b)

Figure 5.7. Pressure coefficient along blade span for different scale factors (a) 0.4 r/R (b) 1 r/R.

The local liquid water volume fractions over the entire domain and around the blade surface are computed using the DROP 3D solver. As shown in Fig. 5.8, droplet LWC contours for each blade size from the root to the tip are similar at scaled droplet flow conditions. Results indicate that at the stagnation region on the blade surface, which extends along the span, higher values of LWC exist. Results show that the droplet flow is usually separated at the leading edge with only water droplets at the first 25% of the chord length, causing a region of no droplets up to the trailing edge.

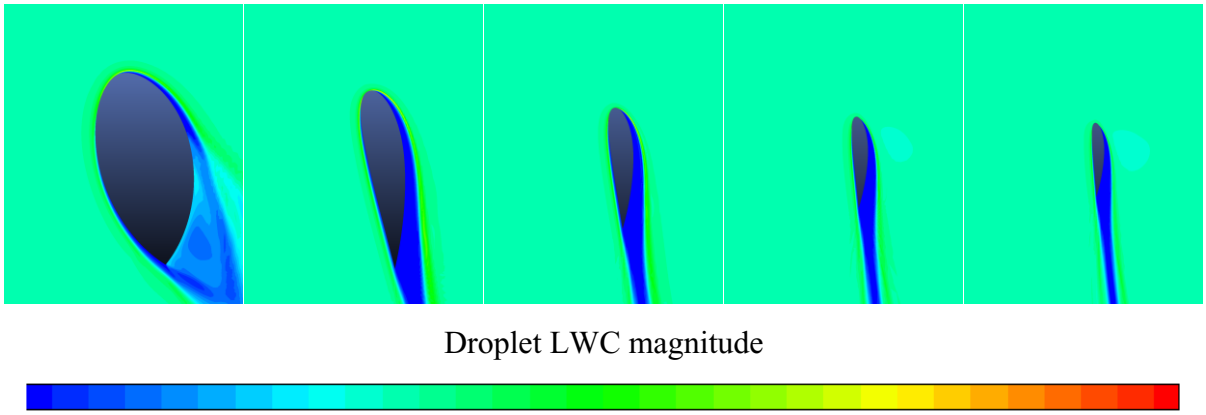

(a) k=1, 0.2 r/R to 1 r/R

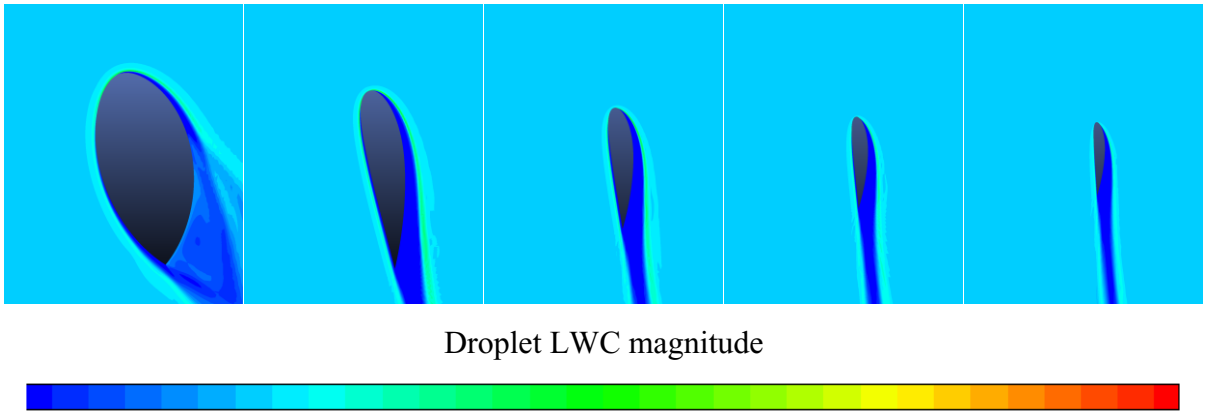

(b) k=5, 0.2 r/R to 1 r/R

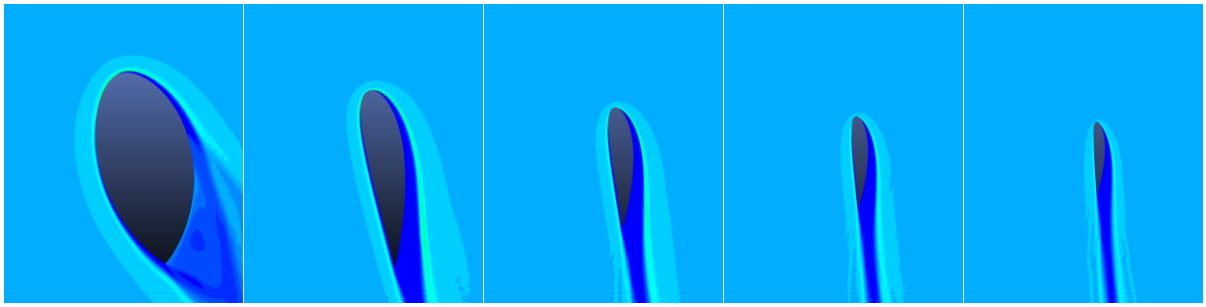

Droplet LWC magnitude

0 5.523 g/m^3

(c) k=10 0.2 r/R to 1 r/R

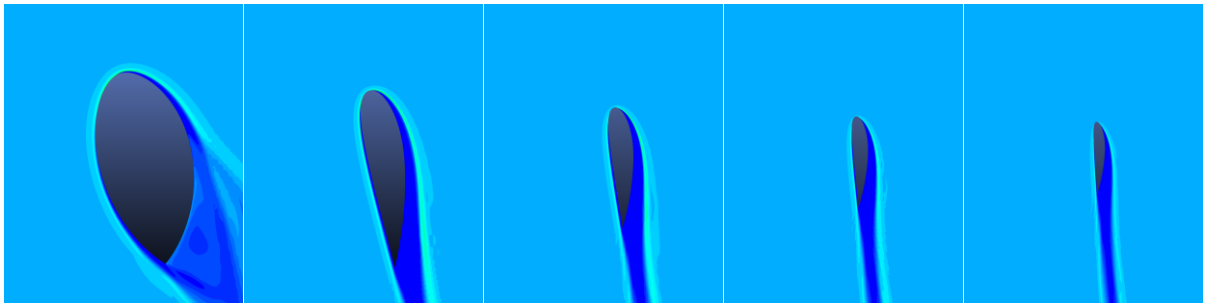

Droplet LWC magnitude

0 8.768 g/m^3

(d) k=15, 0.2 r/R to 1 r/R

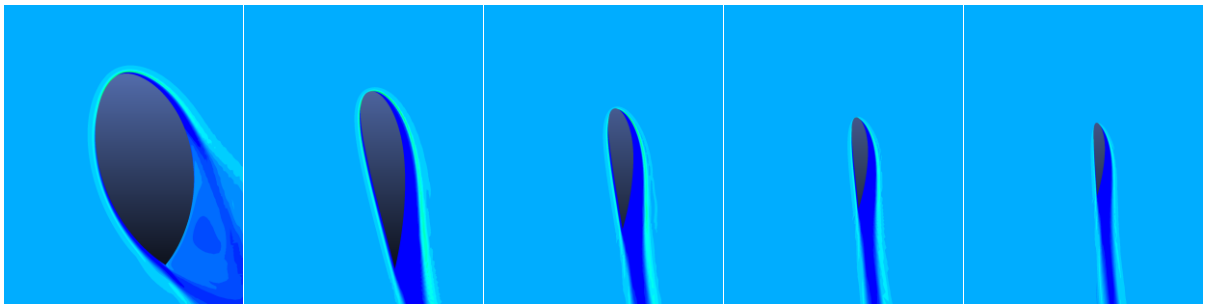

Droplet LWC magnitude

0 11.933 g/m^3

(e) k=20, 0.2 r/R to 1 r/R

Figure 5.8. Droplet LWC contours along blade span for different blade model scale factors.

The droplet concentrations and separation at the leading edge depend on the flow angle of attack and blade sectional twist. As shown in Figs. 5.9, scaled droplet LWC magnitudes are plotted along the horizontal for each blade size from the root to the tip. Results indicate similar distributions of scaled LWC magnitudes around all blade sizes at different sections along the blade span. Results show high LWC values at the stagnation location, with more droplet distribution area at sections closer to the blade tip. High LWCs significantly impact droplet collections and result in ice formation at the associated locations, especially at the stagnation location.

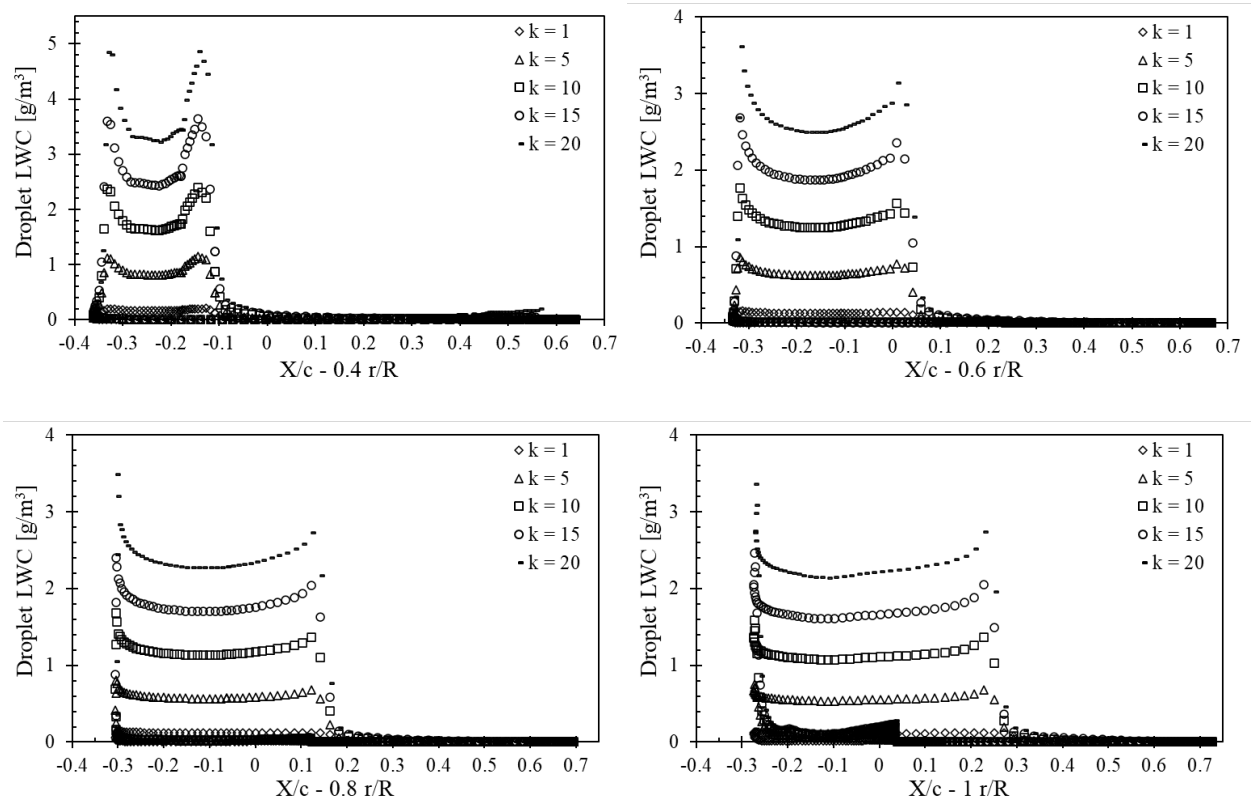

Figure 5.9. Droplet LWC distribution for different scale factors along x- direction and blade span.

Droplet collection efficiencies are also computed numerically using the DROP 3D solver. 3D local droplet collection efficiencies are obtained for each blade size at different sections along span-wise lengths. All 2D local collection efficiencies at various locations of interest on the blade span are obtained using the analysis presented in the earlier section for comparison purposes for each

blade size from the root to the tip. The 2D local droplet efficiencies typically range from 0 to 1 and vary along the blade span, where higher values can only exist at the flow stagnation point along with blade span.

Results in Fig. 5.10 show the distribution of the 2D local collection efficiency along the horizontal direction and can be found at the leading-edge where most droplets collide with the blade surface. Most droplets impinge up to 15% of the blade chord-wise direction at the leading edge. Results indicate close similarity in the collection efficiency profiles for all scaled blade sizes at scaled droplet flow conditions at the same locations of interest on blade span.

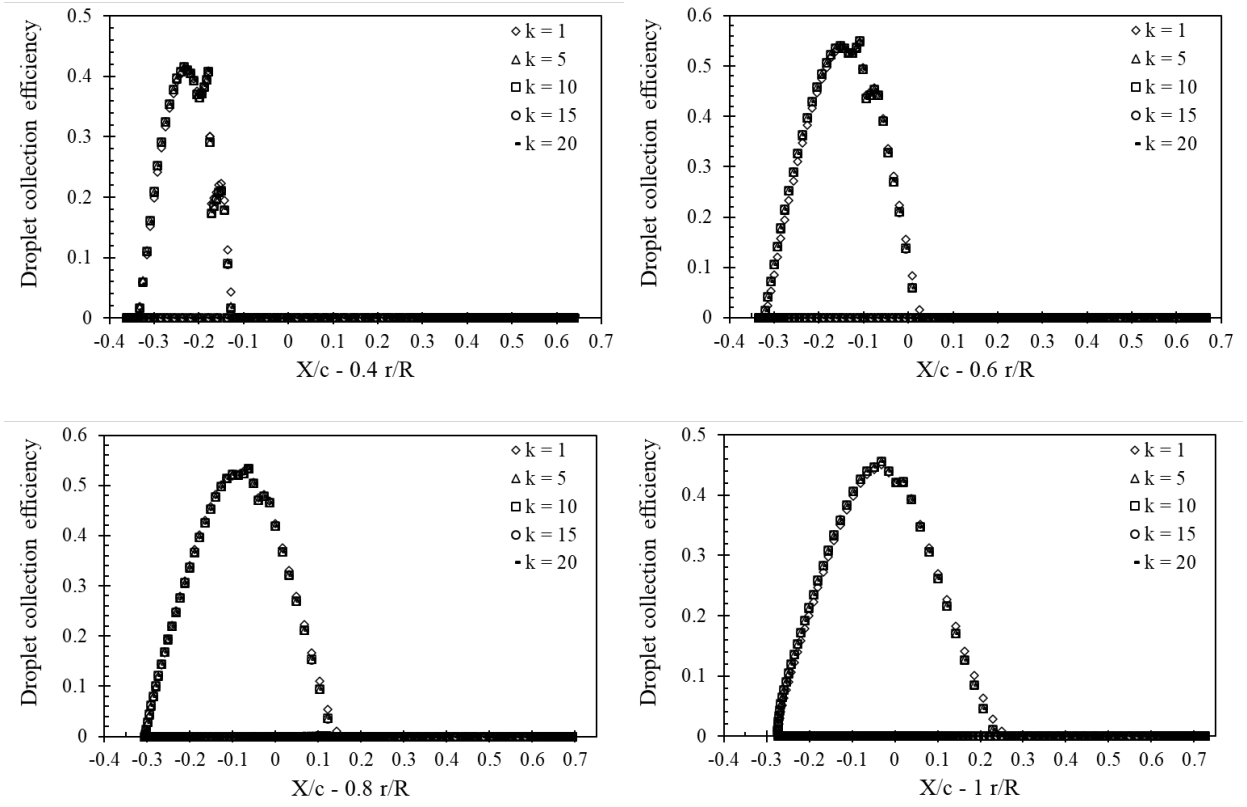

Figure 5.10. Droplet collection efficiency for different scale factors along x- direction and blade span.

The ICE3D solver computes ice thickness distributions and predicts accreted ice shapes. Ice thicknesses are plotted along the horizontal (see Figs. 5.11) for comparison purposes for each blade size from the root to the tip. As shown in Figs. 5.11, all scaled ice accretions occur at the blade's leading edge up to 15% of the chord-wise direction. Higher values of ice thicknesses accumulate at a location near the flow stagnation point. It can be noticed that ice thickness increases in magnitude and area coverage at sections far from the blade root and closer to the blade tip due to the decreased chord length, blade thickness (i.e., cross-sectional area) and twist of blade sections. Results indicate that all blade sizes have scaled ice thicknesses at scaled icing conditions and similar locations of interest along the span-wise length.

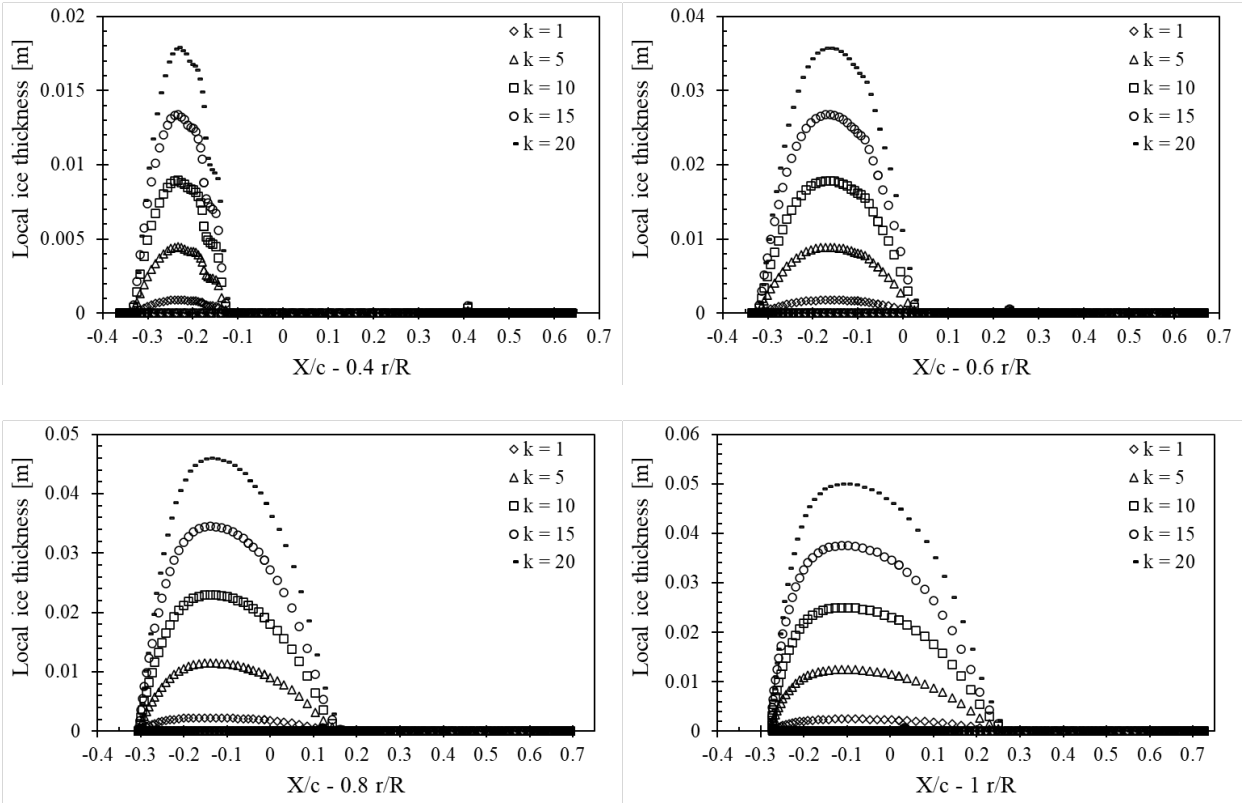

Figure 5.11. Ice thickness distribution for different scale factors along x- direction and blade span.

Local ice thickness values are non-dimensionalized for comparison purposes. Plots along the horizontal are presented in Figs. 5.12. Results again show close similarity in the ice thickness distribution for all blade sizes at scaled icing conditions and similar locations of interest along the span-wise length.

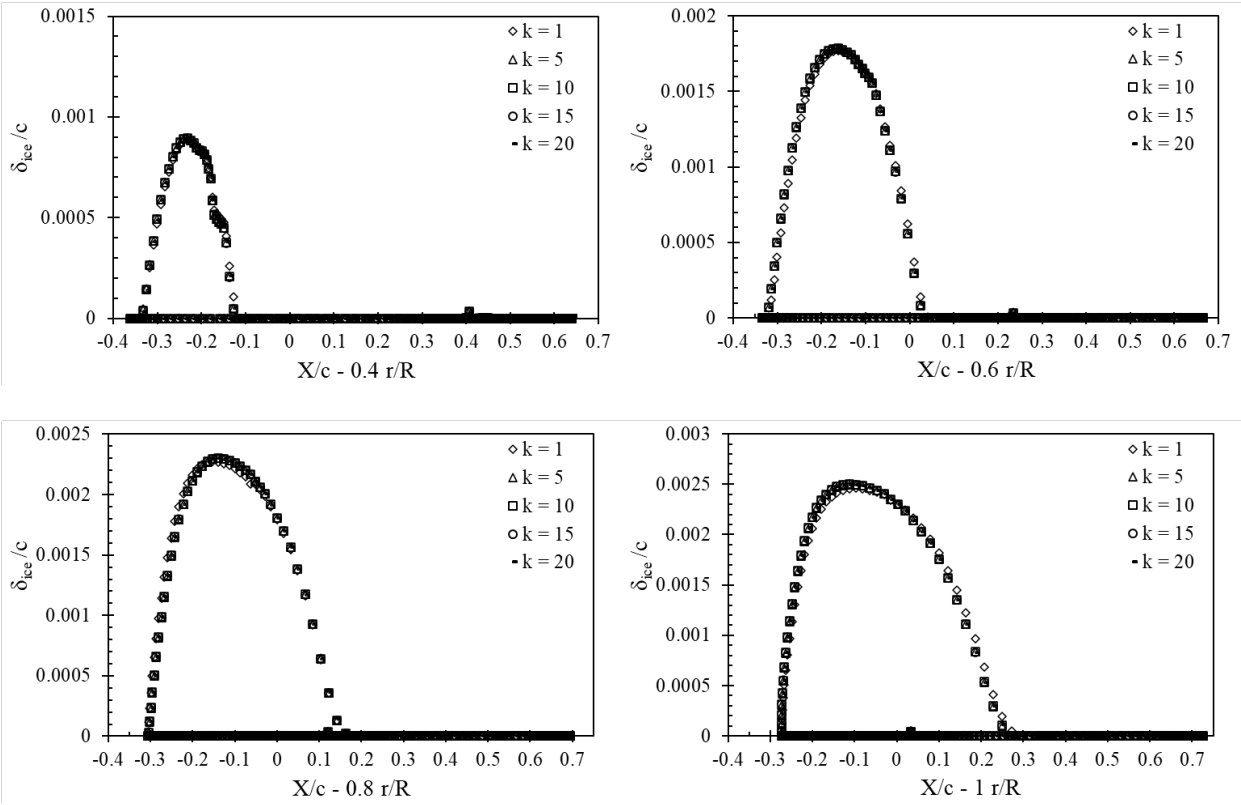

Figure 5.12. Normalized local ice thickness for different scale factors along x- direction and blade span.

2D ice shapes are predicted for each blade size at various locations along the span and presented in a non-dimensional form for comparison purposes. In Fig. 5.13, results show that the scaling methodology to predict scaled flow conditions allows predictions of closely similar ice shapes for glaze ice conditions between all scaled blade sizes and scaled icing conditions.

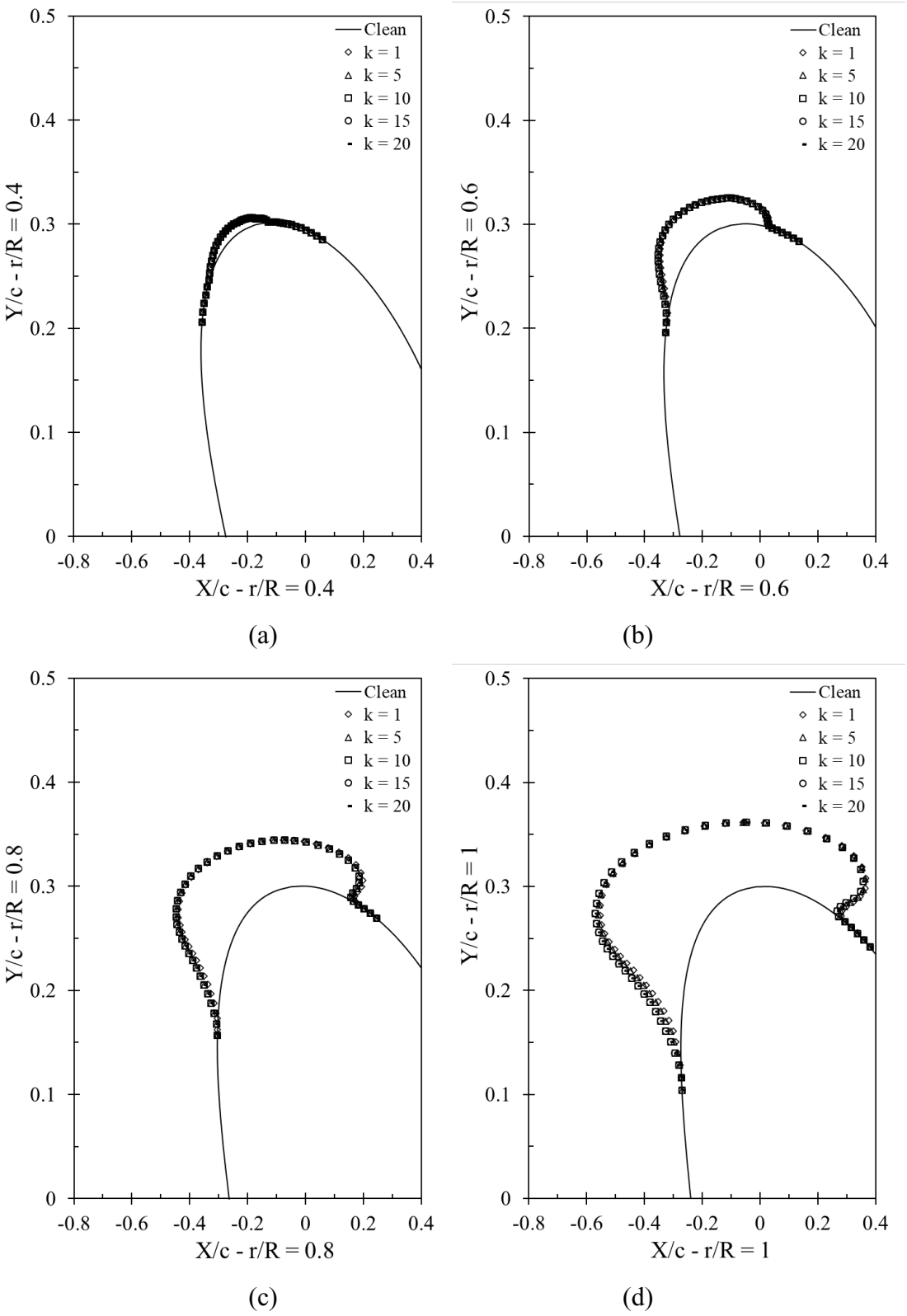

Figure 5.13. Predicted ice shapes along the blade span for different model scale factors: (a) 0.4 r/R (b) 0.6 r/R (c) 0.8 r/R (d) 1 r/R.

Despite the limited data for ice scaling on a rotating blade, further analysis aims to verify the current scaling method for glaze ice accretions on wind turbine blades. Experimental data [17, 47] for glaze ice scaling are compared with the current scaling predictions. Scaling conditions for the NREL VI rotor are predicted by using an Adverse Environment Rotor Test Stand (AERTS) in a wind tunnel (WT), Case 24 [17, 47]; scaled test conditions are examined. A turbine blade section is created for an NREL S809 airfoil, and a CFD grid is constructed for numerical simulations. The conditions are scaled based on the methodology of this study. The conditions are presented in Table 5.6.

Table 5.6. Scaling test conditions for NREL VI rotor

Test variables	**NREL VI rotor Scaling conditions**	**AERTS Case 24 Test conditions**	**Current glaze ice scaling method**
Radial location (r/R)	0.95		
Chord length (m)	0.3762	0.2667	0.1881
Flow stream temperature (°C)	-9	-9	-9
Stream velocity (m/s)	36.1	43	72.2
Rotational velocity (rpm)	72	300	288
Rotational radius (m)	4.778	1.016	2.375
LWC (g/m^3)	0.28	0.3	0.14
MVD (μm)	26.6	20	13.3
Icing time (min)	21.8	12	10.9

As illustrated in Fig. 5.14, experimentally obtained non-dimensional glaze ice distributions on the NREL S809 airfoil are compared with FENSAP ICE prediction at scaled conditions. The results show good agreement with experimental predictions.

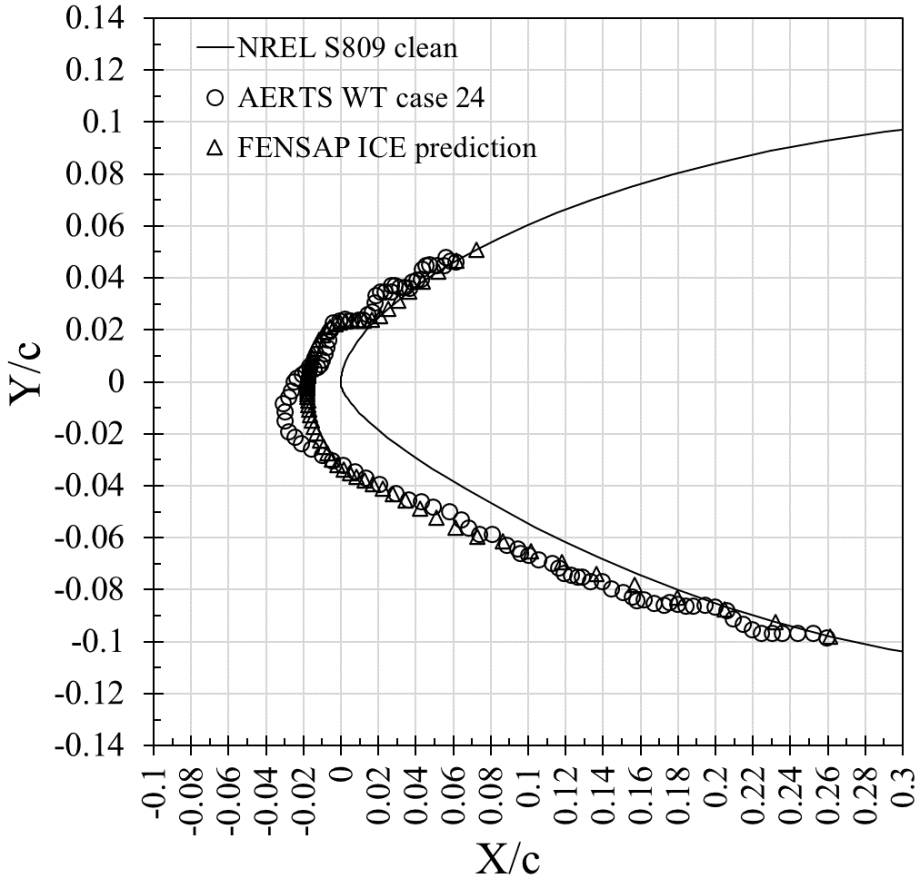

Figure 5.14. Comparison of experimental and numerical results of glaze ice accretion on a rotating NREL S809 airfoil.

Results show scaled ice mass and energy terms at different conditions with remarkable similarities in their flow behaviour, pressure distribution, droplet collection and ice shapes. This confirms the scaling methodology for scaling of multiphase flow around similar rotating blades. Results indicate a successful glaze ice scaling in terms of thickness, shape and mass between all blade sizes and each location along the blade span.

5.7. Conclusions

This study presented a scaling analysis of ice accretion on a rotating wind turbine blade. The study developed a formulation of the scaling parameters for the flow field, droplet trajectory and

ice accretion over a rotating blade, and outlined the mass and energy transfer processes during rime and glaze ice conditions. The study extended past scaling formulations for aircraft icing (i.e., flow over a fixed wing) to account for the rotation of a wind turbine blade. The analysis considered the significant scaling dimensionless groups for glaze ice conditions on a rotating blade, including the Reynolds number, two new speed ratio groups for the rotational forces, droplet inertia, drag on the droplet, ice accumulation parameter and relative heat factor. These dimensionless groups were used to obtain scaling relations that can scale flow conditions between similarly scaled geometries. Scaled variables in this study include the flow stream velocity, blade rotational speed, blade radius, droplet size, LWC, and icing time.

Glaze ice conditions were investigated numerically using FENSAP ICE software. An entire blade model was designed using BEM theory at a TSR of 7 and scaled up to 20 times using a scale factor. The test conditions for each case of each blade size were calculated using the scaling relations. The scaling method led to nearly exact air and droplet flow fields, droplet collection, and ice characteristics at scaled flow conditions for all blade sizes at each location on the span-wise length. Scaled ice characteristics, including thickness, shape, and mass, are predicted for larger blade models. Numerical results indicate that ice accretion could be intense at the blade's leading edge and along the blade span, especially at locations far from the blade root and closer to the blade tip. The results in this study provide valuable new insights for scaling of flow over a rotating blade and prediction of glaze ice accretion on a large wind turbine blade based on smaller blade models tested in laboratory conditions. Further research is recommended to examine the applicability and limits of these scaling parameters through experimental studies.

References

[1] Switchenko, D., Habashi, W., Reid, T., Ozcer, I., & Baruzzi, G. (2014). FENSAP-ice simulation of complex wind turbine icing events, and comparison to observed performance data. 32nd ASME Wind Energy Symposium. https://doi.org/10.2514/6.2014-1399

[2] Pedersen, M. C., & Yin, C. (2014). Preliminary modelling study of ice accretion on wind turbines. Energy Procedia, 61, 258–261. https://doi.org/10.1016/j.egypro.2014.11.1102

[3] Kraj, A. G., & Bibeau, E. L. (2010). Measurement method and results of ice adhesion force on the curved surface of a wind turbine blade. Renewable Energy, 35(4), 741–746. https://doi.org/10.1016/j.renene.2009.08.030

[4] Tsao, J.-C. (2016). Additional results of glaze icing scaling in SLD conditions. 8th AIAA Atmospheric and Space Environments Conference. https://doi.org/10.2514/6.2016-3278

[5] BARTLETT, C. (1988). Icing scaling considerations for aircraft engine testing. 26th Aerospace Sciences Meeting. https://doi.org/10.2514/6.1988-202

[6] Reid, T., Baruzzi, G., Ozcer, I., Switchenko, D., & Habashi, W. (2013). FENSAP-ice simulation of icing on wind turbine blades, part 1: Performance degradation. 51st AIAA Aerospace Sciences Meeting Including the New Horizons Forum and Aerospace Exposition. https://doi.org/10.2514/6.2013-750

[7] Virk, M. S., Homola, M. C., & Nicklasson, P. J. (2010). Effect of rime ice accretion on aerodynamic characteristics of wind turbine blade profiles. Wind Engineering, 34(2), 207–218. https://doi.org/10.1260/0309-524x.34.2.207

[8] Ibrahim, G.M., Pope, K., & Muzychka, Y.S. (2018). Effects of blade design on ice accretion for horizontal axis wind turbines. Journal of Wind Engineering and Industrial Aerodynamics 173, 39-52. https://doi.org/10.1016/j.jweia.2017.11.024

[9] Barber, S., Wang, Y., Jafari, S., Chokani, N., & Abhari, R. S. (2011). The impact of ice formation on wind turbine performance and aerodynamics. Journal of Solar Energy Engineering, 133(1). https://doi.org/10.1115/1.4003187

[10] Ibrahim, G. M., Pope, K., & Muzychka, Y. S. (2018). Transient atmospheric ice accretion on wind turbine blades. Wind Engineering, 42(6), https://doi.org/10.1177/0309524x18780380

[11] Fortin, G., & Perron, J. (2009). Wind turbine icing and de-icing. 47th AIAA Aerospace Sciences Meeting Including The New Horizons Forum and Aerospace Exposition. https://doi.org/10.2514/6.2009-274

[12] Battisti, L. (2015). Wind turbines in cold climates. Green Energy and Technology. https://doi.org/10.1007/978-3-319-05191-8

[13] Anderson, D., & Feo, A. (2002). Ice-accretion scaling using water-film thickness parameters. 40th AIAA Aerospace Sciences Meeting & Exhibit. https://doi.org/10.2514/6.2002-522

[14] Bilanin, A. (1988). Proposed modifications to ice accretion/icing scaling theory. 26th Aerospace Sciences Meeting. https://doi.org/10.2514/6.1988-203

[15] Anderson, D. N. (2004). Manual of scaling methods. NASA CR, 212875.

[16] Ruff, G. A. (1985). Analysis and verification of the icing scaling equations. volume 1. https://doi.org/10.21236/ada162226

[17] Han, Y., Palacios, J., & Schmitz, S. (2012). Scaled ice accretion experiments on a rotating wind turbine blade. Journal of Wind Engineering and Industrial Aerodynamics, 109, 55–67. https://doi.org/10.1016/j.jweia.2012.06.001

[18] Anderson, D. (1995). Methods for scaling icing test conditions. 33rd Aerospace Sciences Meeting and Exhibit. https://doi.org/10.2514/6.1995-540

[19] Anderson, D., & Ruff, G. (1999). Evaluation of methods to select scale velocity in icing scaling tests. 37th Aerospace Sciences Meeting and Exhibit. https://doi.org/10.2514/6.1999-244

[20] Anderson, D. N., & Ruff, G. (1997). Scaling methods for simulating aircraft in-flight icing encounters. In International Symposium on Scale Modeling (No. NAS 1.15: 107538).

[21] Potapczuk, M. G. (2013). Aircraft icing research at NASA glenn research center. Journal of Aerospace Engineering, 26(2), 260–276. https://doi.org/10.1061/(asce)as.1943-5525.0000322

[22] Anderson, D. (1994). Rime-, mixed- and glaze-ice evaluations of three scaling laws. 32nd Aerospace Sciences Meeting and Exhibit. https://doi.org/10.2514/6.1994-718

[23] Anderson, D., & Feo, A. (2002). Ice-accretion scaling using water-film thickness parameters. 40th AIAA Aerospace Sciences Meeting & Exhibit. https://doi.org/10.2514/6.2002-522

[24] Bilanin, A., & Anderson, D. (1995). Ice accretion with varying surface tension. 33rd Aerospace Sciences Meeting and Exhibit. https://doi.org/10.2514/6.1995-538

[25] Anderson, D. (2000). Effect of velocity in icing scaling tests. 38th Aerospace Sciences Meeting and Exhibit. https://doi.org/10.2514/6.2000-236

[26] Langmuir, I., & Blodgett, K. (1946). A mathematical investigation of water droplet trajectories (No. 5418). Army Air Forces Headquarters, Air Technical Service Command.

[27] Bragg, M. B. (1982). A similarity analysis of the droplet trajectory equation. AIAA Journal, 20(12), 1681–1686. https://doi.org/10.2514/3.8004

[28] Anderson, D., & Tsao, J.-C. (2003). Evaluation and validation of the messinger freezing fraction. 41st Aerospace Sciences Meeting and Exhibit. https://doi.org/10.2514/6.2003-1218

[29] Anderson, D. (1996). Further evaluation of traditional icing scaling methods. 34th Aerospace Sciences Meeting and Exhibit. https://doi.org/10.2514/6.1996-633

[30] Tsao, J.-C., & Anderson, D. (2005). Latest development in SLD scaling. 4th AIAA Theoretical Fluid Mechanics Meeting. https://doi.org/10.2514/6.2005-5187

[31] Anderson, D. (2001). Acceptable tolerances for matching icing similarity parameters in scaling applications. 39th Aerospace Sciences Meeting and Exhibit. https://doi.org/10.2514/6.2001-832

[32] Clift, R., Grace, J., & Weber, M. E. (2013). Bubbles, drops, and particles. Dover.

[33] Naterer, G. F. (2022) Advanced Heat Transfer, 3rd Edition, CRC Boca Raton, FL.

[34] ANSYS, (2015). FENSAP-ICE User Manual R1.0, Canada.

[35] Hu, L., Zhu, X., Hu, C., Chen, J., & Du, Z. (2017). Calculation of the water droplets local collection efficiency on the wind turbines blade. Journal of Energy Resources Technology, 139(5). https://doi.org/10.1115/1.4036329

[36] Fortin, G., & Perron, J. (2009). Wind turbine icing and de-icing. 47th AIAA Aerospace Sciences Meeting Including The New Horizons Forum and Aerospace Exposition. https://doi.org/10.2514/6.2009-274

[37] Kreith, F., & Manglik, R. M. (2018). Principles of Heat Transfer. Cengage Learning.

[38] Tribus, M., Young, G., & Boelter, L. (1948). Analysis of heat transfer over a small cylinder in icing conditions on Mount Washington. Trans. ASME, 70(8), 971-976

[39] Charpin, F., & Fasso, G. (1979). Icing testing in the large Modane wind-tunnel on full-scale and reduced scale models. In Conf. on Protection Against Icing (No. NASA-TM-75373)

[40] Olsen, W., & Walker, E. (1986). Experimental evidence for modifying the current physical model for ice accretion on aircraft surfaces (No. NASA-MPD-1683).

[41] Newton, J., & Olsen, W. (1986). Study of ice accretion on icing wind tunnel components. 24th Aerospace Sciences Meeting. https://doi.org/10.2514/6.1986-290

[42] Kind, R., Dillon, T., Gaydos, J., & Oleskiw, M. (1998). Evidence for importance of scaling viscous effects in the water film in Glaze icing tests. 36th AIAA Aerospace Sciences Meeting and Exhibit. https://doi.org/10.2514/6.1998-196

[43] Kind, R., & Oleskiw, M. (2001). Experimental assessment of a water-film-thickness Weber number for scaling of Glaze Icing. 39th Aerospace Sciences Meeting and Exhibit. https://doi.org/10.2514/6.2001-836

[44] Kind, R. (2001). Assessment of importance of water-film parameters for scaling of Glaze Icing. 39th Aerospace Sciences Meeting and Exhibit. https://doi.org/10.2514/6.2001-835

[45] Ruff, G., & Anderson, D. (1998). Quantification of ice accretions for icing scaling evaluations. 36th AIAA Aerospace Sciences Meeting and Exhibit. https://doi.org/10.2514/6.1998-195

[46] Lanzafame, R., & Messina, M. (2007). Fluid Dynamics Wind Turbine Design: Critical Analysis, Optimization and application of BEM theory. Renewable Energy, 32(14), 2291–2305. https://doi.org/10.1016/j.renene.2006.12.010

[47] Yirtici, O., Ozgen, S., Tuncer, I. H. (2019). Predictions of ice formations on wind turbine blades and power production losses due to icing. Wind Energy. https://doi.org/10.1002/we.2333

Chapter 6

6. Conclusions and Future Research

6.1. Conclusions

The following concluding remarks can be drawn from this thesis.

- The mass of ice is significantly influenced by the relative flow Reynolds number. This indicates that the large sections of the blade are characterized by a large characteristic length compared to the smaller blade sections, i.e. chord length, operating at the same flow conditions and rotational speed, which may result in more ice mass.
- Results in this thesis showed that heat transfer rates and freezing fraction values were slightly lower during the icing process over the smaller blade sections compared to the large blade sections.
- This results showed an increase in velocity over smaller blade sections. The distribution of pressure between similar blade sections is found to be relatively unchanged. More droplet collection is found on the smaller blade sections. Smaller blade sections have larger icing area coverage and ice mass.
- The results indicated higher droplet collection efficiencies at the leading edge, especially at the flow stagnation point, with an increase of the value towards the blade tip by 2.6 times. Subsequently, larger ice thicknesses were mainly found at the blade's leading edge, with higher accumulations in terms of overall thickness by 3.38 times and mass by 3.95 times towards the tip sections. The results suggested higher ice formations are expected near the blade tip, contributing to aerodynamic losses in terms of overall lift and drag coefficients.

- This research provided useful predictions for the changes in the flow field and ice accretion along a wind turbine blade span at different operating conditions.
- Numerical results showed that ice accretion is highest at the blade's leading edge and along the blade's span, especially in locations further from the blade root or closer to its tip.
- This research presented a scaling analysis of ice accretion on a rotating wind turbine blade.
- A formulation of the scaling parameters was developed for the flow field, droplet trajectory and ice accretion over a rotating blade including the mass and energy transfer processes during rime and glaze ice conditions.
- This research proposed new scaling methods to predict scaled ice characteristics on larger blade models, including thickness, shape, and mass.
- This research extended past scaling formulations for aircraft icing (i.e., flow over a fixed wing) to account for the rotation of a wind turbine blade.
- Newly derived variables were developed for scaling the air and droplet flows during rime and glaze ice conditions.
- The analysis considered the significant scaling dimensionless groups for ice conditions on a rotating blade, including the Reynolds number, two new speed ratio groups for the rotational forces, droplet inertia, drag on the droplet, ice accumulation parameter and relative heat factor.
- These derived dimensionless groups were used to obtain scaling relations that can scale flow conditions between similarly scaled geometries.
- Scaled variables in this research include the flow stream velocity, blade rotational speed, blade radius, droplet size, LWC, and icing time.
- The proposed scaling methods include the blade section size scaling and icing conditions.

- This research provides an incremental improvement to the current approach of CFD studies for ice formation on wind turbines, which is a challenging problem for both the industry and the CFD developers.

6.2. Recommendations for Future Research

There are many promising future research activities in the field of wind turbine icing. Despite the number of research activities and significant progress made in ice scaling in recent years, numerous avenues for further research remain for ice scaling on a rotating blade. Further analyzing the scaling parameters, developing new methods for ice accretion scaling and conducting numerical investigations are recommended. Future work would include experiments for verification of different scaling approaches. Future research may include testing the applicability of the new scaling parameters for icing investigation on vertical-axis wind turbines.

Future experimental programs may include the available laboratory facility at Memorial University of Newfoundland for icing tests on wind turbine blade models. Future experiments would consist of a closed loop flow space, a cooling chamber with a small open wind tunnel, a fan, a droplet spraying system and a scaled wind turbine model prototype. Further research work can also include identifying the particular limitations of the newly developed scaling parameters. Future research may be needed to continue the experimental setup made during this Ph.D. program for icing tests (See Appendix 1).

Appendix 1

Details on some components in the experimental setup are presented as follows.

Icing Facility Description

A walk-in cooling chamber within a space of 4.15 m in width, 4.15 m in height and 7.43 m in length is utilized for the icing tests. As shown in Fig. 6.1., an open wind tunnel is built in the cooling chamber to direct the super-cooled flow around the wind turbine prototype model and in a closed loop inside the cold room.

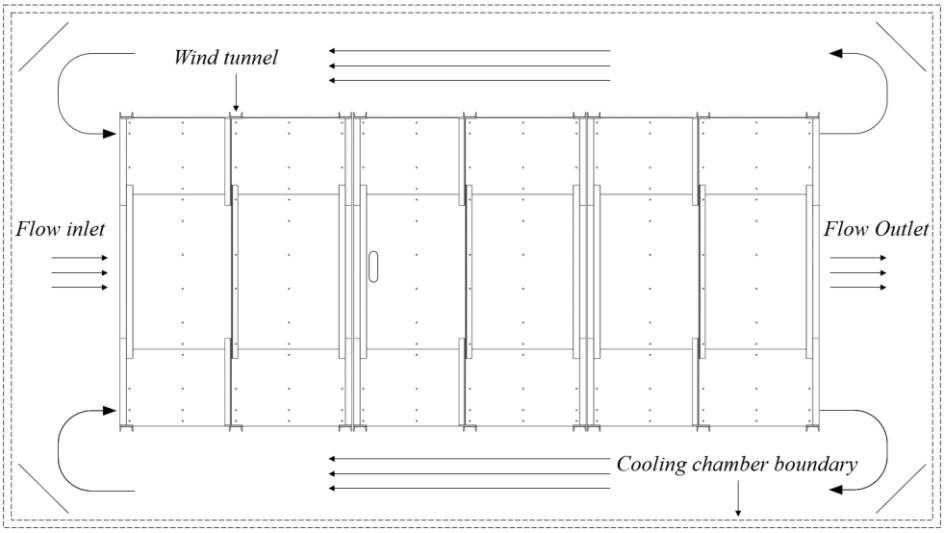

Figure 6.1. Overview of the icing facility with the wind tunnel and flow loop.

Wind Tunnel

A wind tunnel is designed to be assembled in three sizes to test various flow conditions during experiments. The wind tunnel has three similar connected sections; each consists of overlapped sheets that can be formed in three different sizes. As shown in Fig. 6.2a, the wind tunnel has three adjustable sections in the three available sizes. The first section contains an industrial fan for flow circulation and a flow straightener mesh panel after the fan to reduce flow turbulence and obtain steady flow during tests. The second section includes atomizing spray nozzles installed at the top

and a wind turbine prototype model placed at its end. The third section is empty, representing the wake region after the wind turbine prototype model. Fig. 6.2b shows an overview of the assembled wind tunnel (size 3) and the location of the other experiment components.

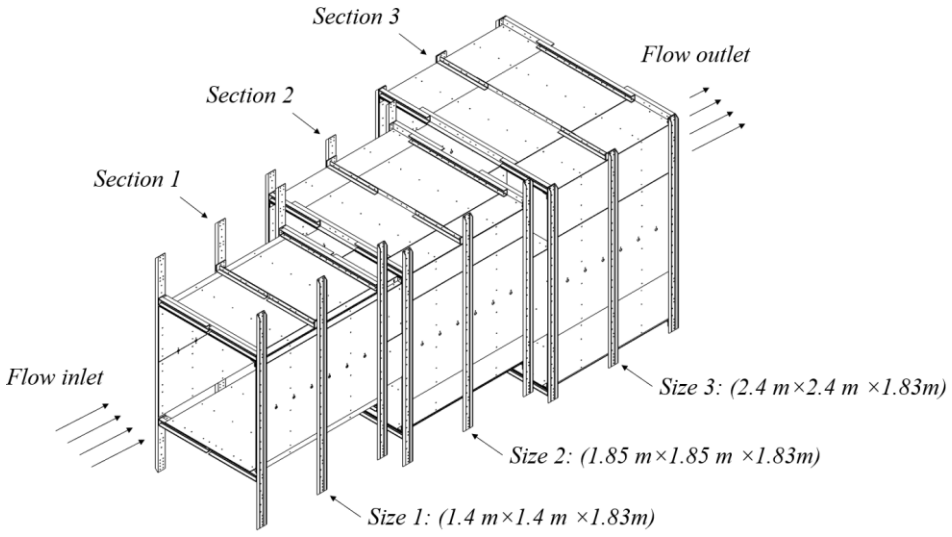

(a)

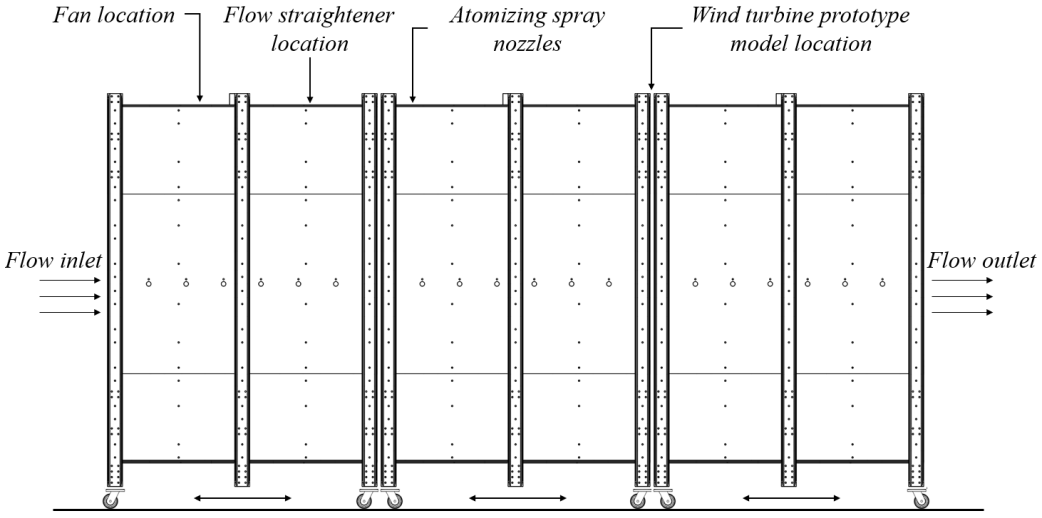

(b)

Figure 6.2. Layout of the wind tunnel: (a) three sections and the available sizes, and (b) locations of experimental components.

Each section comprises overlapped polycarbonate sheets and bolted connections consisting of aluminum C sections and angles for overall structure reinforcement. The wind tunnel sections and the wind turbine model are attached with casters for movability in the icing facility while conducting experiments. Small holes along each section are made for different measurements during tests. As shown in Fig. 6.3, a four-bladed fan with a controlling unit is placed inside the cooling chamber to circulate the air flow at different speeds. The closed flow loop in the cold chamber around the model is achieved through the wind tunnel boundaries.

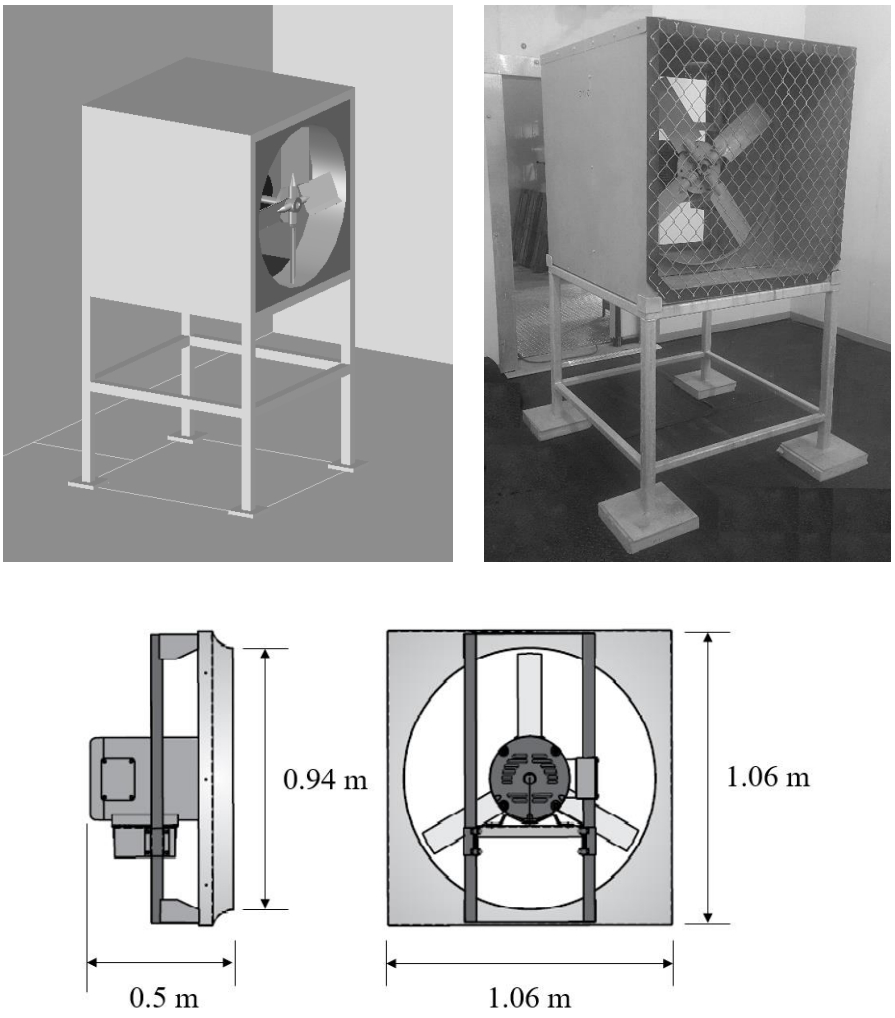

Figure 6.3. Dimensions of the fan and housing structure in the cold chamber.

Scaled Wind Turbine Prototype Model

As shown in Fig. 6.4, one-bladed wind turbines exist. A counterweight to balance the rotor must be placed on the hub's opposite side from the blade. Practical one-blade wind turbines with a counterweight were considered in designing the prototype models used for tests. A one-blade wind turbine model was created for icing investigation, similar to a large-scale one-blade wind turbine.

Figure 6.4. One-blade wind turbines.

Prototype scaled models are designed into two configuration cases. Case A contains scaled blade sections with counterweights, and Case B includes a full 1.1 m blade model with a counterweight. As shown in Figs. 6.5a and 6.5b, the schematic diagram for the model shows two setup configurations for icing tests. The wind turbine prototype model consists of a tower with a base, an electric motor with a variable-frequency drive (VFC), shaft couplings, a counterweight equivalent to the rotating blade model mass, steel threaded rods, a shaft with a vibration-damping mechanism and wind blade prototype models. The base includes a compartment that can be filled with sandbags to add to structural stability during operation. Threaded rods allow each small blade section to be fixed at any location in the spanwise direction and adjusted at different angles to enable precise placement of counterweights on the opposite side. The VFC controls the motor's

rotational speed by changing the input frequency. The rotational direction for experiments is a clockwise direction for blade models from the inlet flow perspective.

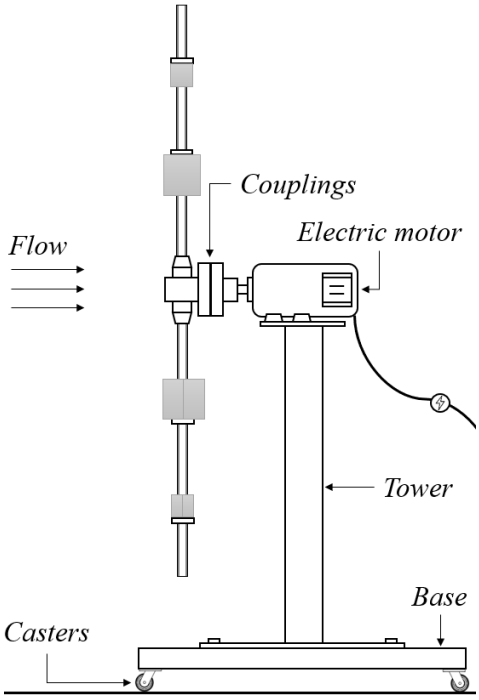

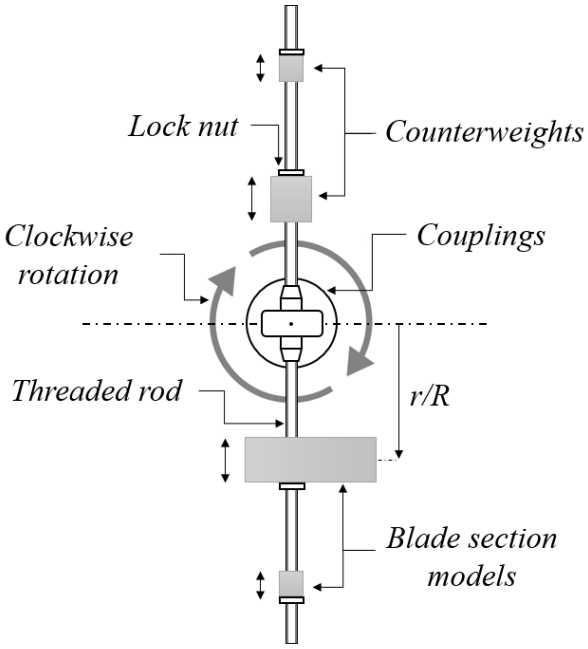

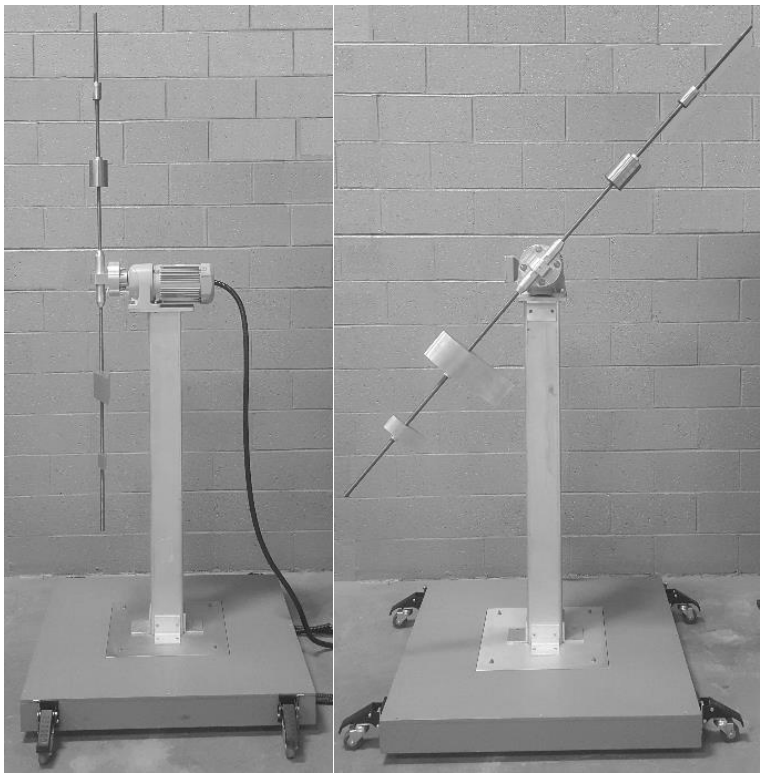

(a)

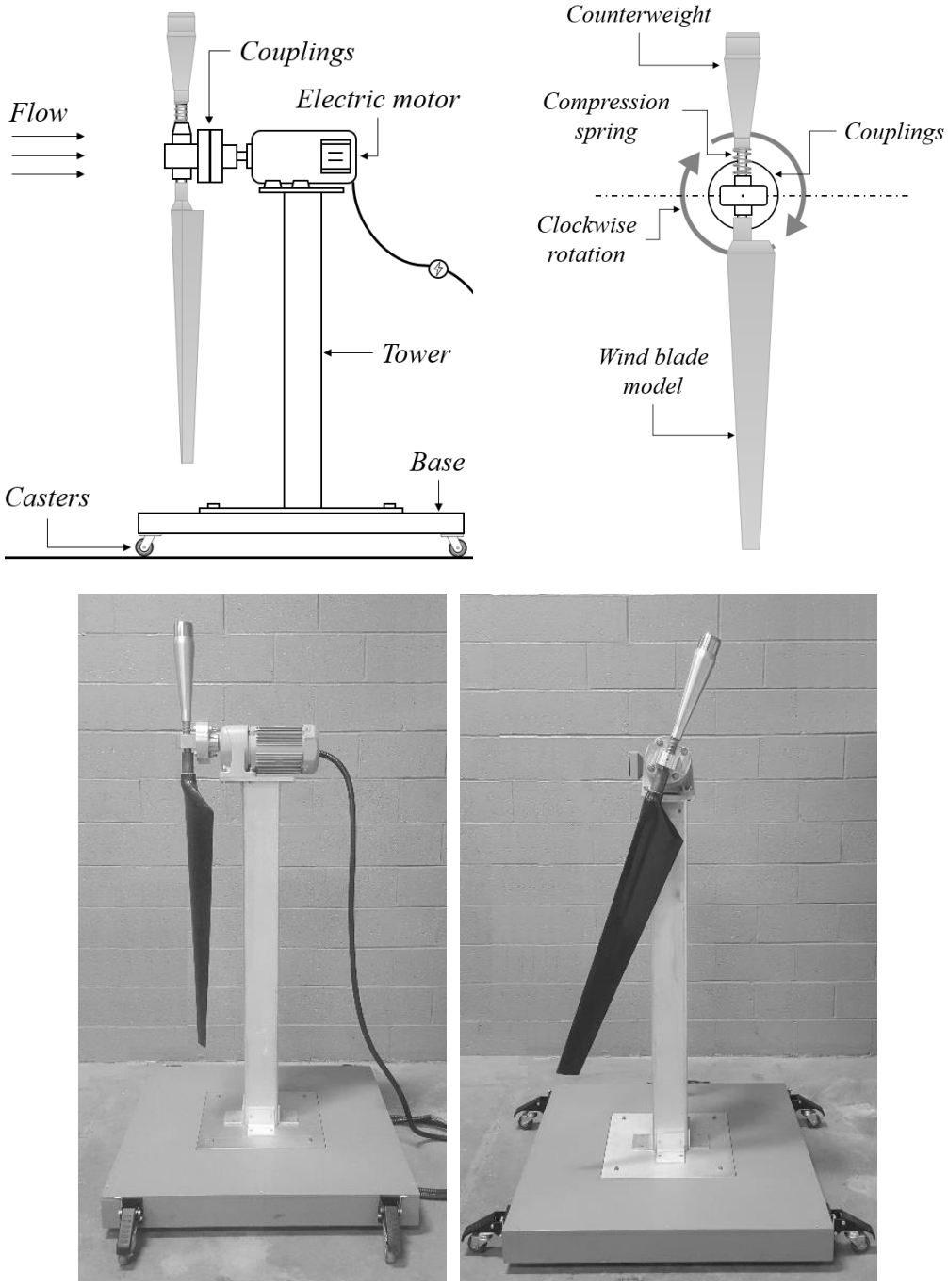

(b)

Figure 6.5. Discretization of the two cases: (a) Case A of one wind blade model testing and (b) Case B of blade section model testing.

As shown in Fig. 6.5a, two scaled blade sections with a non-symmetrical airfoil (NERL S809) are manufactured for ice accretion scaling tests. The prototype blade sections are related to each other by the scale factor. Each blade section is made from aluminum, and the counterweights are made from stainless steel. The smaller blade section represents a unity scale factor (i.e., k = 1) and is scaled up to 2 times. Values for each model dimension and each section area are shown in Table 6.1. As shown in Fig. 6.5b, a scaled entire wind blade model of a 1.1 m radius is fabricated to examine ice accretion along the blade span. The one-blade model is made from carbon fibre and attached to the hub via a steel shaft. The Blade Element Momentum (BEM) theory is applied in the entire blade model design process to obtain the chord length variation along the blade model span (i.e., at a TSR of 5). A non-symmetrical airfoil (NACA 63-415) is selected for the one-bladed model design.

Table 6.1. Scaled blade geometry characteristics

Parameter	**Scale factor, k**	
	1	2
Chord length (m)	0.15	0.3
Span wise length (m)	0.05	0.1
Section reference area (m^2) (i.e., Chord by span)	0.0075	0.03
Area impingement (m^2) (i.e., Perimeter by span)	0.0155	0.062